

Exploiting Clock Transitions for the chemical design of resilient molecular spin qubits

Silvia Giménez-Santamarina¹, Salvador Cardona-Serra¹, Juan M. Clemente-Juan^{1*}, Alejandro Gaita-Ariño^{1*}, Eugenio Coronado^{1*}

¹ICMol. Universitat de València. C/ Catedrático José Beltrán nº 2, 46980 Paterna, Valencia, España.

Supplementary information

S1.	Description of the algorithm and code flow	2
a.	From discrete to continuous Zeeman diagrams	2
b.	Characterization of the Clock Transitions	6
S2.	Vanadyl dithiolates complexes	9
a.	Analytical solutions	11
S3.	HoW10	15
a.	Studies with the Radial Effective Charge (REC) model	16
S4.	Cubic symmetry: expanding the anticrossing taxonomy	17
a.	Potential CTs in a perfect cubic HoPd12	84
b.	Potential CTs for X-band EPR along 1% compression of HoPd12	87
S5.	Estimate of instantaneous vibrational distortions	88
S6.	Probability of CTs for VO derivative	89

S1. Description of the algorithm and code flow

a. From discrete to continuous Zeeman diagrams

The coexistence of crossings and avoided crossings possesses an intrinsic difficulty for numerical methods, in our case this is translated into how to correctly label and order the magnetic levels (see Fig. 2, main text). When analyzing the relative energies of a distribution of spin states varying with an external magnetic field, we need to keep track (and consistently label) the different energy levels. This is not trivial when the energy level set is calculated numerically and independently at each different magnetic field. A naïve ordering from lowest to highest magnetic field is physically meaningless, and this technical problem can arise from the numerical methods used to obtain these values from standard diagonalization routines.

We have chosen to overcome this problem with a particular methodology: We start from a given input data set and evaluate the continuum evolution of each spin level with an increasing magnetic field. It is achieved by (1) fitting and (2) extrapolating the numerical function that defines the behavior of a variable or category as a function of another and find the equivalent value in the first data set (See Fig. S1).

(1) The program fits a second order polynomial expression for the first set of five consecutive points (x variable, energy) of each variable (data group, spin level). The user should ensure that the first five points in the given input data set pertain to the same function in order to achieve the reliable estimation of the following value.

(2) By extrapolation, it calculates the following point and maps the input set of values performing a numerical evaluation to scrutinize the analogous item. Then the column number of the match is mapped and written in an intermediate file. Then, this file is used as a ‘mask’ to finally re-order the input data set by creating a new matrix. There the continuity of the dependence of each group as a function of another variable are traced by the values in each column. Whenever the estimates and the data differ, the program generates a matrix with the input energies but reordered to guarantee the continuity of the energy levels (see Figure S2, S3, S4 center).

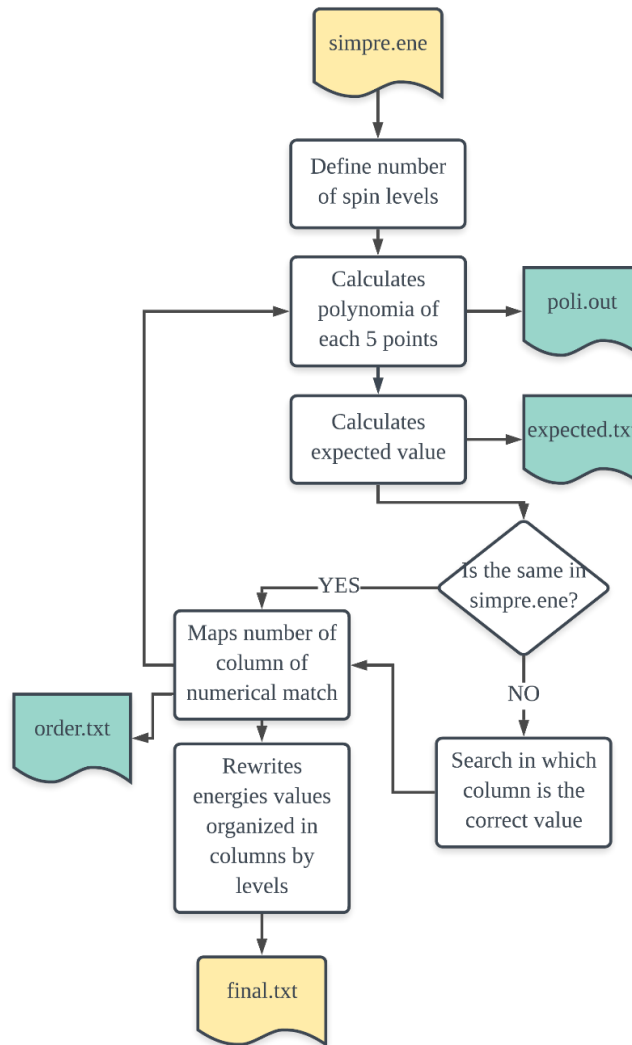


Figure S1: Workflow of the initial script designed with the functionality of mapping and reordering the energy values that traces the magnetic behavior of each spin level in the presence of a magnetic field.

Finally, as a quality control check after the run of the script, a multiplot figure is created with the objective of providing a fast and easy graphical control of the results. At the upper panel of the multiplot the user will find the graphical representation of the raw input/initial data set; next to it, the polynomial estimated values after the fitting and extrapolation stages, and finally, the values from the input data set re-ordered as a continuous function. The coloring in the plots remarks very evidently which traces are correct and which are incorrect within all categories. In addition, we provide two extra plots at the bottom of the panel to numerically evaluate the order of magnitude of the mapping (difference between initial value and estimated value) and the range of error of this evaluation. (See Figs. S2, S3 and S4 as methodological examples)

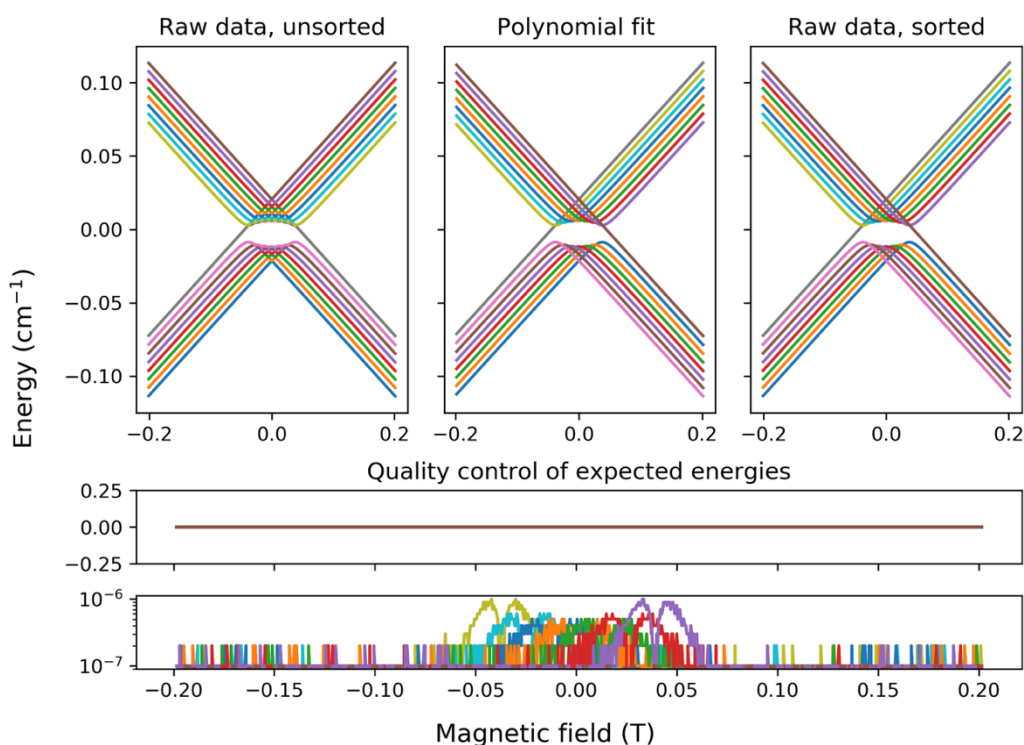


Figure S2: Results of the mapping processes and quality control plots after running the first script of our code for the first calculation concerning the Vanadyl-like case study. See main text section “**Vanadyl dithiolates complexes**”.

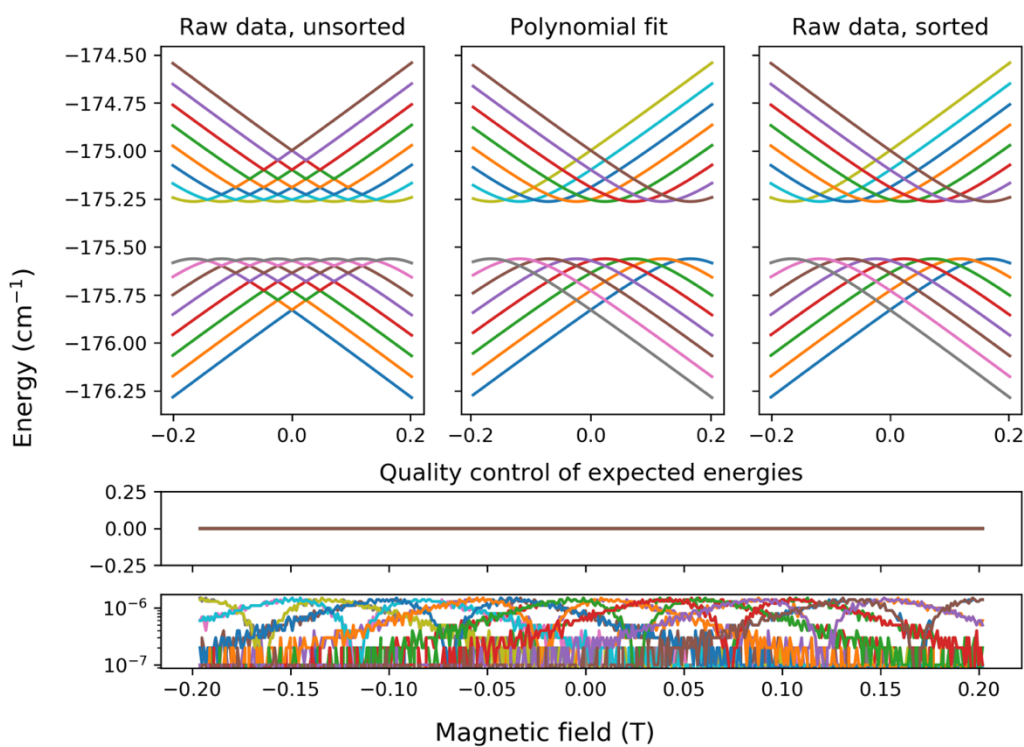


Figure S3: Results of the mapping processes and quality control plot of the fundamental octuplets after running the first script of our code for the first calculation concerning the case of HoW₁₀. See main text section “**Antiprismatic holmium POM complex**”.

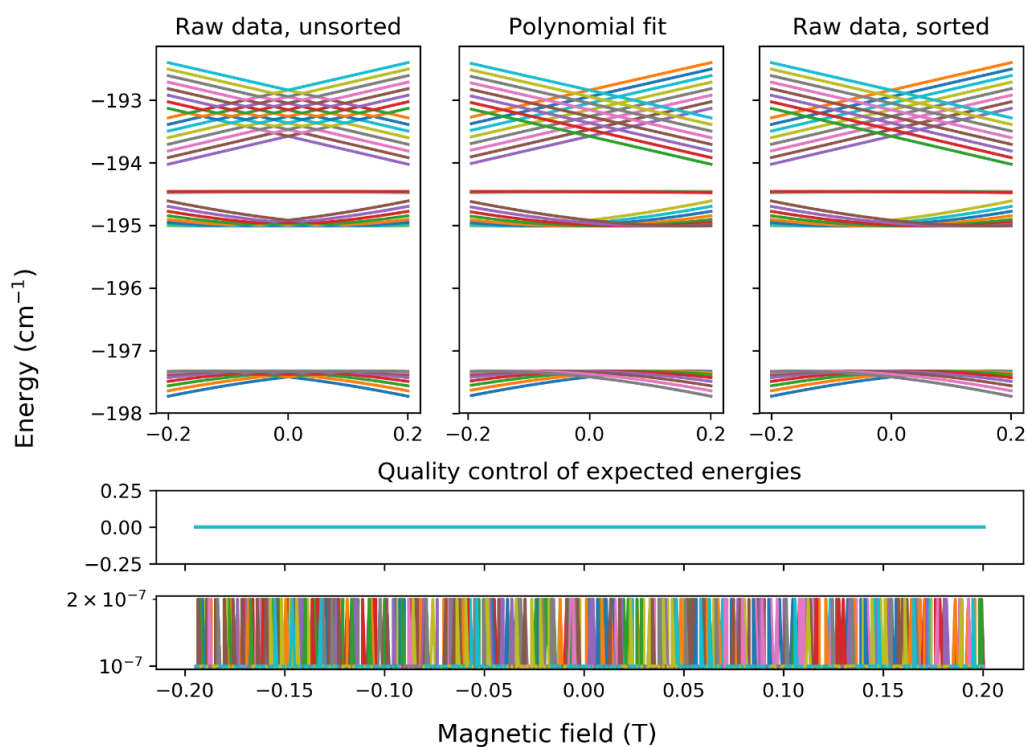


Figure S4: Results of the mapping processes and quality control plot after running the first script of our code for the first calculation concerning the cubic polyoxopaladate case. See main text section “**Cubic holmium POM complex**”.

b. Characterization of the Clock Transitions

Starting from general data containing numerical values (y coordinate) as a function of an independent variable (x coordinate), the algorithm compares the evolution of each y curve and finds the regions where the numerical difference of values are inside a certain range (a threshold externally defined by the user), and identifies whether in these regions the first derivative is equal or close to zero. A second threshold, defined by default but modifiable by the user, deals with the difference between slopes of two specific levels. In principle, this later threshold will define quality and width of the search of transitions.

Following the code workflow (Figure S5), first, the user externally defines the threshold to search for Clock Transitions. This is the energy difference (in units of cm^{-1}) in which the user is interested. This specific range can come from technical limitations such for instance, availability of specific EPR-bands to study a given compound. Once the energies are ordered in columns and the magnetic field dependence (independent variable) is considered, the script calculates the numerical energy difference for each possible combination of levels. If such difference is lower or equal to the energy threshold, the first derivative (curve slope) for each level at the given magnetic field value is calculated and compared. If the difference between the calculated slopes is less or equal to the threshold, we have encountered a potential Clock transition. To identify the character of the potential transition, meaning, to evaluate if the evolution of the spin levels will rise to a crossing or to an anticrossing, other variables are calculated as needed such as absolute value of the gap energy, difference of absolute energy values and the ratio of first derivatives.

Once we have identify which levels and in which regions of the function we could find a target for obtaining a possible CTs, we classify them as crossing or anticrossings by evaluating the sign of the curve slopes: A crossing will never change its sign while an anticrossing will vary it approaching to zero and then continue with the opposite sign. An anticrossing can be locally approximated by a mathematical quadratic function, so it is easy to calculate the vertex of the parabola from this polynomial expression. In this point, the script ensures the good extrapolation and polynomial fitting of the function every 5 points.

In this point of the workflow, the second derivative is calculated. The script then evaluates whether this second derivative is equal or very close to zero, and the vertex of the parabola, in order to get the minimum and the maximum of the function.

The curvature is quantified as follows: given the quadratic expression ($y = ax^2 + bx + c$) defining the CTs, one can calculate the curvature at the vertex of the parabola with the following formula:

$$k = \frac{y''}{(1 + y'^2)^{3/2}}$$

Then, substituting first and second derivatives we obtain:

$$k = \frac{2a}{(1 + (2ax_v + b)^2)^{3/2}}$$

where x_v is the maximum or minimum value at the vertex of the quadratic function.

The output produced by the script contains the labelling of the levels mixing, the value of the magnetic field at which they appear (x coordinate), the maximum or minimum energy value of each of curves involved in the transition, the energy gap difference and finally the curvature of both transitions.

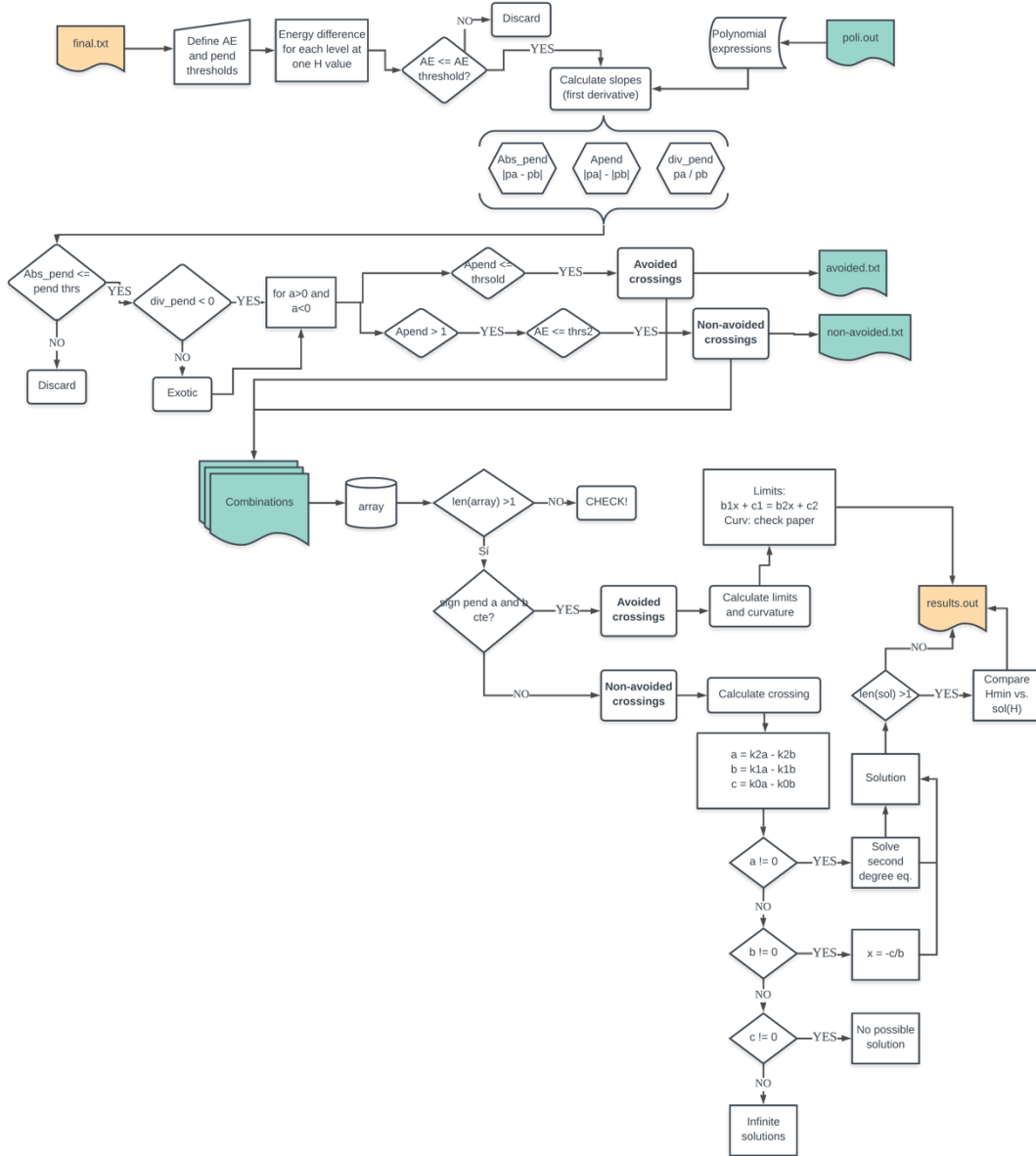


Figure S5: General workflow of the second script that classifies the avoided and non-avoided crossings. Two different thresholds are applied (transition frequency and slopes difference), to ensure the direct and reliable search of Clock transitions in a frequency window. Certain number of intermediate files are created for data storage and quality control.

An example of the information produced by the program is given at table S1. The columns i and j refer to the levels involved in the transition, after re-ordering as explained in section S1a, with energies “ E_{cross1} ”, “ E_{cross2} ”, respectively. The “*Type*” column serves to identified the crossings as avoided (“anticrossings” in the main text). “ H_{cross} ” is the magnetic field at which the anticrossing is appearing, labeled as B_{CT} in the main text. “ AE_{ij} ” is the tunneling splitting labelled in the main text as Δ , or, generally, the energy difference at the anticrossing. “*Curvature 1*” and “*Curvature 2*” correspond to the second derivatives of the polynomial functions that fit the curves of levels i and j in the vicinity of the anticrossing; these are labelled as k_i , k_j in the main text.

Table S1: Output information obtained after running the program. The example corresponds to the first calculation of Vanadyl-like complex study. See main text section “**Vanadyl dithiolates complexes**” for more detailed information on the chemical system. The results are written in plain text in a matrix format. i, j are referred to the levels involved (sorted from lowest to highest energy at magnetic field negative limit); type of crossing; H_{CT} is the value of magnetic field where the CT appears (T); E_i and E_j is the energy at the maximum or minimum of the spin level where the transition is found (cm^{-1}); ΔE_{ij} corresponds to tunneling splitting of the transition (cm^{-1}) and k_i, k_j mean the value of the curvature.

i	j	Type	H_{CT}	E_i	E_j	ΔE_{ij}	k_i	k_j
1	15	Avoided	0.03797	-0.0087192	0.0028692	0.0115884	36.74286	36.74286
2	14	Avoided	0.02531	-0.0105114	0.0046614	0.0151727	28.05714	28.05714
3	13	Avoided	0.01266	-0.0114068	0.0055568	0.0169637	25.25714	25.25714
4	12	Avoided	0.00000	-0.0116850	0.0058350	0.0175200	24.28571	24.28571
5	11	Avoided	-0.01266	-0.0114068	0.0055568	0.0169637	25.20000	25.20000
6	10	Avoided	-0.02531	-0.0105113	0.0046613	0.0151727	28.17143	28.17143
7	9	avoided	-0.03797	-0.0087192	0.0028692	0.0115883	36.91429	36.91429

S2. Vanadyl dithiolates complexes

We evaluated the robustness of the CTs appearing in vanadium-based dithiolate complexes, such as $[\text{VO}(\text{C}_x\text{S}_y)_2]^{2-}$ and $[\text{V}(\text{C}_x\text{S}_x)_3]^{2-}$. We have selected such families because of their interesting performance acting as molecular spin qubits (i.e. high coherence time T_2)

In this section we will focus on the different behavior of anticrossings in the typical range of A_{\parallel}/A_{\perp} ratios for vanadyl and vanadium complexes. Starting from the hyperfine parameters given for the four V(IV)-based complexes in [1,2], we calculated the average value corresponding to the hyperfine coupling components where: $\overline{A_{\parallel}} = 414.5 \text{ MHz} = 0.013825 \text{ cm}^{-1}$; $\overline{A_{\perp}} = 131.25 \text{ MHz} = 0.004385 \text{ cm}^{-1}$ for vanadyl complexes [1] and $\overline{A_{\parallel}} = -307 \text{ GHz} = 0.010234 \text{ cm}^{-1}$; $\overline{A_{\perp}} = 51 \text{ GHz} = 0.001736 \text{ cm}^{-1}$ for vanadium complexes [2]. We chose vanadyl family of complexes as a reason as the lower dispersion in the hyperfine parameters, but this study could be extended to vanadium family as well.

Table S2: Vanadyl and vanadium hyperfine coupling values (A_{\parallel} , parallel; A_{\perp} , perpendicular).

VO Complex	A_{\parallel}	A_{\perp}
1	411 MHz = 0.01371 cm^{-1}	131 MHz = 0.00437 cm^{-1}
2	414 MHz = 0.01381 cm^{-1}	131 MHz = 0.00437 cm^{-1}
3	418 MHz = 0.01384 cm^{-1}	132 MHz = 0.00440 cm^{-1}
4	415 MHz = 0.01394 cm^{-1}	131 MHz = 0.00437 cm^{-1}
V Complex		
1	-265 MHz = -0.00884 cm^{-1}	46 MHz = 0.00153 cm^{-1}
2	-270 MHz = -0.00901 cm^{-1}	45 MHz = 0.00155 cm^{-1}
3	-340 MHz = -0.01134 cm^{-1}	65 MHz = 0.00217 cm^{-1}
4	-329 MHz = -0.01097 cm^{-1}	46 MHz = 0.00153 cm^{-1}
5	-330 MHz = -0.01101 cm^{-1}	57 MHz = 0.00190 cm^{-1}

We varied both A_{\parallel} and A_{\perp} parameters by $\pm 15\%$ sequentially, this means vary one of them while keeping the other in its typical value in order to have a good analysis of the influence of each parameter. The study consists on a numerical processing of 658 calculated curves, of which we represent a selection in Fig. 4, coincides with the analytical solution that is possible in this case (see SI section S4) in the linear dependence, for all CTs, of the transition frequency and its curvature as a function of A_{\perp} and of the magnetic field where the CT appears as a function of A_{\parallel} . The tunneling gap of each CT appearing at the following magnetic fields ($B_1 = 0.00$, $B_2 = \pm 0.01493$, $B_3 = \pm 0.02986$, $B_4 = \pm 0.04478$ T) take values of: $\Delta_1 = [0.05800]$, $\Delta_2 = [0.05616]$, $\Delta_3 = [0.05023]$, $\Delta_4 = [0.00986-0.03836]$ (cm^{-1}). And the curvature of each CT is quantified: $k_1 = 30.34$, $k_2 = 31.37$, $k_3 = 35.09$, $k_4 = 46.10$ (cm^{-1}/T)².

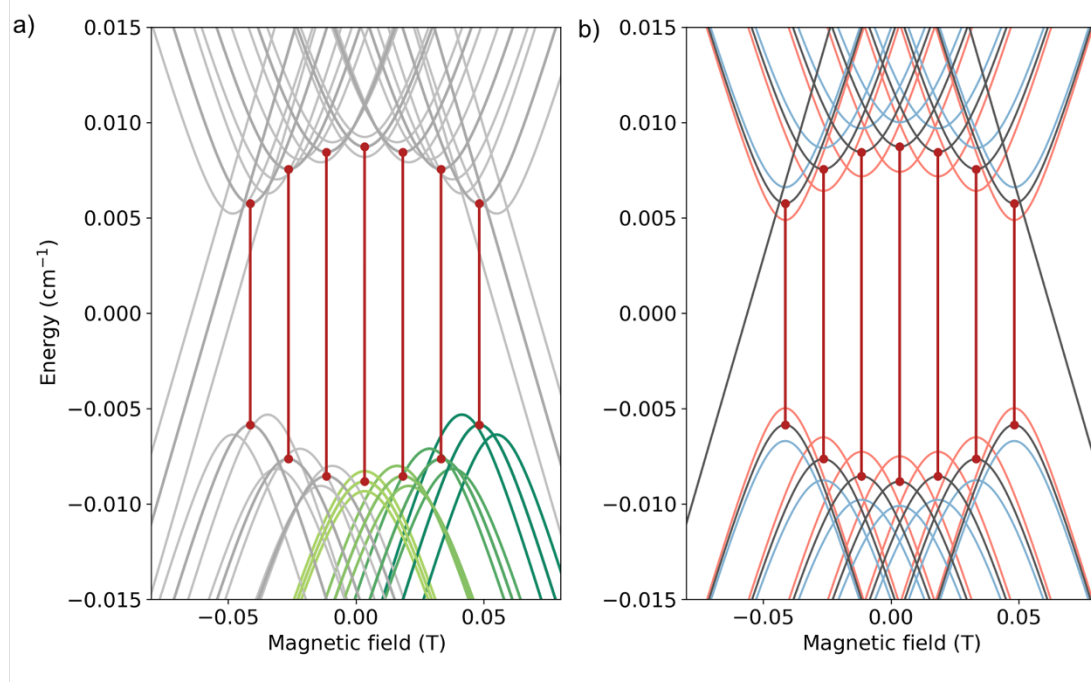


Figure S6: a) Full Zeeman diagram showing the effects of a $\pm 15\%$ variation in $A_{||}$. b) Full Zeeman diagram showing the effects of a $\pm 15\%$ variation in A_{\perp} .

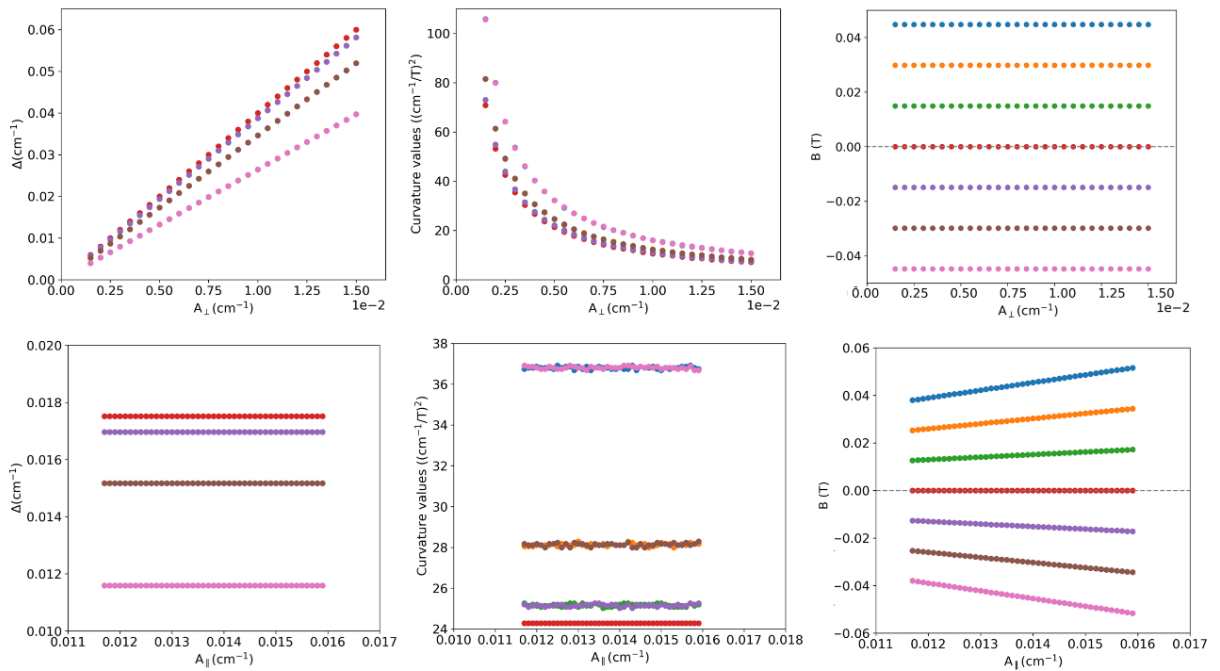


Figure S7: Dependencies of a) tunneling splitting, Δ ; b) curvature, k ; and c) magnetic field B_{CT} in a $\pm 15\%$ variation in A_{\perp} .

a. Analytical solutions

We extracted analytical solution for the dependence of energy spin levels as a function of A_{\parallel} , A_{\perp} . The case of vanadyl complexes is especially interesting due to the possibility of obtaining analytical expression where is possible to obtain the energy of a given spin level as a function of A_{\parallel} , A_{\perp} parameters.

Starting from a molecular complex with $S = 1/2$ and $I = 7/2$; Heisenberg and hyperfine Hamiltonian can be applied to obtain the eigenvalues and eigenvectors corresponding to the wave function and energy of each spin energy level.

$$\hat{H} = A_{\parallel}I_zS_z + A_{\perp}(I_xS_x + I_yS_y) + g_S\mu_B S_z B$$

Where H is the magnetic field, μ_B is the Bohr magneton, g is electronic g-tensor, A is the hyperfine vector (components decomposed in A_{\parallel} and A_{\perp}), S is the electronic spin projection and I the nuclear spin projection.

Then, a matrix can be created where the basis functions are all the possible combination of electronic and nuclear spin projections (M_S , M_I). Once the H is applied, the obtained matrix will present all the extradiagonal terms equal to zero and the diagonal will contain the expressions relative to each combination.

$$\langle M_S M_I | \hat{H} | M_S M_I \rangle = \mu_B \cdot g \cdot M_S \cdot H \cdot \delta M_I M_I,$$

Through the analytical diagonalization of the energy matrix we can obtain the expression of the 16 energy levels:

$$E_1 = \frac{1}{4}(7A_{\parallel} - 2g\mu_B B)$$

$$E_2 = \frac{1}{4}(7A_{\parallel} + 2g\mu_B B)$$

$$E_3 = \frac{1}{4}\left(-A_{\parallel} - 2\sqrt{(4A_{\perp})^2 + (g\mu_B B)^2}\right)$$

$$E_4 = \frac{1}{4}\left(-A_{\parallel} + 2\sqrt{(4A_{\perp})^2 + (g\mu_B B)^2}\right)$$

$$E_5 = \frac{1}{4}\left(-A_{\parallel} - 2\sqrt{(\sqrt{7}A_{\perp})^2 + (3A_{\parallel})^2 - 6A_z g\mu_B B + (g\mu_B B)^2}\right)$$

$$E_6 = \frac{1}{4}\left(-A_{\parallel} + 2\sqrt{(\sqrt{7}A_{\perp})^2 + (3A_{\parallel})^2 - 6A_z g\mu_B B + (g\mu_B B)^2}\right)$$

$$E_7 = \frac{1}{4}\left(-A_{\parallel} - 2\sqrt{(2\sqrt{3}A_{\perp})^2 + (2A_{\parallel})^2 - 4A_z g\mu_B B + (g\mu_B B)^2}\right)$$

$$E_8 = \frac{1}{4}\left(-A_{\parallel} + 2\sqrt{(2\sqrt{3}A_{\perp})^2 + (2A_{\parallel})^2 - 4A_z g\mu_B B + (g\mu_B B)^2}\right)$$

$$E_9 = \frac{1}{4}\left(-A_{\parallel} - 2\sqrt{(\sqrt{15}A_{\perp})^2 + A_{\parallel}^2 - 2A_z g\mu_B B + (g\mu_B B)^2}\right)$$

$$E_{10} = \frac{1}{4}\left(-A_{\parallel} + 2\sqrt{(\sqrt{15}A_{\perp})^2 + A_{\parallel}^2 - 2A_z g\mu_B B + (g\mu_B B)^2}\right)$$

$$\begin{aligned}
E_{11} &= \frac{1}{4} \left(-A_{\parallel} - 2\sqrt{(\sqrt{15}A_{\perp})^2 + A_{\parallel}^2} + 2A_z g\mu_B B + (g\mu_B B)^2 \right) \\
E_{12} &= \frac{1}{4} \left(-A_{\parallel} + 2\sqrt{(\sqrt{15}A_{\perp})^2 + A_{\parallel}^2} + 2A_z g\mu_B B + (g\mu_B B)^2 \right) \\
E_{13} &= \frac{1}{4} \left(-A_{\parallel} - 2\sqrt{(2\sqrt{3}A_{\perp})^2 + (2A_{\parallel})^2} + 4A_z g\mu_B B + (g\mu_B B)^2 \right) \\
E_{14} &= \frac{1}{4} \left(-A_{\parallel} + 2\sqrt{(2\sqrt{3}A_{\perp})^2 + (2A_{\parallel})^2} + 4A_z g\mu_B B + (g\mu_B B)^2 \right) \\
E_{15} &= \frac{1}{4} \left(-A_{\parallel} - 2\sqrt{(\sqrt{7}A_{\perp})^2 + (3A_{\parallel})^2} + 6A_z g\mu_B B + (g\mu_B B)^2 \right) \\
E_{16} &= \frac{1}{4} \left(-A_{\parallel} + 2\sqrt{(\sqrt{7}A_{\perp})^2 + (3A_{\parallel})^2} + 6A_z g\mu_B B + (g\mu_B B)^2 \right)
\end{aligned}$$

To calculate the position of the clock-transitions we derive the energies against the applied magnetic field:

$$\begin{aligned}
\frac{\partial E_1}{\partial B} &= -\frac{g_S \mu_B}{2} \\
\frac{\partial E_2}{\partial B} &= \frac{g_S \mu_B}{2} \\
\frac{\partial E_3}{\partial B} &= -\frac{(g\mu_B)^2 B}{2\sqrt{(4A_{\perp})^2 + (g\mu_B B)^2}} \\
\frac{\partial E_4}{\partial B} &= \frac{(g\mu_B)^2 B}{2\sqrt{(4A_{\perp})^2 + (g\mu_B B)^2}} \\
\frac{\partial E_5}{\partial B} &= -\frac{-3A_{\parallel} g\mu_B + (g\mu_B)^2 B}{2\sqrt{(\sqrt{7}A_{\perp})^2 + (3A_{\parallel})^2} - 6A_{\parallel} g\mu_B B + (g\mu_B B)^2} \\
\frac{\partial E_6}{\partial B} &= \frac{-3A_{\parallel} g\mu_B + (g\mu_B)^2 B}{2\sqrt{(\sqrt{7}A_{\perp})^2 + (3A_{\parallel})^2} - 6A_{\parallel} g\mu_B B + (g\mu_B B)^2} \\
\frac{\partial E_7}{\partial B} &= -\frac{-2A_{\parallel} g\mu_B + (g\mu_B)^2 B}{2\sqrt{(2\sqrt{3}A_{\perp})^2 + (2A_{\parallel})^2} - 4A_{\parallel} g\mu_B B + (g\mu_B B)^2} \\
\frac{\partial E_8}{\partial B} &= \frac{-2A_{\parallel} g\mu_B + (g\mu_B)^2 B}{2\sqrt{(2\sqrt{3}A_{\perp})^2 + (2A_{\parallel})^2} - 4A_{\parallel} g\mu_B B + (g\mu_B B)^2}
\end{aligned}$$

$$\begin{aligned}
\frac{\partial E_9}{\partial B} &= -\frac{-A_{\parallel}g\mu_B + (g\mu_B)^2 B}{2\sqrt{(\sqrt{15}A_{\perp})^2 + A_{\parallel}^2 - 2A_{\parallel}g\mu_B B + (g\mu_B B)^2}} \\
\frac{\partial E_{10}}{\partial B} &= \frac{-A_{\parallel}g\mu_B + (g\mu_B)^2 B}{2\sqrt{(\sqrt{15}A_{\perp})^2 + A_{\parallel}^2 - 2A_{\parallel}g\mu_B B + (g\mu_B B)^2}} \\
\frac{\partial E_{11}}{\partial B} &= \frac{A_{\parallel}g\mu_B + (g\mu_B)^2 B}{2\sqrt{(\sqrt{15}A_{\perp})^2 + A_{\parallel}^2 + 2A_{\parallel}g\mu_B B + (g\mu_B B)^2}} \\
\frac{\partial E_{12}}{\partial B} &= \frac{A_{\parallel}g\mu_B + (g\mu_B)^2 B}{2\sqrt{(\sqrt{15}A_{\perp})^2 + A_{\parallel}^2 + 2A_{\parallel}g\mu_B B + (g\mu_B B)^2}} \\
\frac{\partial E_{13}}{\partial B} &= -\frac{2A_{\parallel}g\mu_B + (g\mu_B)^2 B}{2\sqrt{(2\sqrt{3}A_{\perp})^2 + (2A_{\parallel})^2 + 4A_{\parallel}g\mu_B B + (g\mu_B B)^2}} \\
\frac{\partial E_{14}}{\partial B} &= \frac{2A_{\parallel}g\mu_B + (g\mu_B)^2 B}{2\sqrt{(2\sqrt{3}A_{\perp})^2 + (2A_{\parallel})^2 + 4A_{\parallel}g\mu_B B + (g\mu_B B)^2}} \\
\frac{\partial E_{15}}{\partial B} &= -\frac{3A_{\parallel}g\mu_B + (g\mu_B)^2 B}{2\sqrt{(\sqrt{7}A_{\perp})^2 + (3A_{\parallel})^2 + 6A_{\parallel}g\mu_B B + (g\mu_B B)^2}} \\
\frac{\partial E_{16}}{\partial B} &= \frac{3A_{\parallel}g\mu_B + (g\mu_B)^2 B}{2\sqrt{(\sqrt{7}A_{\perp})^2 + (3A_{\parallel})^2 + 6A_{\parallel}g\mu_B B + (g\mu_B B)^2}}
\end{aligned}$$

By zeroing these derivatives, we can obtain the positions of the transitions and the energy gap between the lower and higher levels at a certain field. Levels 1 and 2 are just straight lines. The remaining 14 levels always present a maximum or minimum at a discrete magnetic field value.

In the following table we represent these 14 levels in 7 pairs. These pairs represent the two energy levels that have a minimum and a maximum respectively at a specific magnetic field. In addition, we give the energy difference between both curves and the curvature in the minimum gap field.

levels 3–4	$B = 0$	$\Delta E_{4-3} = 4A_{\perp}$	$curvature = \frac{\beta^2 g^2}{8A_{\perp}} = \frac{\beta^2 g^2}{2\Delta}$
levels 5–6	$B = \frac{3A_{\parallel}}{g\mu_B}$	$\Delta E_{6-5} = \sqrt{7}A_{\perp}$	$curvature = \frac{\mu_B^2 g^2}{2\sqrt{7}A_{\perp}} = \frac{\mu_B^2 g^2}{2\Delta}$
levels 7–8	$B = \frac{2A_{\parallel}}{g\mu_B}$	$\Delta E_{8-7} = 2\sqrt{3}A_{\perp}$	$curvature = \frac{\mu_B^2 g^2}{4\sqrt{3}A_{\perp}} = \frac{\mu_B^2 g^2}{2\Delta}$
levels 9–10	$B = \frac{A_{\parallel}}{g\mu_B}$	$\Delta E_{10-9} = \sqrt{15}A_{\perp}$	$curvature = \frac{\mu_B^2 g^2}{2\sqrt{15}A_{\perp}} = \frac{\mu_B^2 g^2}{2\Delta}$
levels 11–12	$B = -\frac{A_{\parallel}}{g\mu_B}$	$\Delta E_{12-11} = \sqrt{15}A_{\perp}$	$curvature = \frac{\mu_B^2 g^2}{2\sqrt{15}A_{\perp}} = \frac{\mu_B^2 g^2}{2\Delta}$
levels 13–14	$B = -\frac{2A_{\parallel}}{g\mu_B}$	$\Delta E_{14-13} = 2\sqrt{3}A_{\perp}$	$curvature = \frac{\mu_B^2 g^2}{4\sqrt{3}A_{\perp}} = \frac{\mu_B^2 g^2}{2\Delta}$
levels 15–16	$B = -\frac{3A_{\parallel}}{g\mu_B}$	$\Delta E_{16-15} = \sqrt{7}A_{\perp}$	$curvature = \frac{\mu_B^2 g^2}{2\sqrt{7}A_{\perp}} = \frac{\mu_B^2 g^2}{2\Delta}$

S3. HoW10

For the simplest test-case study, $[\text{Ho}(\text{W}_5\text{O}_{18})_2]^{9-}$ (hereafter HoW10 for simplicity), from the previously reported crystal field parameters (see Table S2) we varied B_4^4 parameter in a range of $\Delta B_4^4 \hat{O}_4^4 = B_4^4 \hat{O}_4^4 \pm 2\sigma$, where $\sigma_{B_4^4} = 2.1 \times 10^{-5} \text{ cm}^{-1}$ responsible for the inhomogeneous broadening. [3]

Table S2: Empirical values of CFP in Stevens notation of HoW10.

B_2^0	0.60141602cm ⁻¹	18.03GHz
B_4^0	0.00697149cm ⁻¹	209MHz
B_4^4	0.00314551cm ⁻¹	0.09GHz
B_6^0	0.00005104cm ⁻¹	-1.53 MHz

\hat{O}_4^4 consists in fourth order ladder operators which mix levels presenting m_j that differ in 4, or multiples of 4. In the Stevens Extended Operator notations $\hat{O}_k^q(J)$ it is defined as:

$$O_4^4 \equiv O_4^4(c) = \frac{1}{2}[J_+^4 + J_-^4]$$

However, in this small parameter range we did find a locally linear dependence both of the energy gap and of the curvature of all eight anticrossings as a function of the crystal field parameter B_4^4 (see SI section S3) which evolve approximately according to the equations $\Delta = 194.42 \cdot B_4^4 - 0.31 \text{ cm}^{-1}$, $k = -22446.81 \cdot B_4^4 + 106.18 \text{ cm}^{-1}/\text{T}^2$. In practice, molecules that in the timescale of the pulsed EPR experiment present an extradiagonal parameter that deviates $\sigma_{B_4^4} = 2.1 \cdot 10^{-5} \text{ cm}^{-1}$ from the average value of $B_4^4 \hat{O}_4^4 = 3.14 \cdot 10^{-3} \text{ cm}^{-1}$ present a larger (or smaller) transition frequency; this effect is comparable to a relatively large local magnetic field of over 25 mT. This serves as a first numerical estimate of the sensitivity of these CTs to structural or vibrational noise and could be related to the intense thermal dependence of T² in this system. [3]

The dependences of tunneling gap (Δ) and curvature (k) as a function of B_4^4 were investigated. We find a local linear dependence in the variational range we applied, which follow the next linear equations: $\Delta = 194.42B_4^4 - 0.31 \text{ cm}^{-1}$, $k = -22446.81B_4^4 + 106.18 \text{ cm}^{-1}/\text{T}^2$.

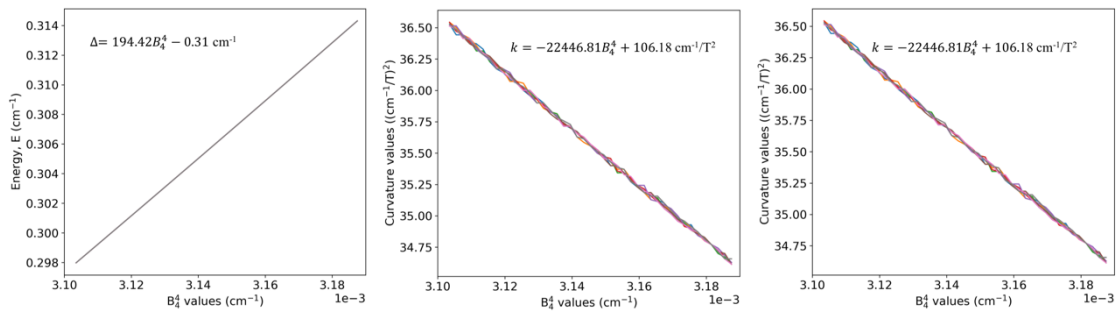


Figure S8: Dependences of Δ and k as a function of B_4^4 . In this variational region both Δ and k follow a linear dependence, with opposite signs.

We also checked the validity of the results comparing the estimated magnetic field values where the CTs are predicted to appear, and the same values empirically obtained in [3].

Table S3: Position of CTs for HoW10 complex. We compare the position at magnetic field the CTs were observed experimentally in a previous study [3] and the position obtained in the present study.

H(experiment [3])	H(theory)
23.5 mT	23.73 mT
70.9 mT	71.2 mT
118 mT	118.67 mT
165 mT	166.13 mT

a. Studies with the Radial Effective Charge (REC) model

In the REC model, the ligand effect is modelled by substituting each atom of the coordination sphere through an effective point charge situated between the lanthanoid ion, in this case Ho^{3+} , and the coordinating atom at a distance R_i from the magnetic center, which is smaller than the real metal-ligand distance (r_i). To account for the effect of covalent electron sharing, a radial displacement vector (D_r) is defined, in which the polar coordinate r of each coordinated atom is collectively varied, $R_i = r_i - D_r$, and at the same time the charge value (Z_i) is scanned in order to achieve a minimum deviation between calculated and experimental data, whereas θ_i and φ_i remain constant.

In the present case, we employed the REC parameters $D_r = 0.8$, $Z_i = 0.197$ obtained in a previous work as the result of a simultaneous and satisfactory fit of the tunneling splitting as determined by EPR measurements and the first two excited doublets as obtained by Inelastic Neutron Scattering experiments. [4]

S4. Cubic symmetry: expanding the anticrossing taxonomy

We performed a moderate axial compression up to 1% ($\Delta z/z$, where the field is applied in B_z). We extracted the initial the REC corrected parameters from [5].

The following collection of graphs show the results of the vertical compression for each calculation, from the maximum compressed structure (1% of compression in z axis), to the minimum compressed structure. The maximum and minimum of the region which follows a quadratic dependence of each spin level is depicted with diamonds, and the CTs detected are marked with dashed lines of the same color.

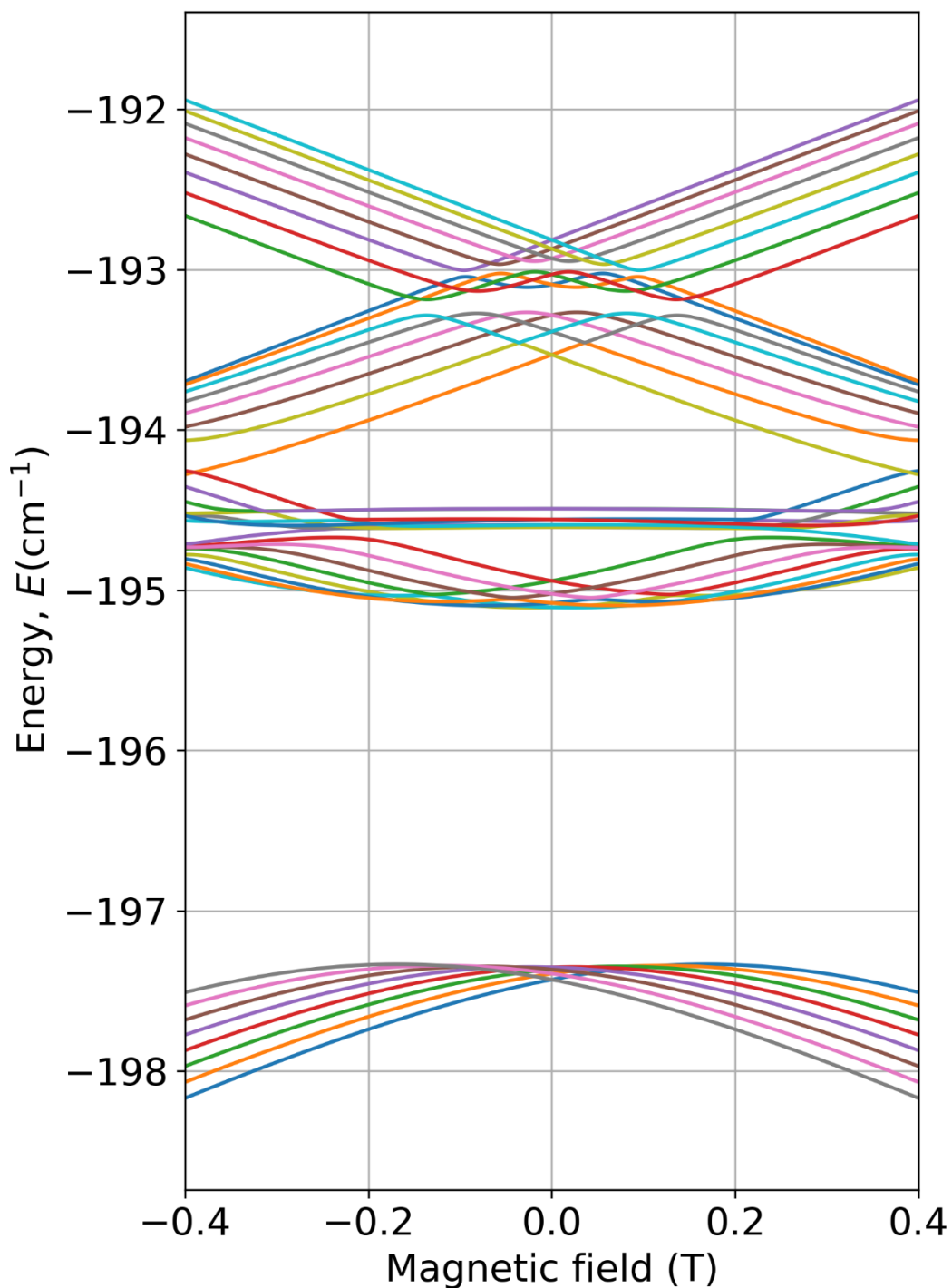


Figure S9: Energy levels splitting for a vertical compression of 1%

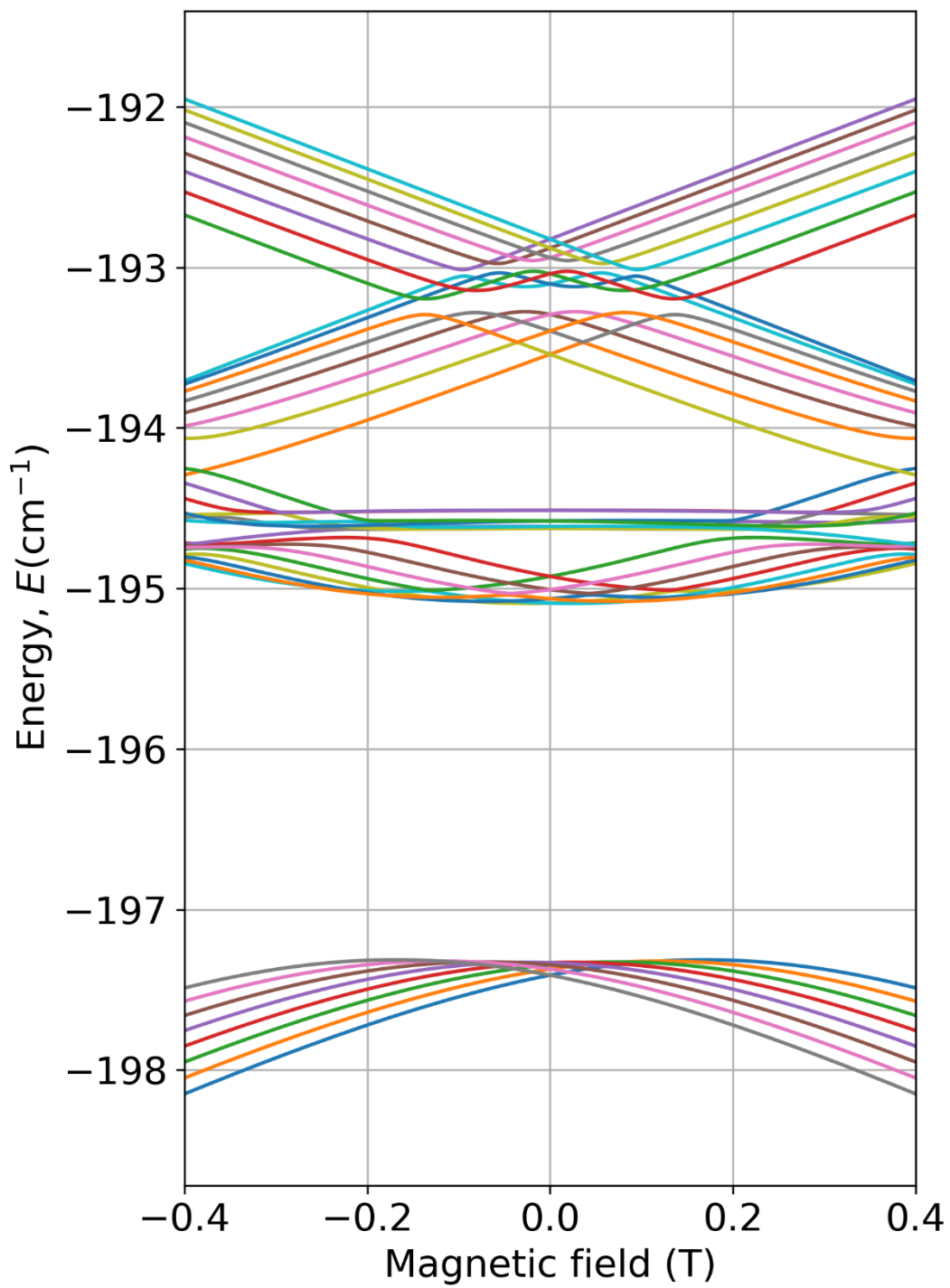


Figure S10: Energy levels splitting for a vertical compression of 0.985%

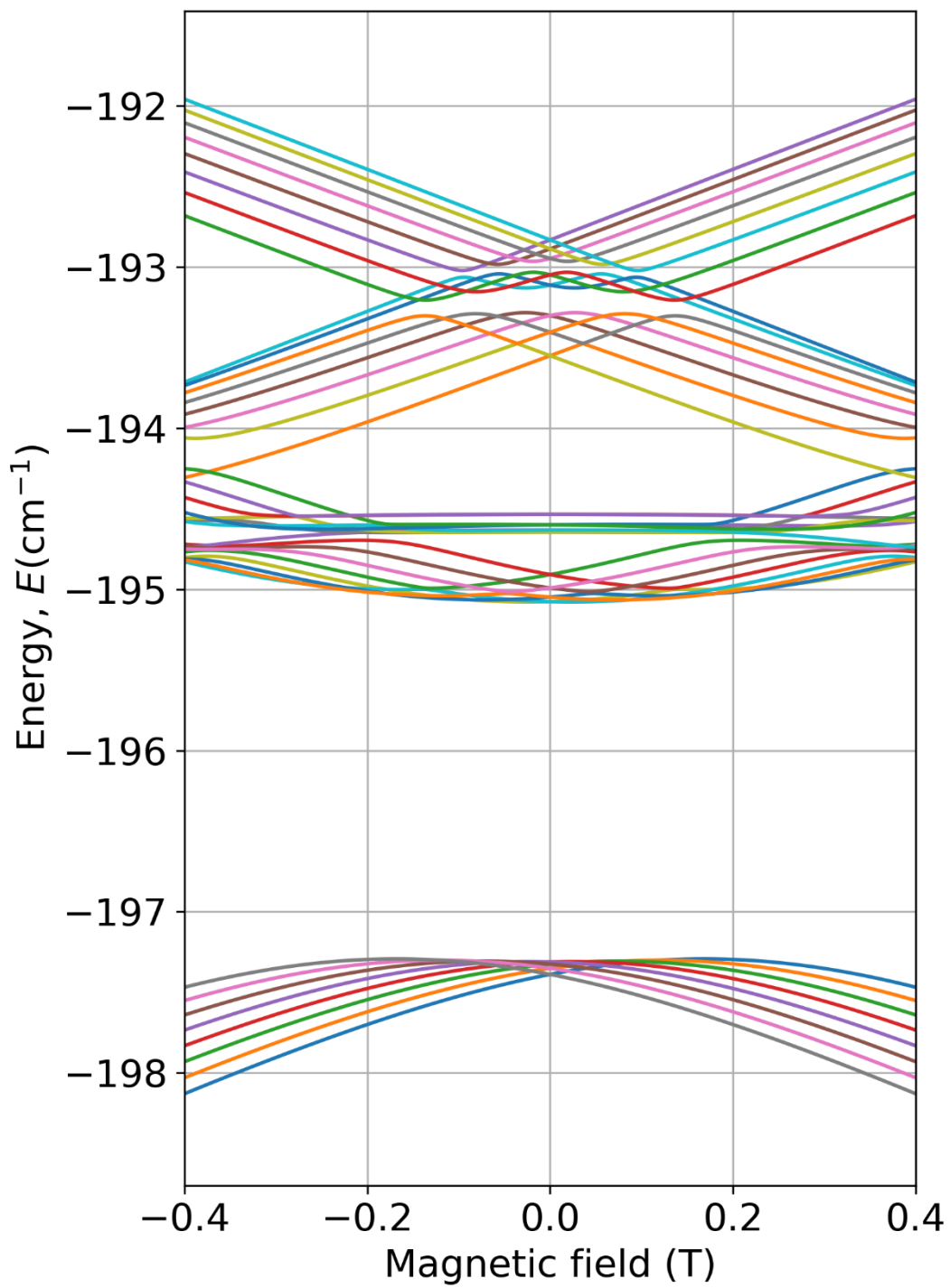


Figure S11: Energy levels splitting for a vertical compression of 0.970%

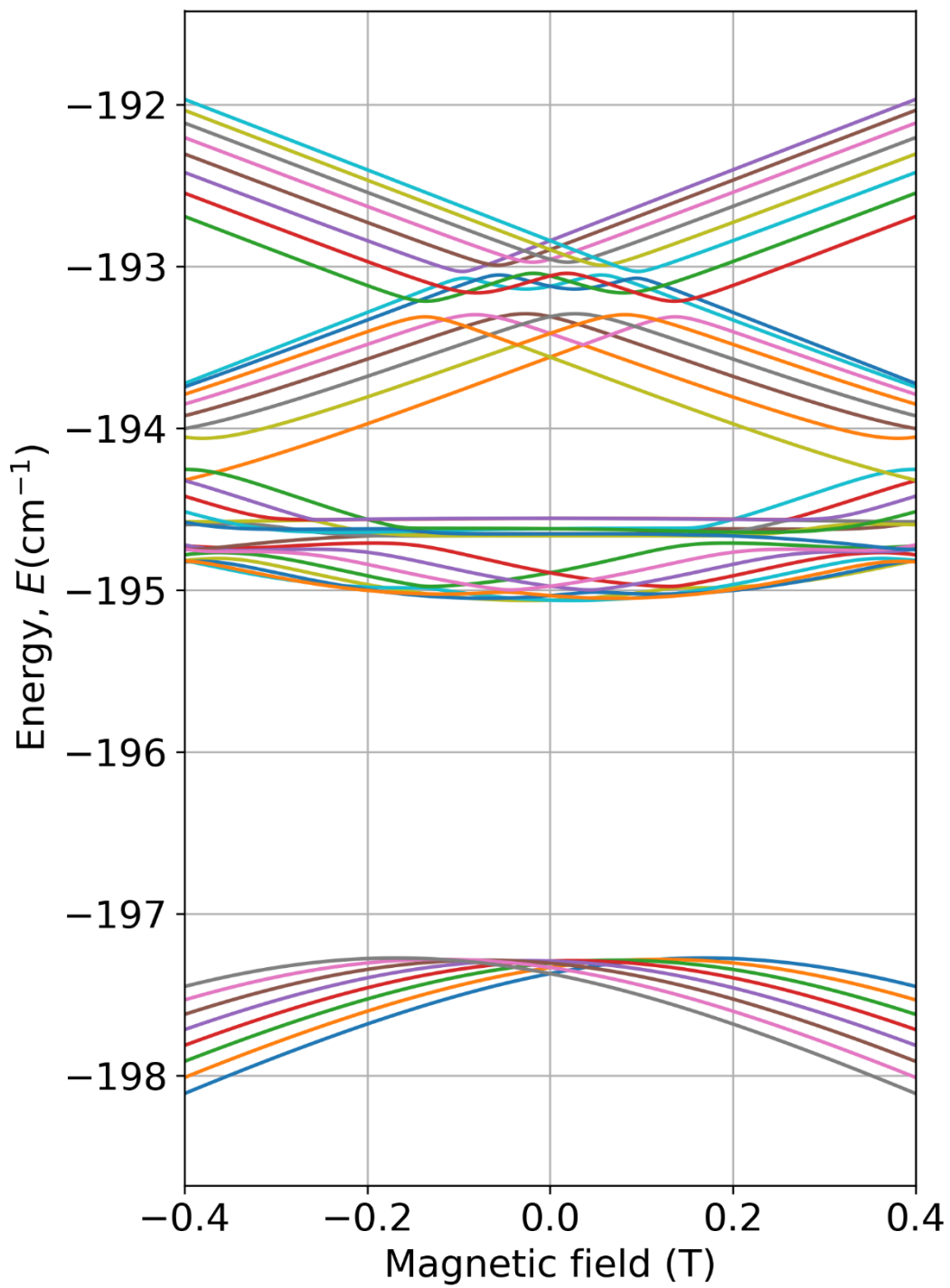


Figure S12: Energy levels splitting for a vertical compression of 0.955%

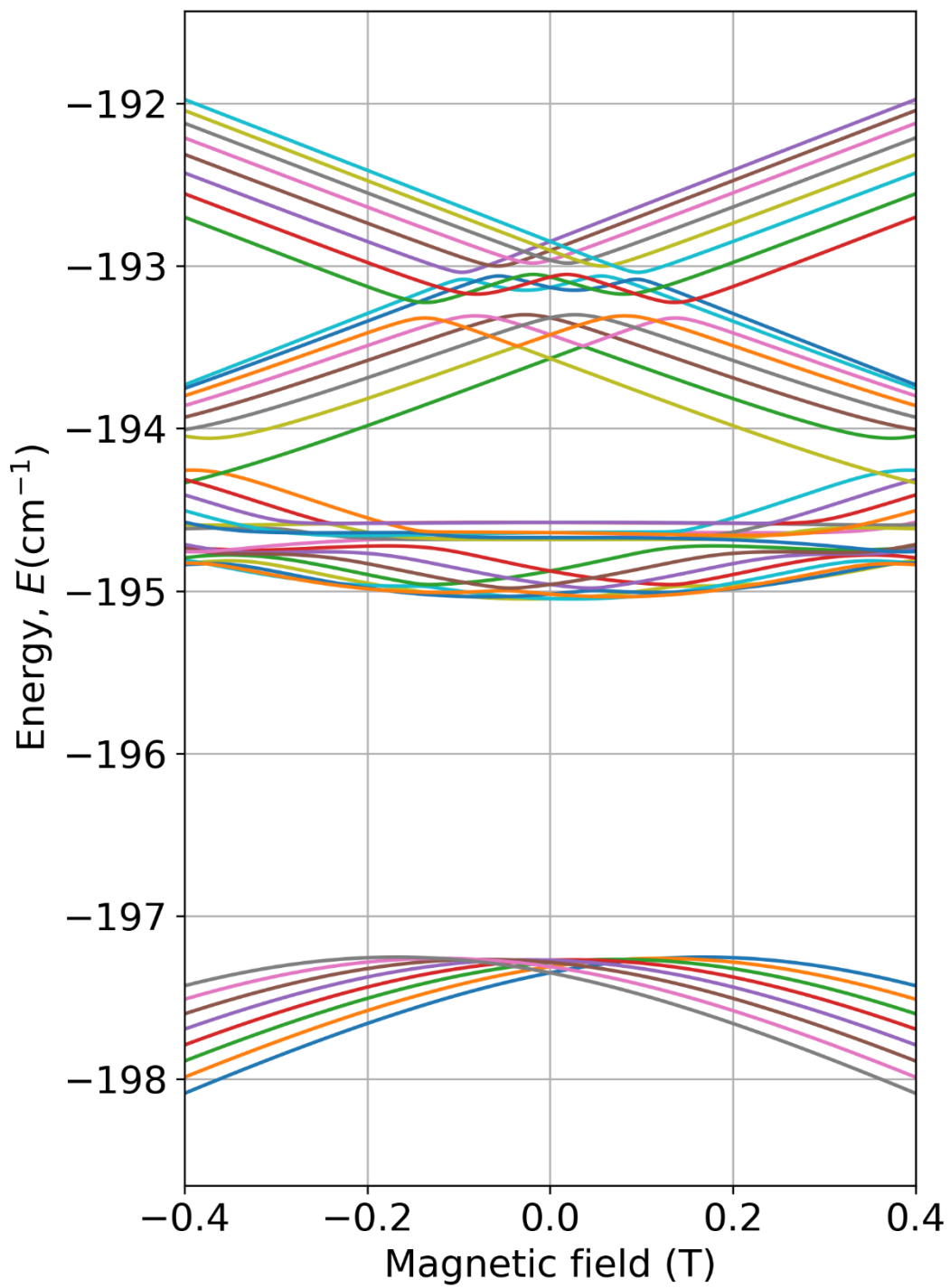


Figure S13: Energy levels splitting for a vertical compression of 0.941%

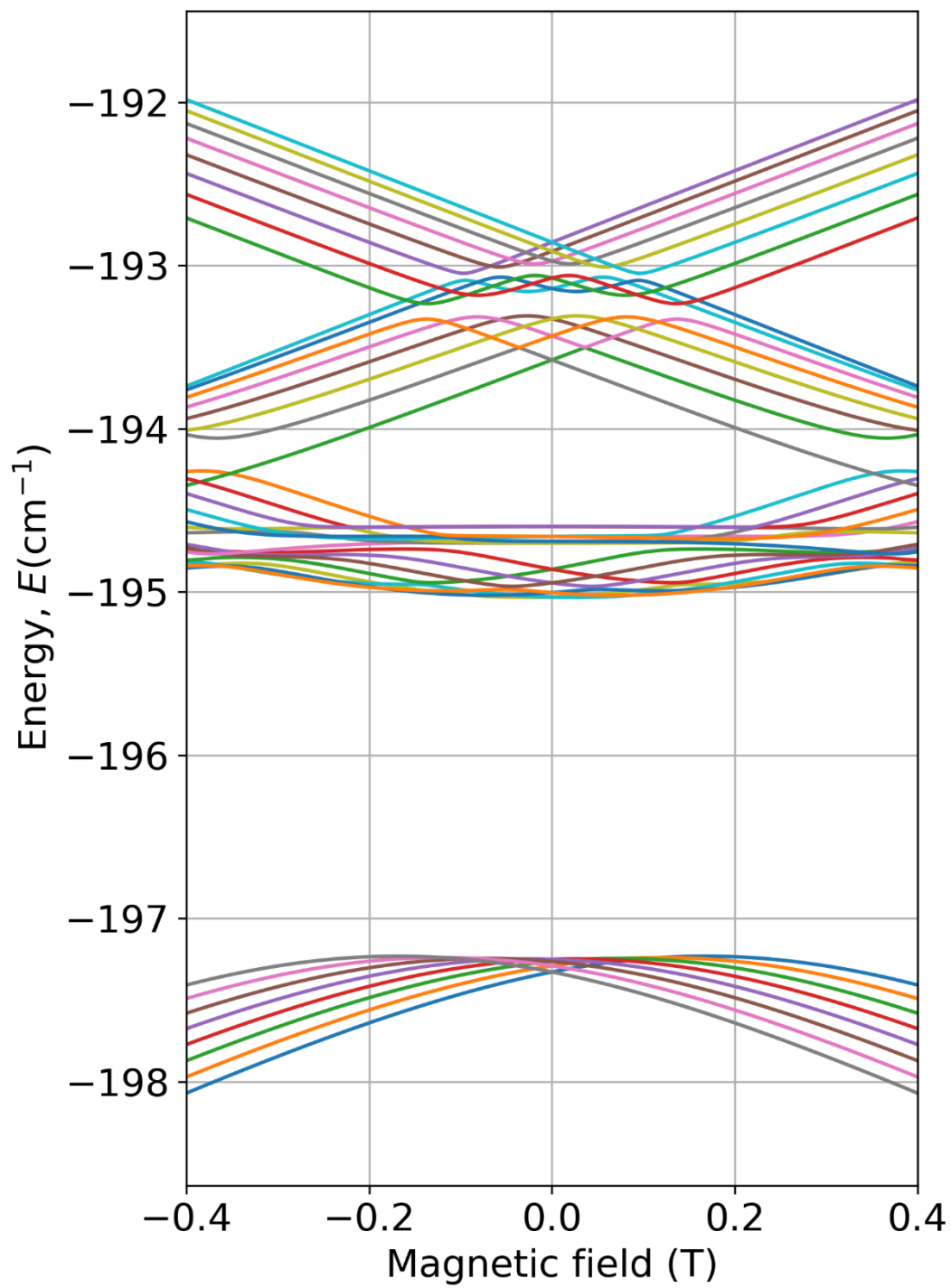


Figure S14: Energy levels splitting for a vertical compression of 0.926%

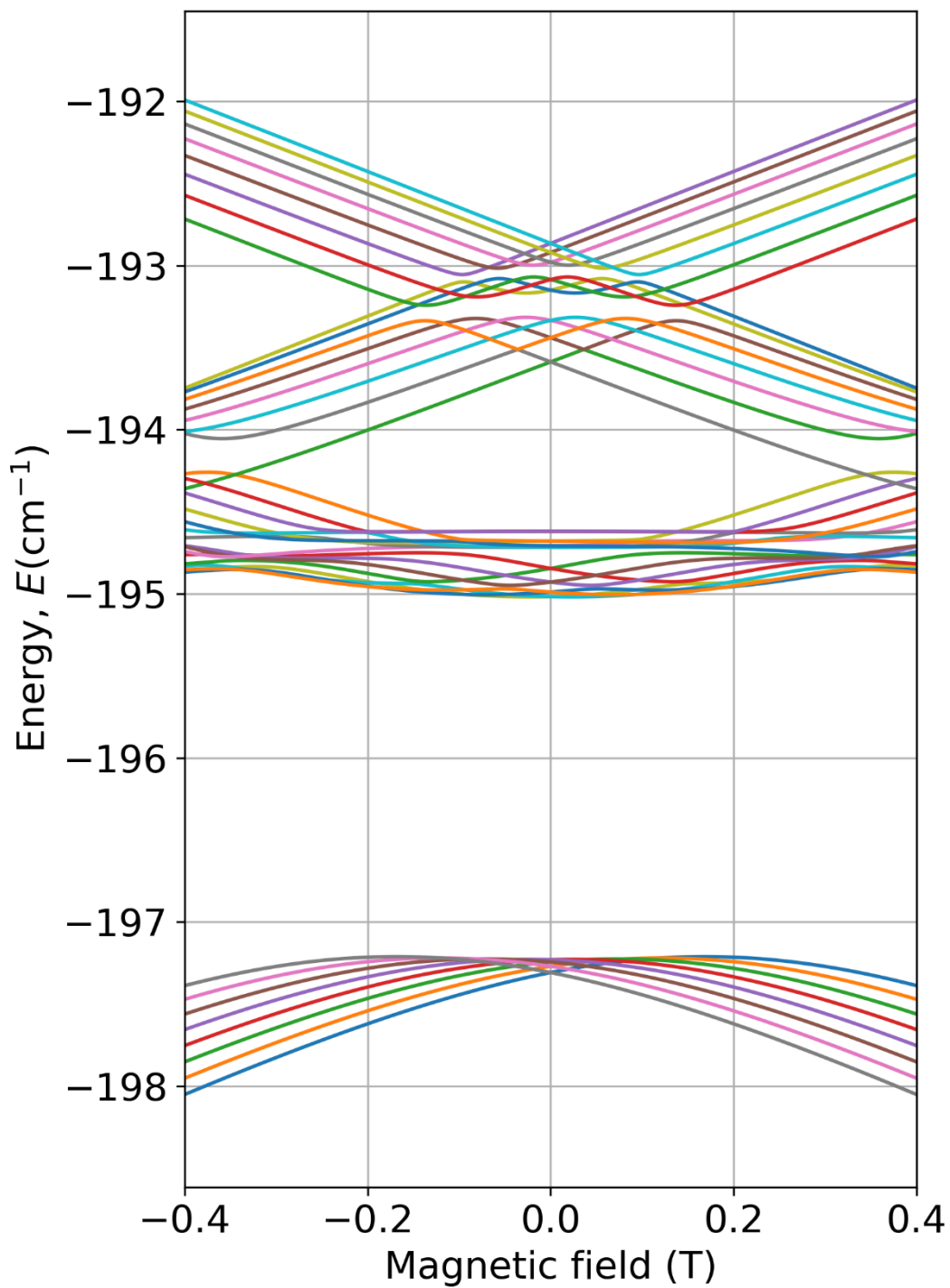


Figure S15: Energy levels splitting for a vertical compression of 0.911%

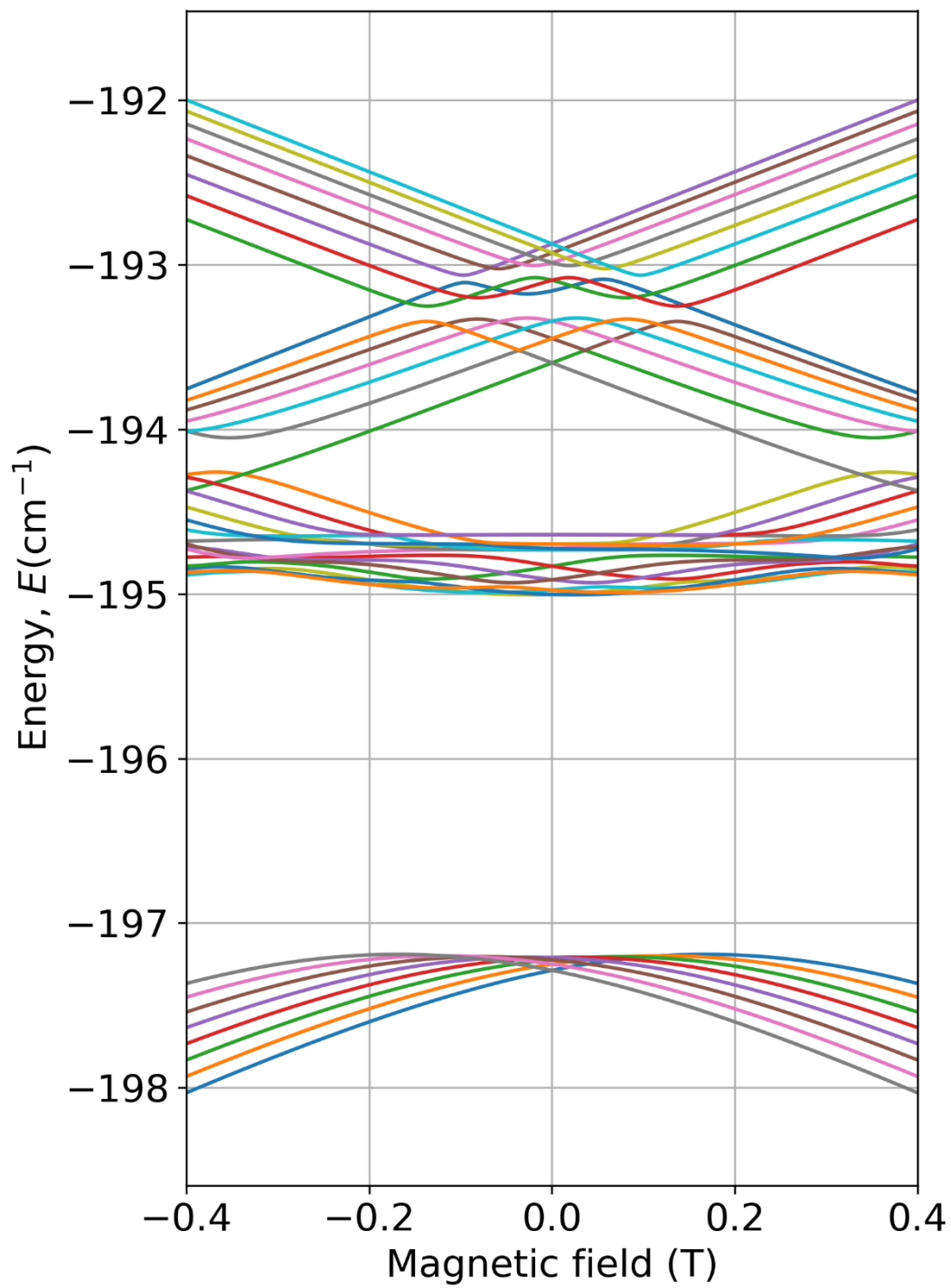


Figure S16: Energy levels splitting for a vertical compression of 0.897%

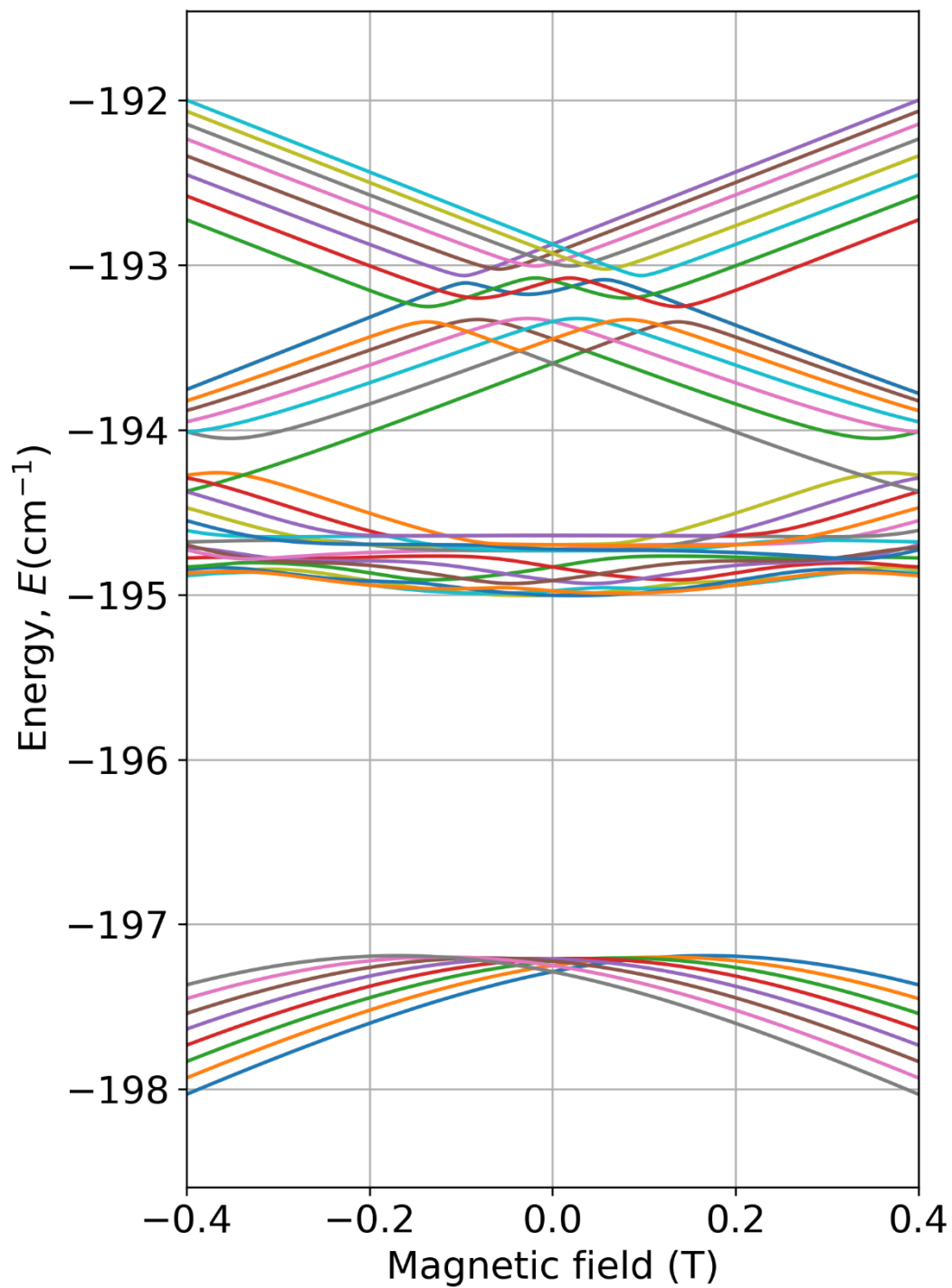


Figure S17: Energy levels splitting for a vertical compression of 0.882%

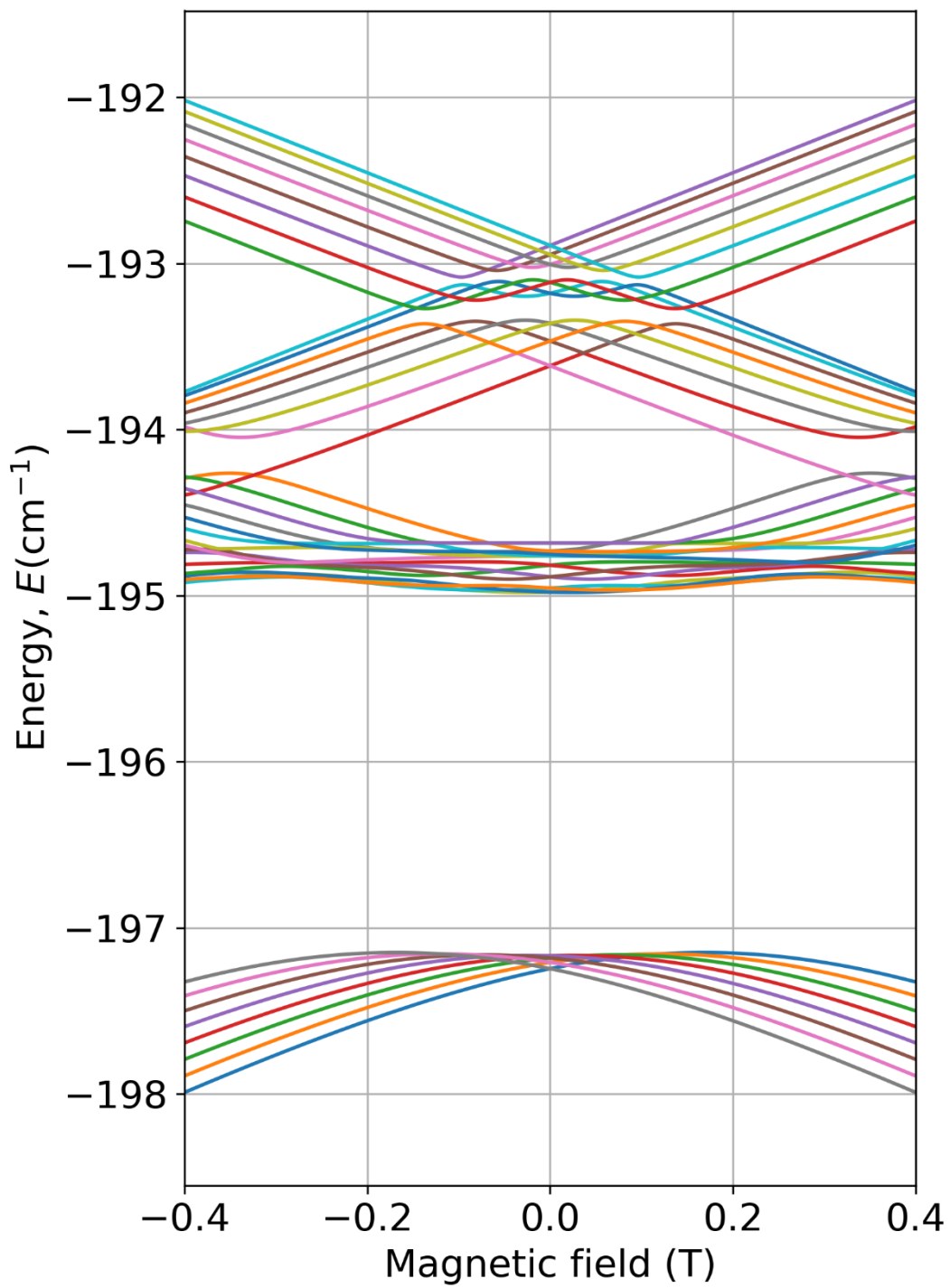


Figure S18: Energy levels splitting for a vertical compression of 0.867%

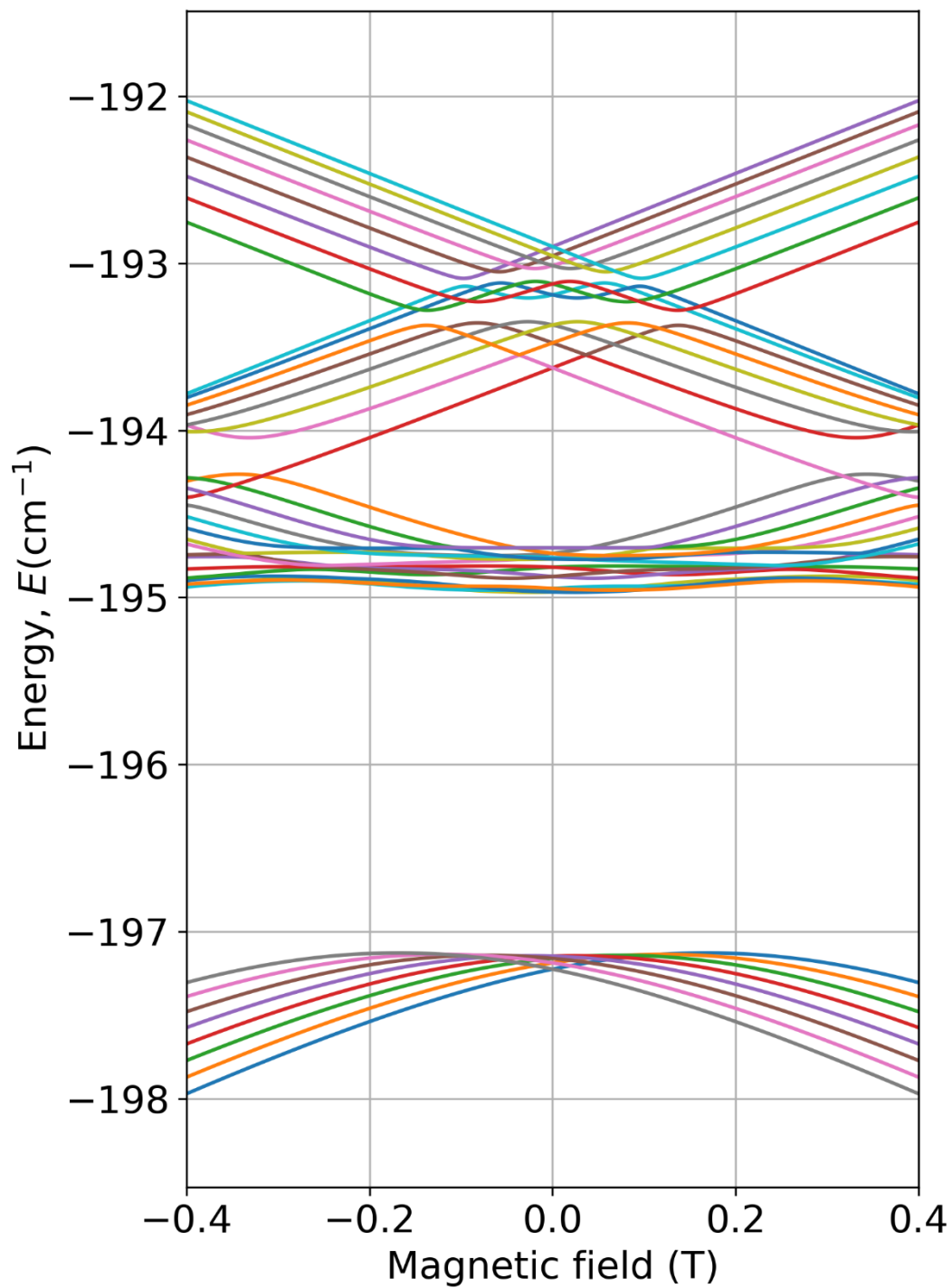


Figure S19: Energy levels splitting for a vertical compression of 0.852%

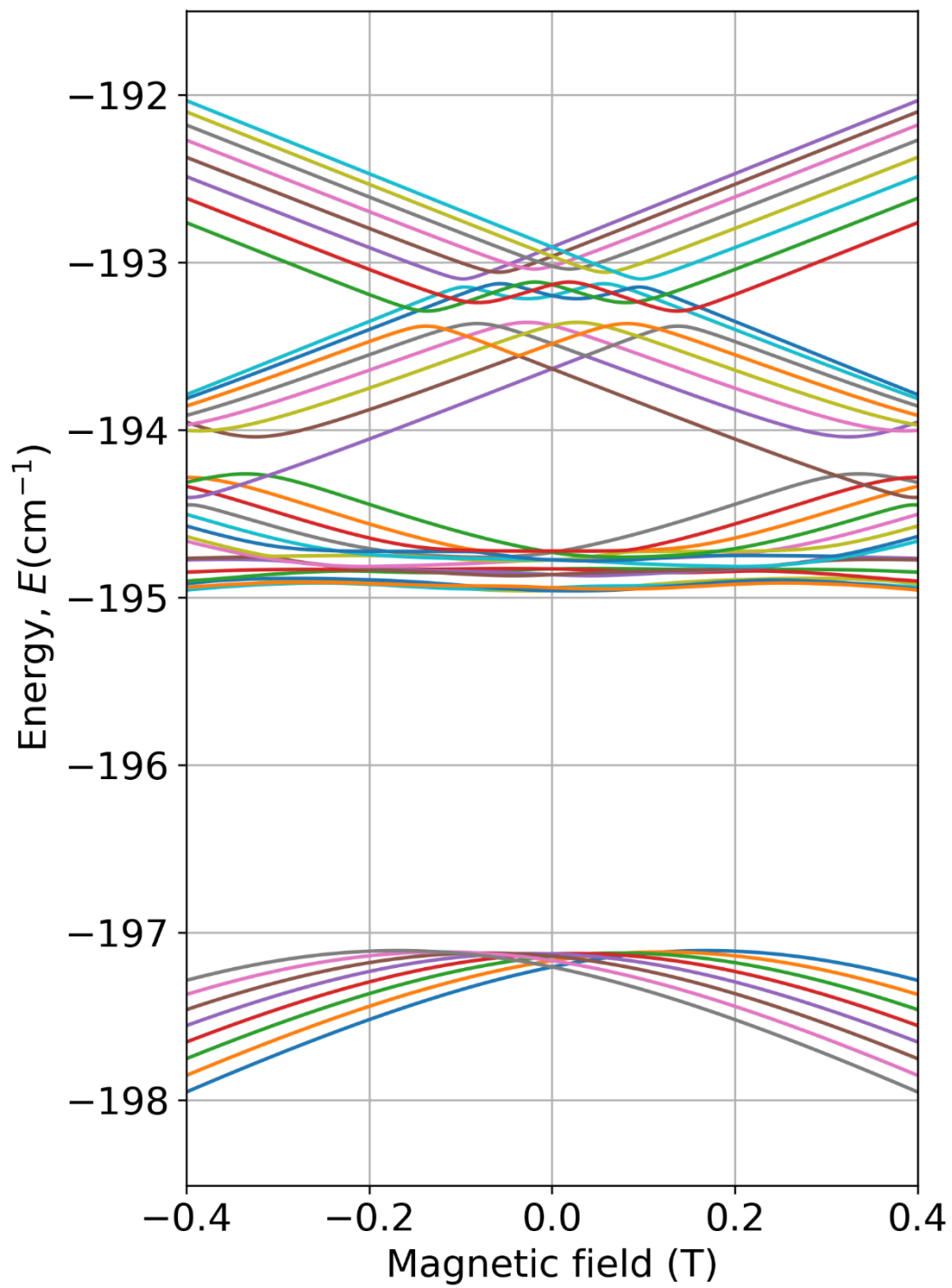


Figure S20: Energy levels splitting for a vertical compression of 0.838%

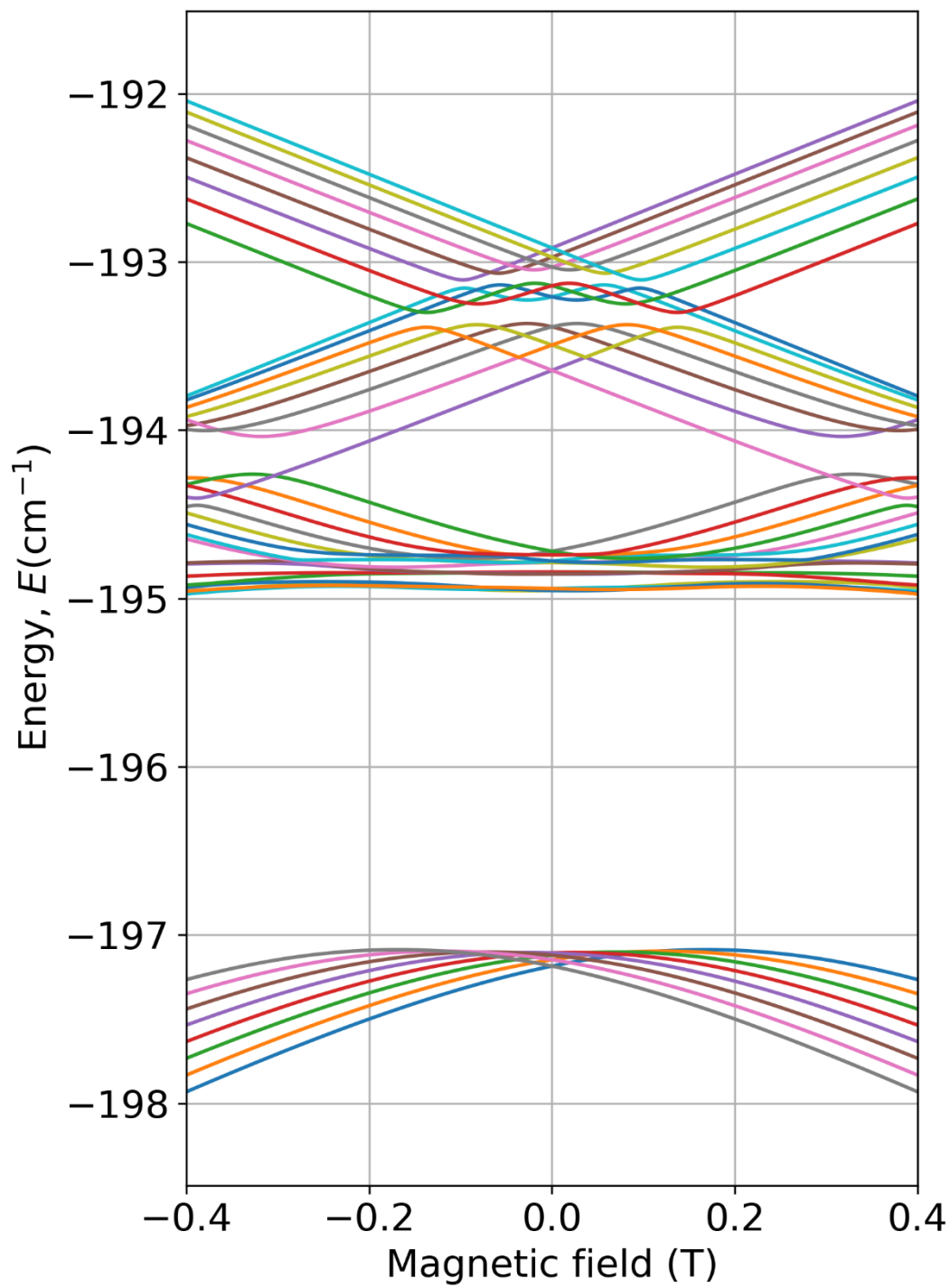


Figure S21: Energy levels splitting for a vertical compression of 0.823%

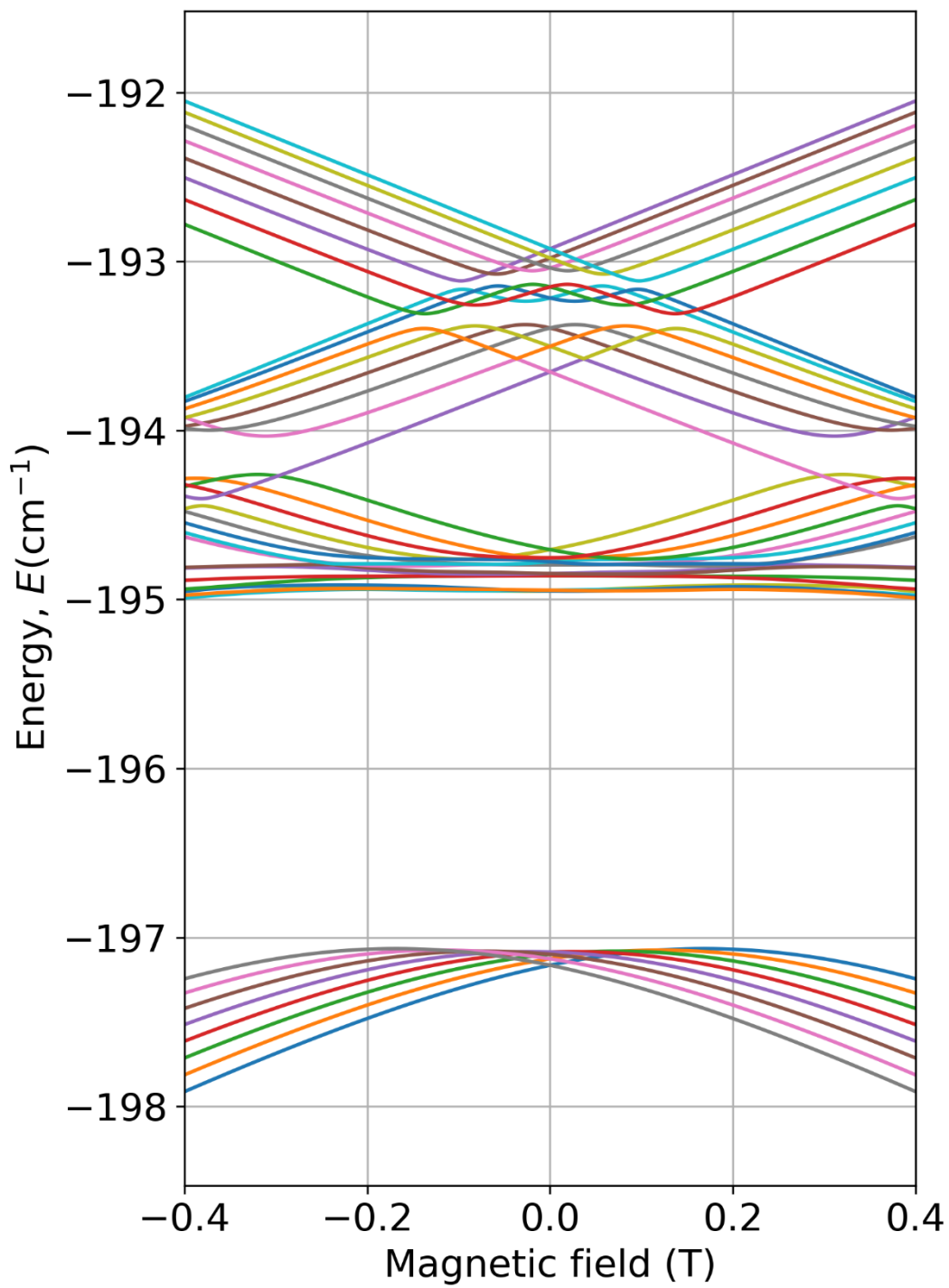


Figure S22: Energy levels splitting for a vertical compression of 0.808%

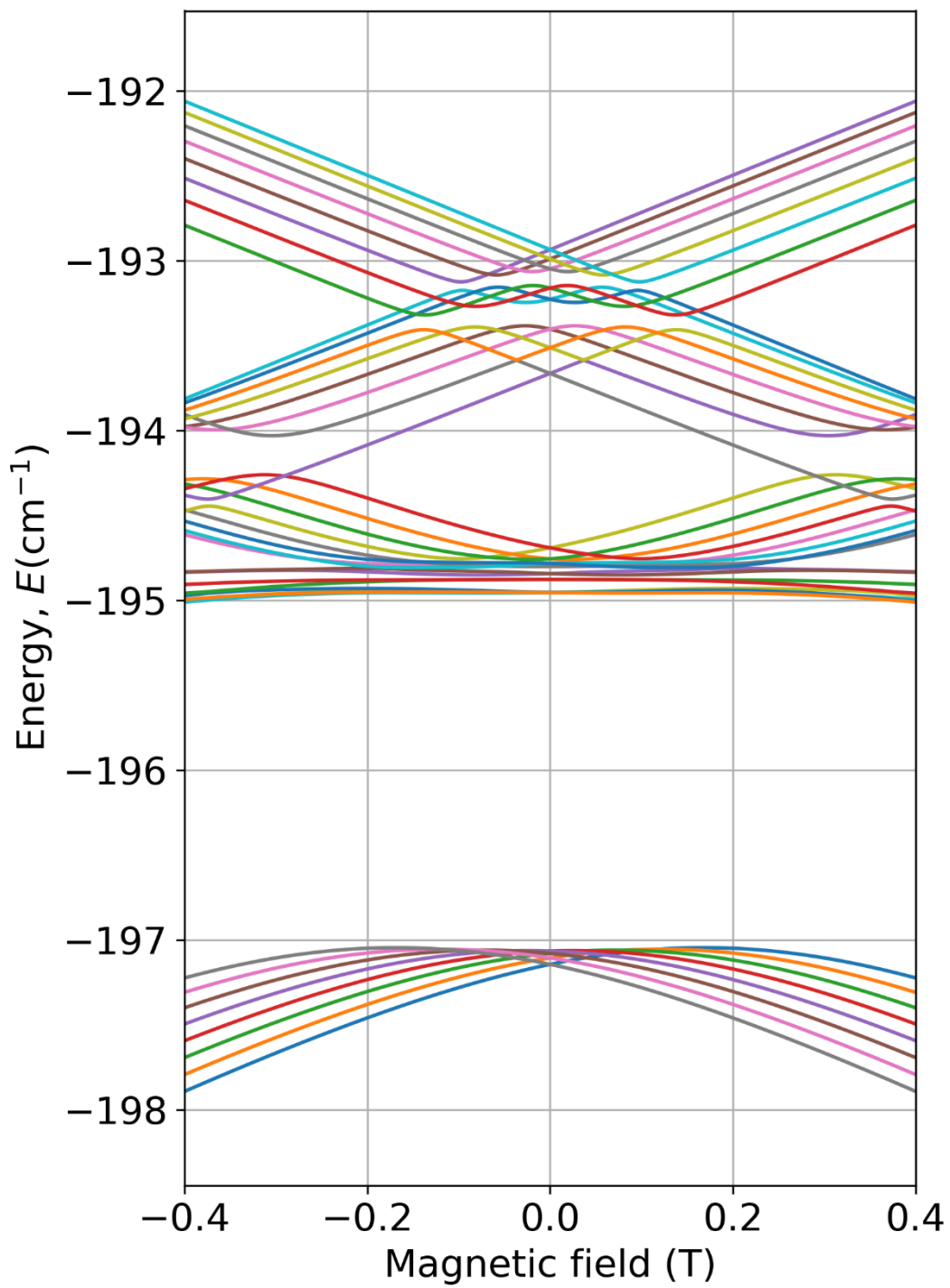


Figure S23: Energy levels splitting for a vertical compression of 0.794%

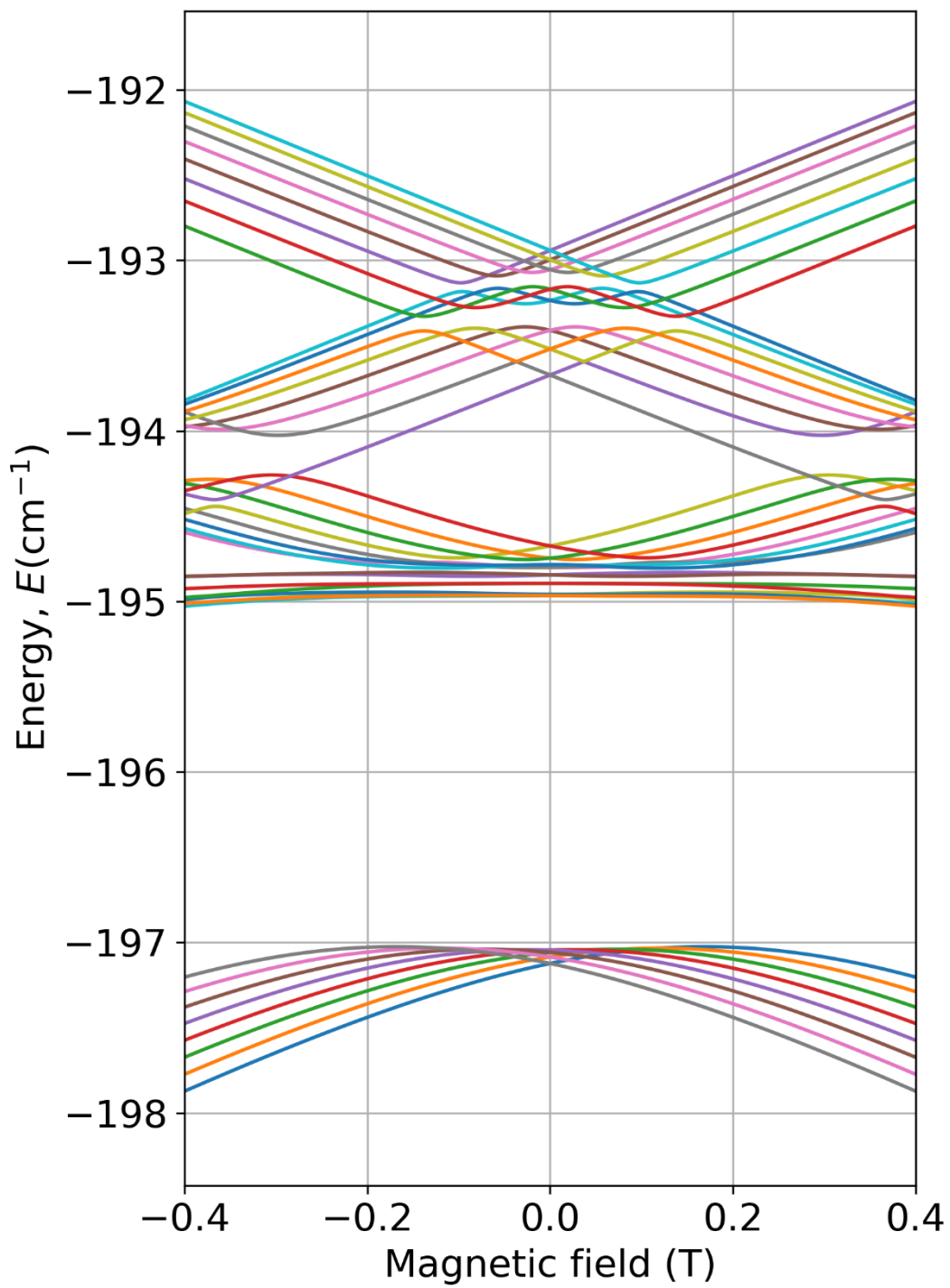


Figure S24: Energy levels splitting for a vertical compression of 0.779%

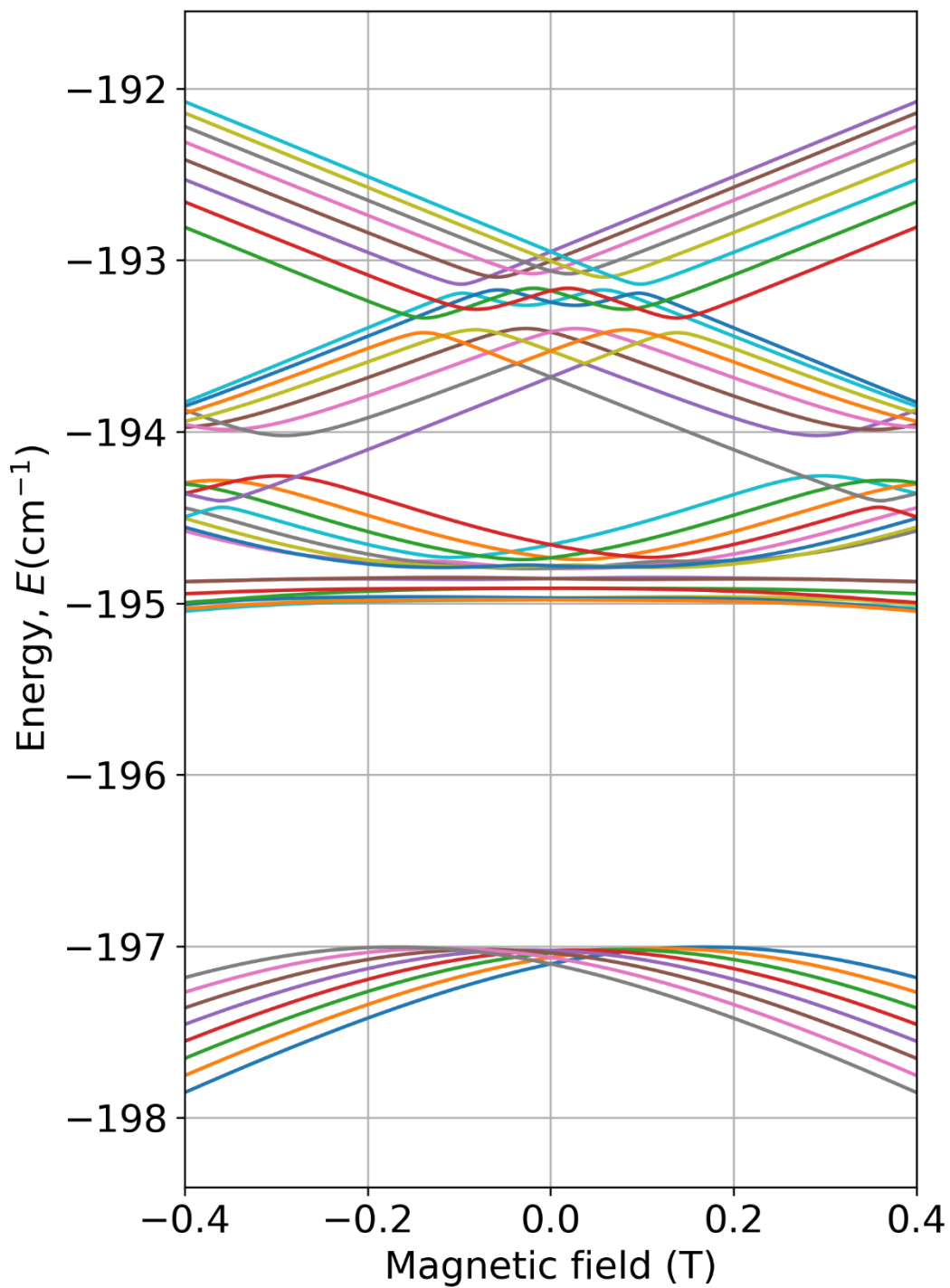


Figure S25: Energy levels splitting for a vertical compression of 0.764%

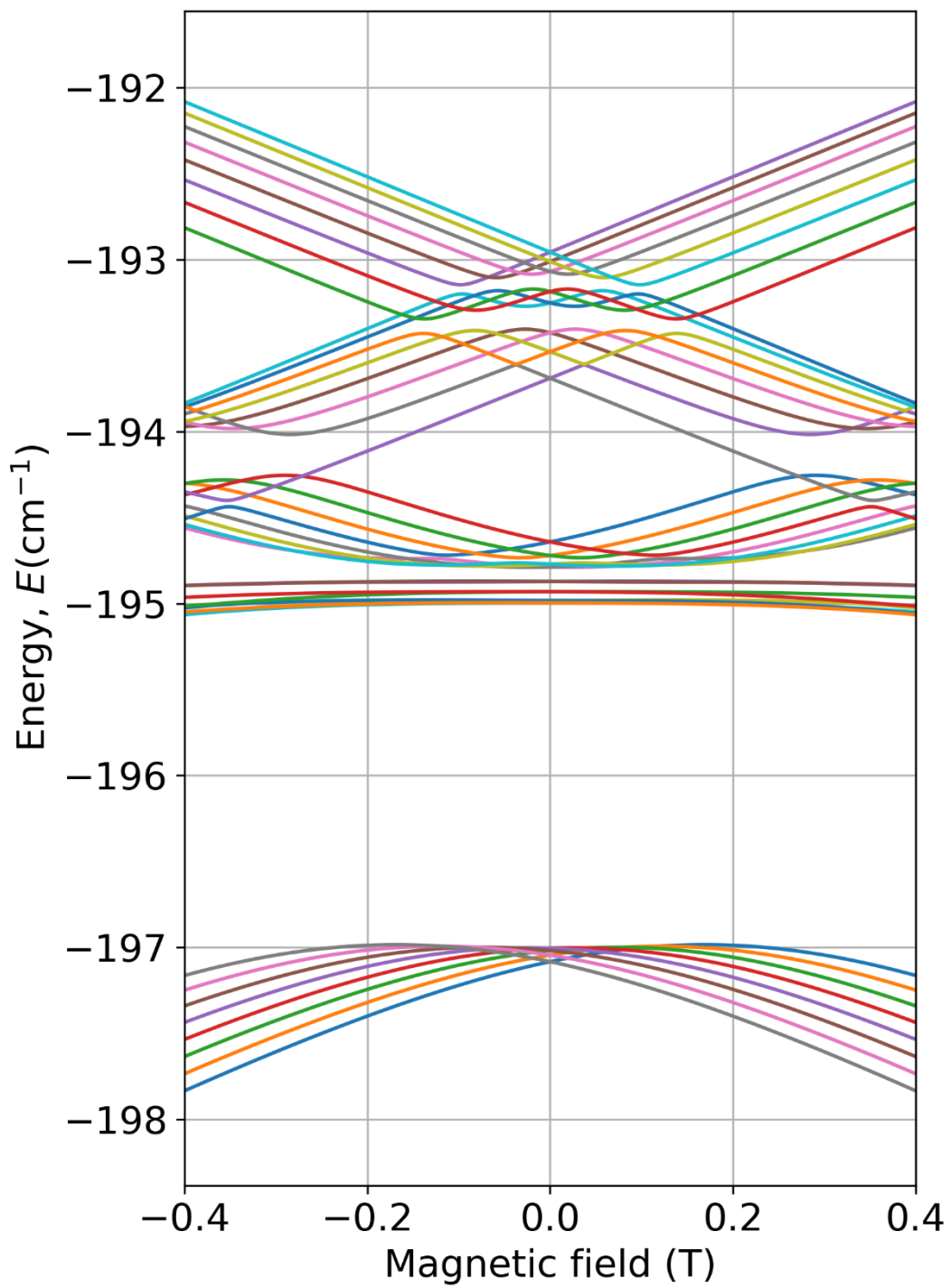


Figure S26: Energy levels splitting for a vertical compression of 0.750%

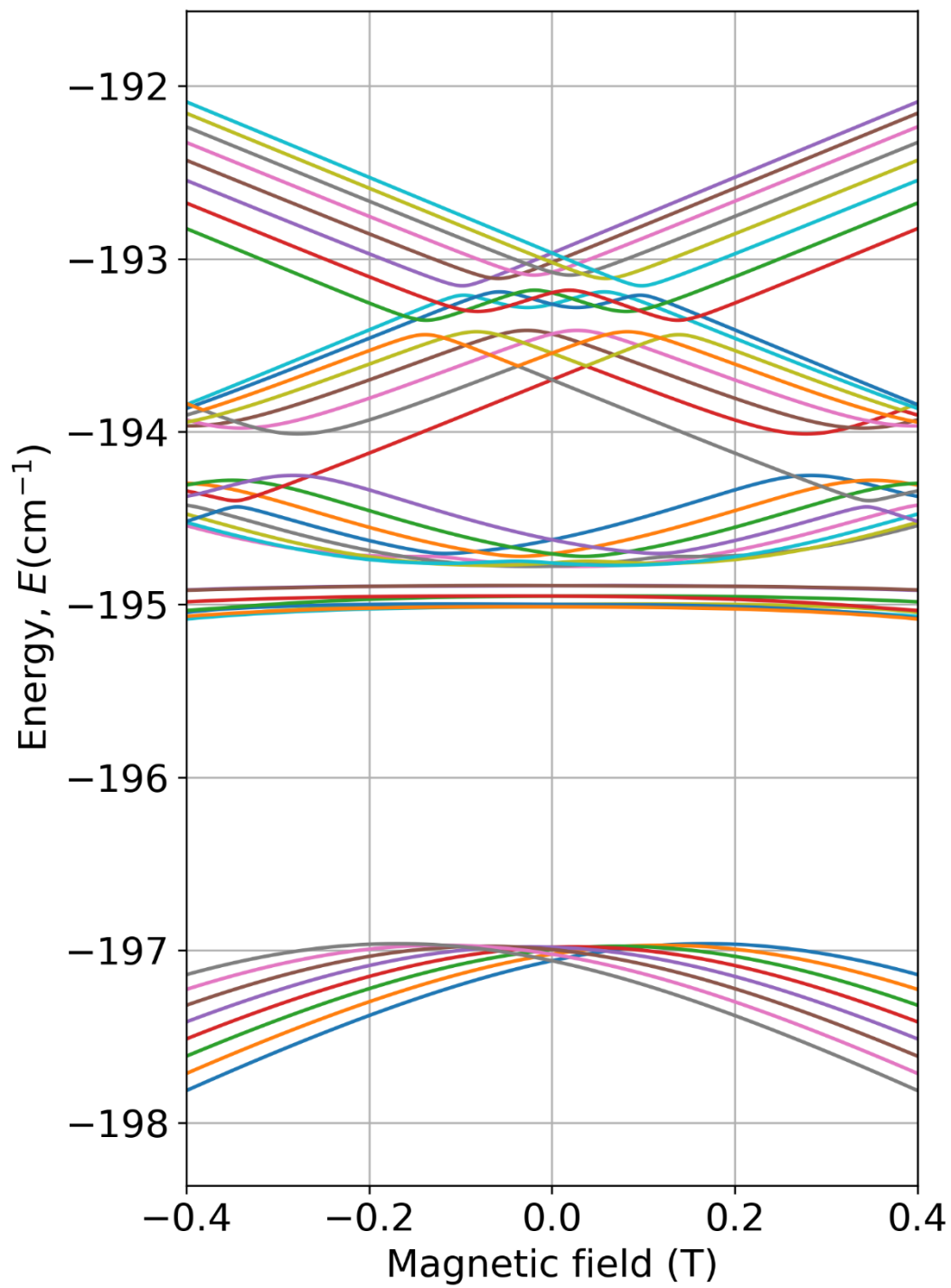


Figure S27: Energy levels splitting for a vertical compression of 0.735%

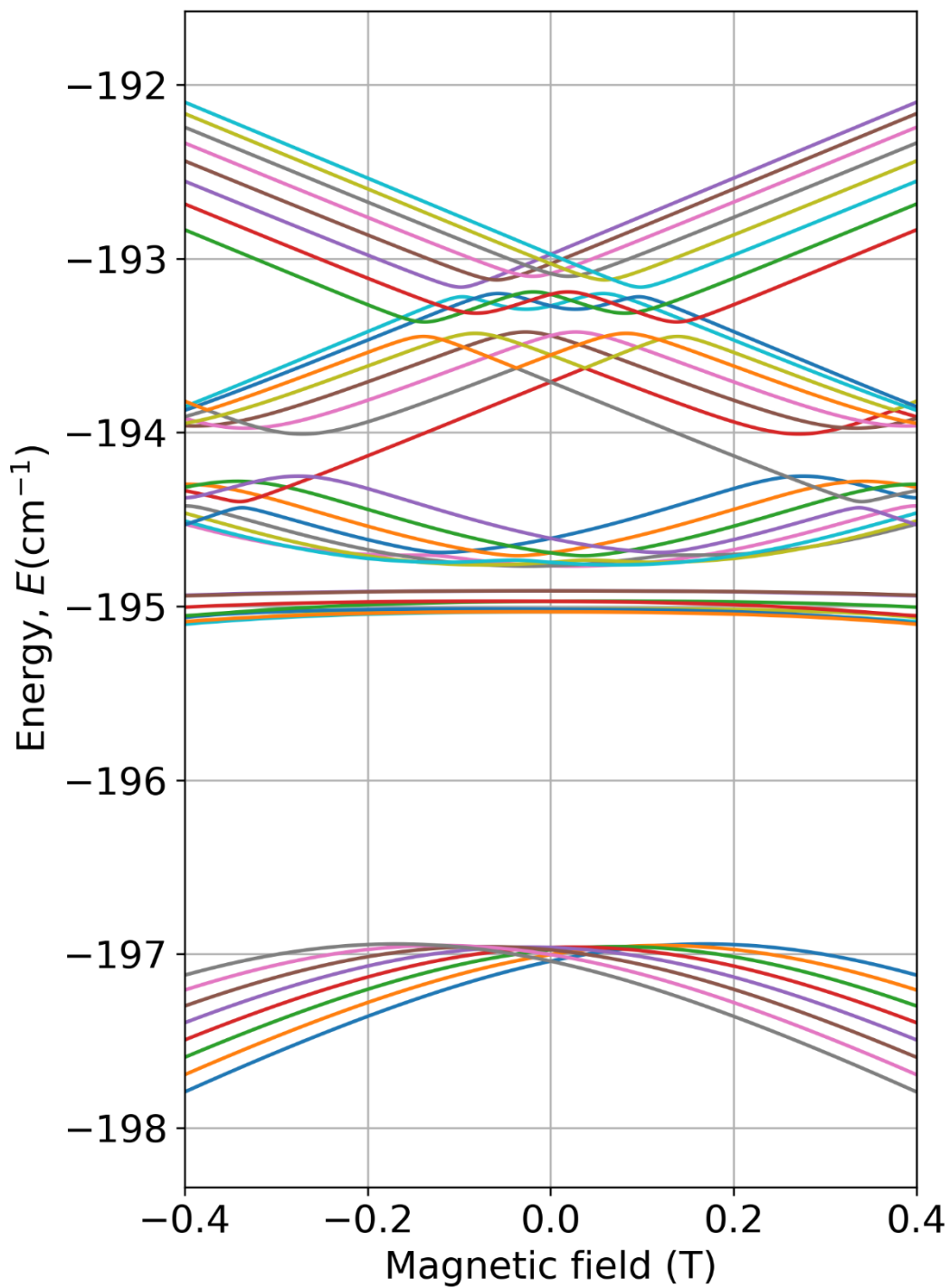


Figure S28: Energy levels splitting for a vertical compression of 0.720%

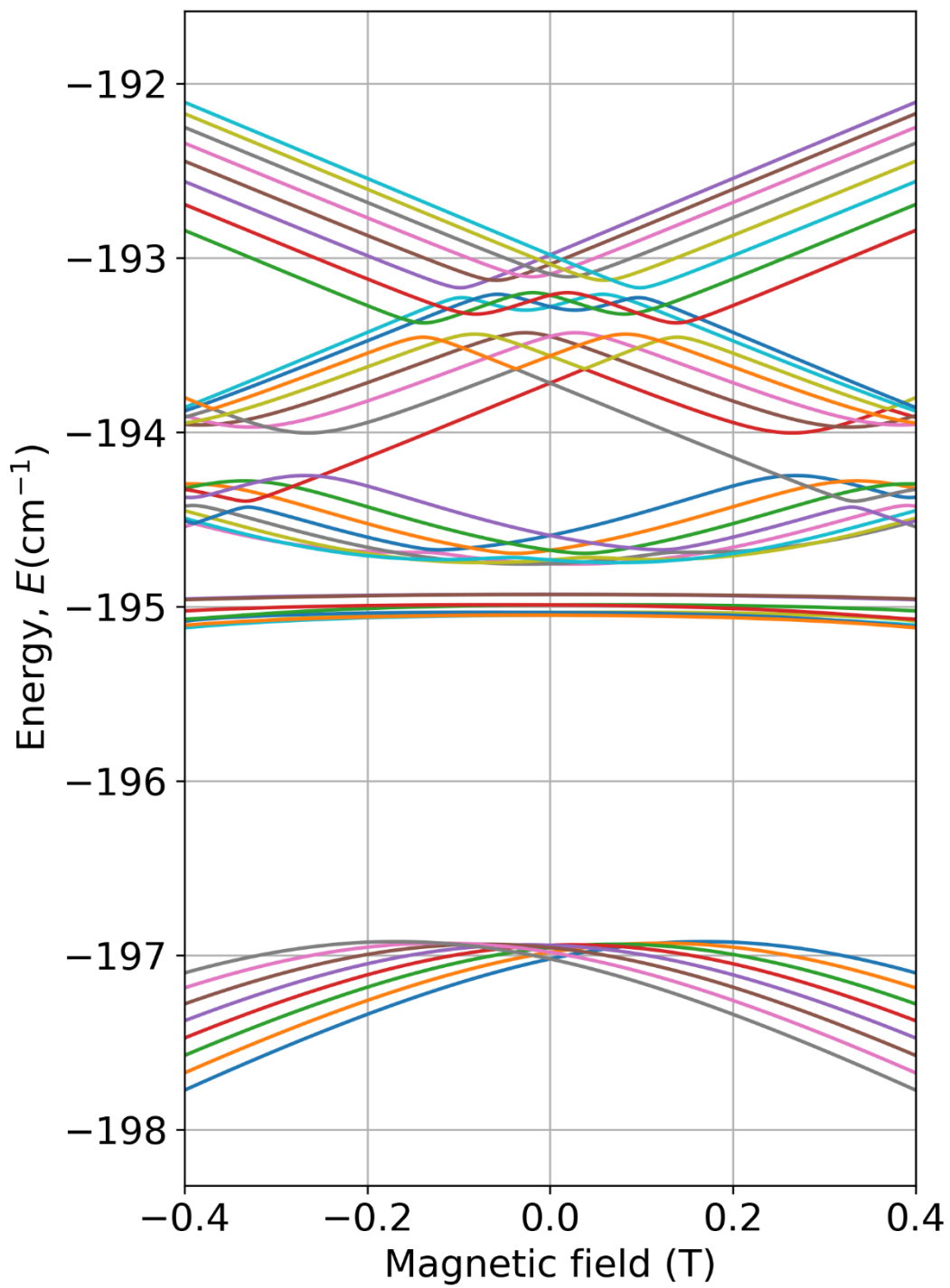


Figure S29: Energy levels splitting for a vertical compression of 0.705%

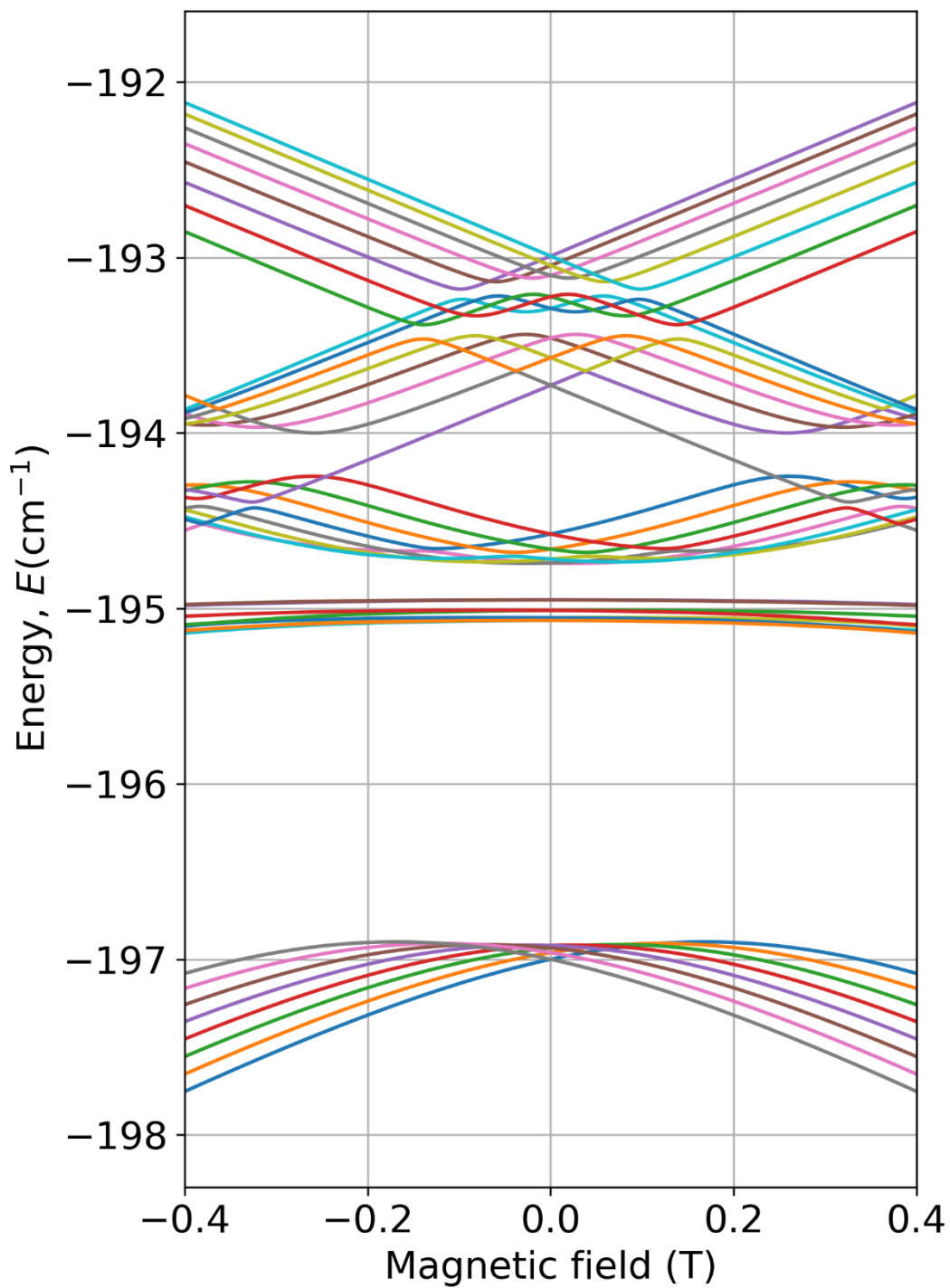


Figure S30: Energy levels splitting for a vertical compression of 0.691%

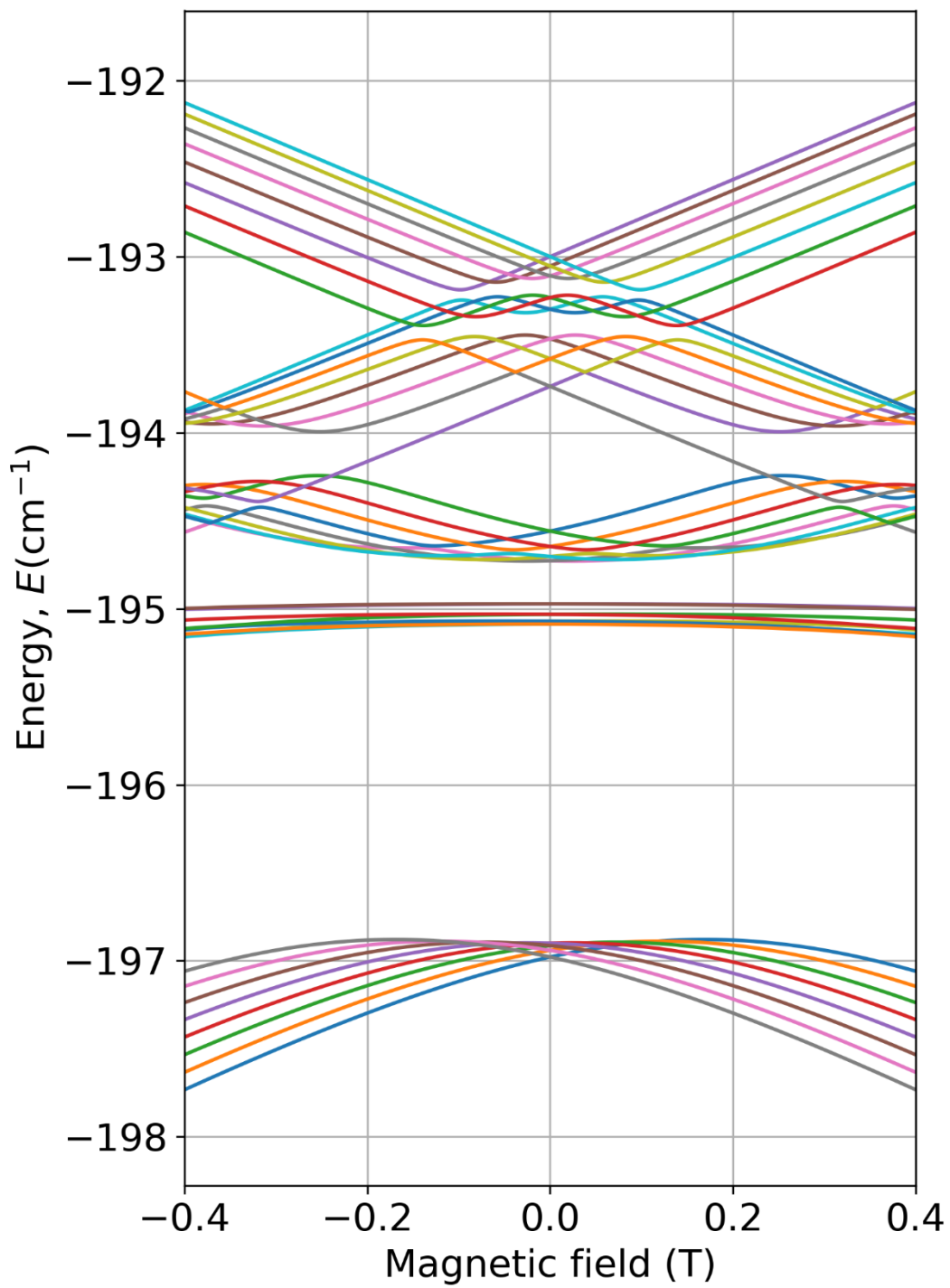


Figure S31: Energy levels splitting for a vertical compression of 0.676%

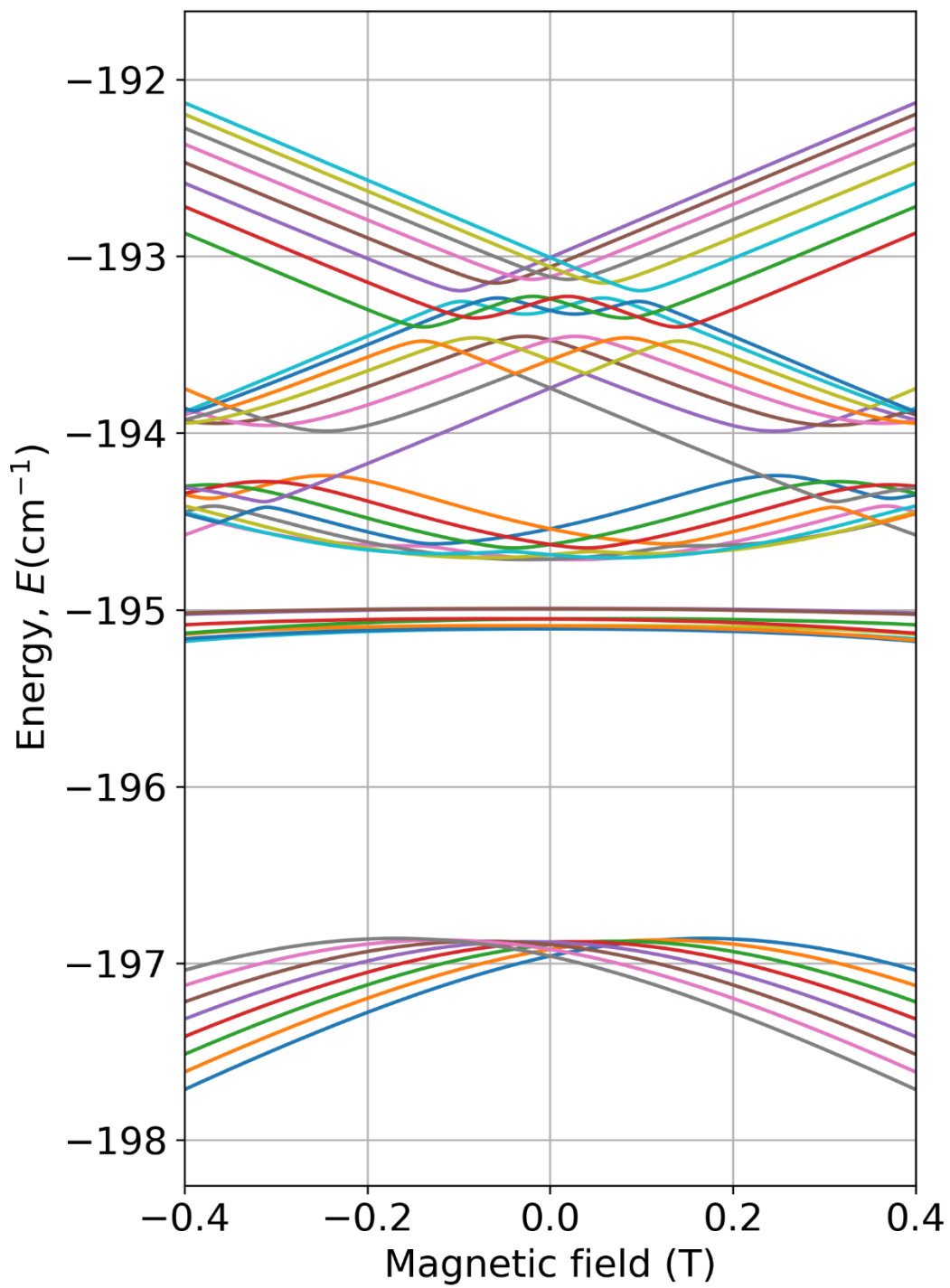


Figure S32: Energy levels splitting for a vertical compression of 0.661%

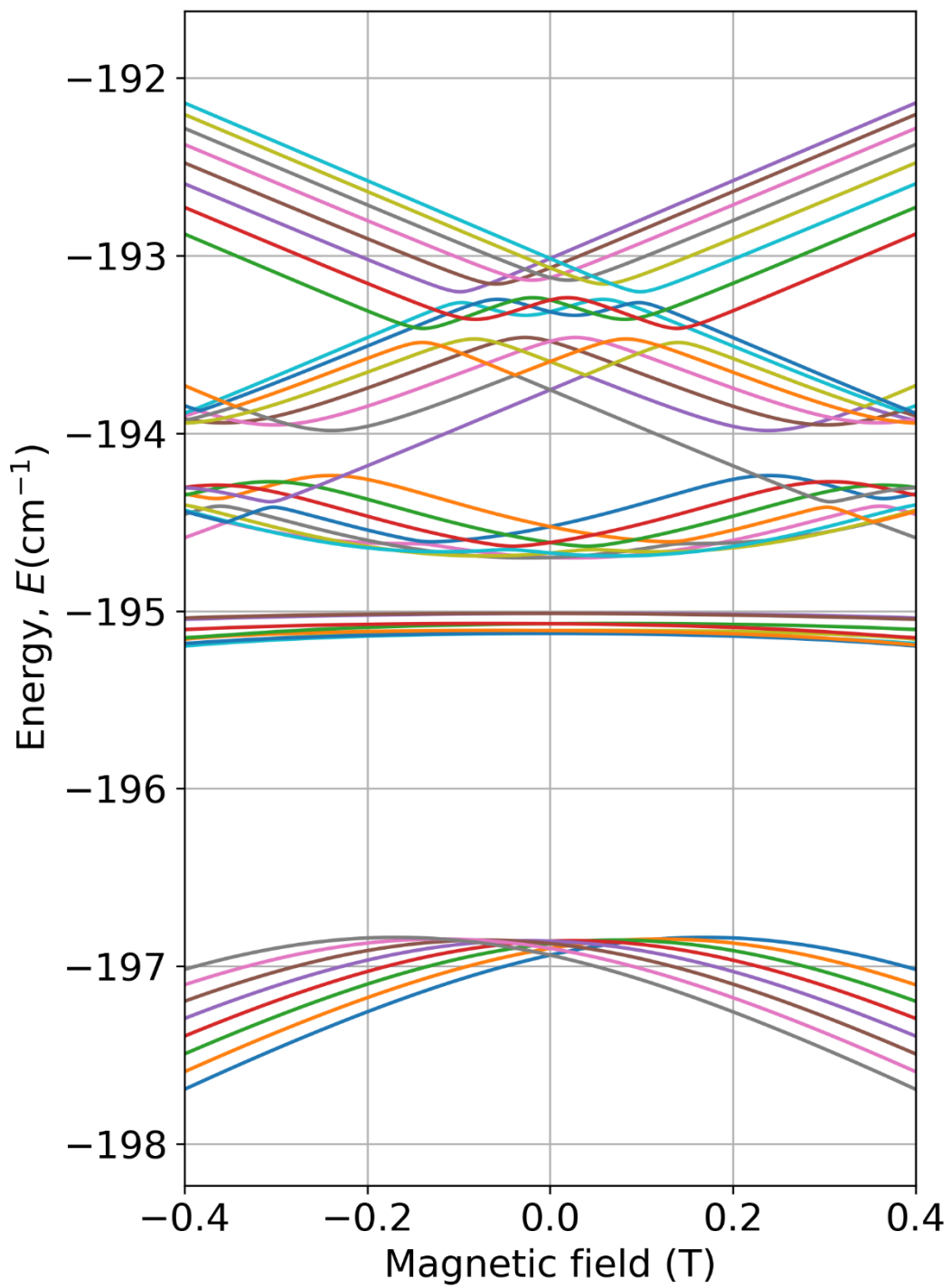


Figure S33: Energy levels splitting for a vertical compression of 0.647%

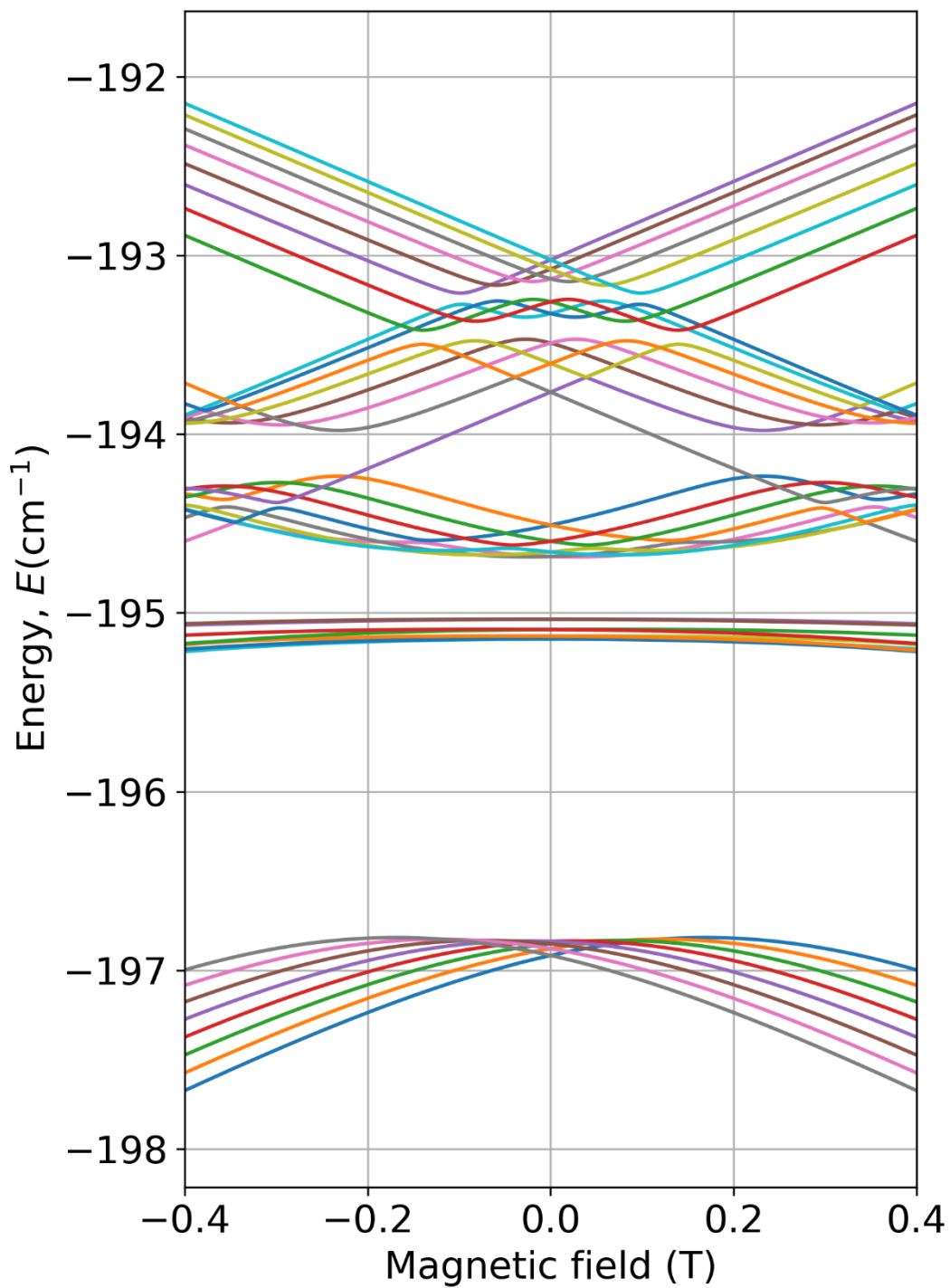


Figure S34: Energy levels splitting for a vertical compression of 0.632%

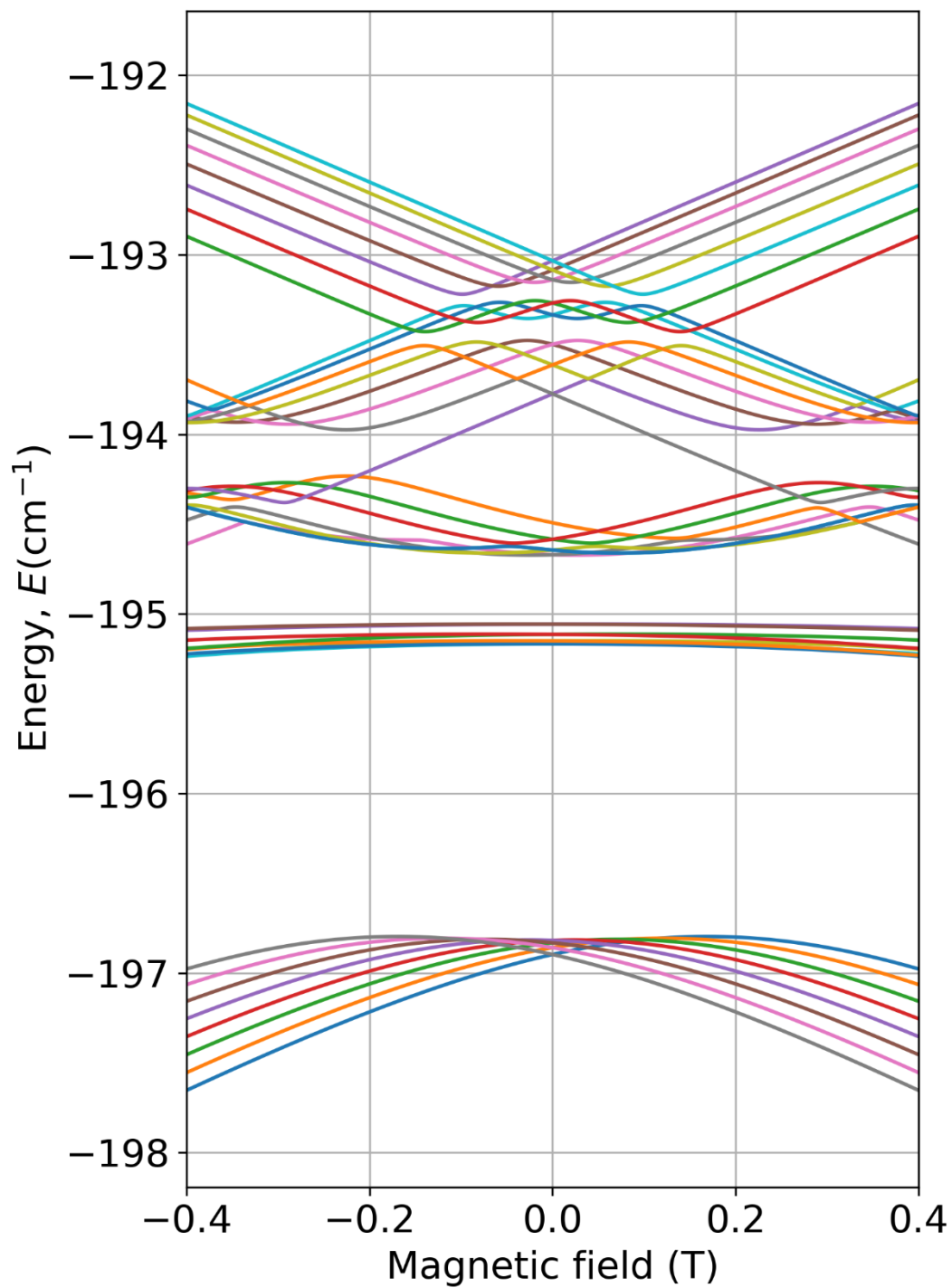


Figure S35: Energy levels splitting for a vertical compression of 0.617%

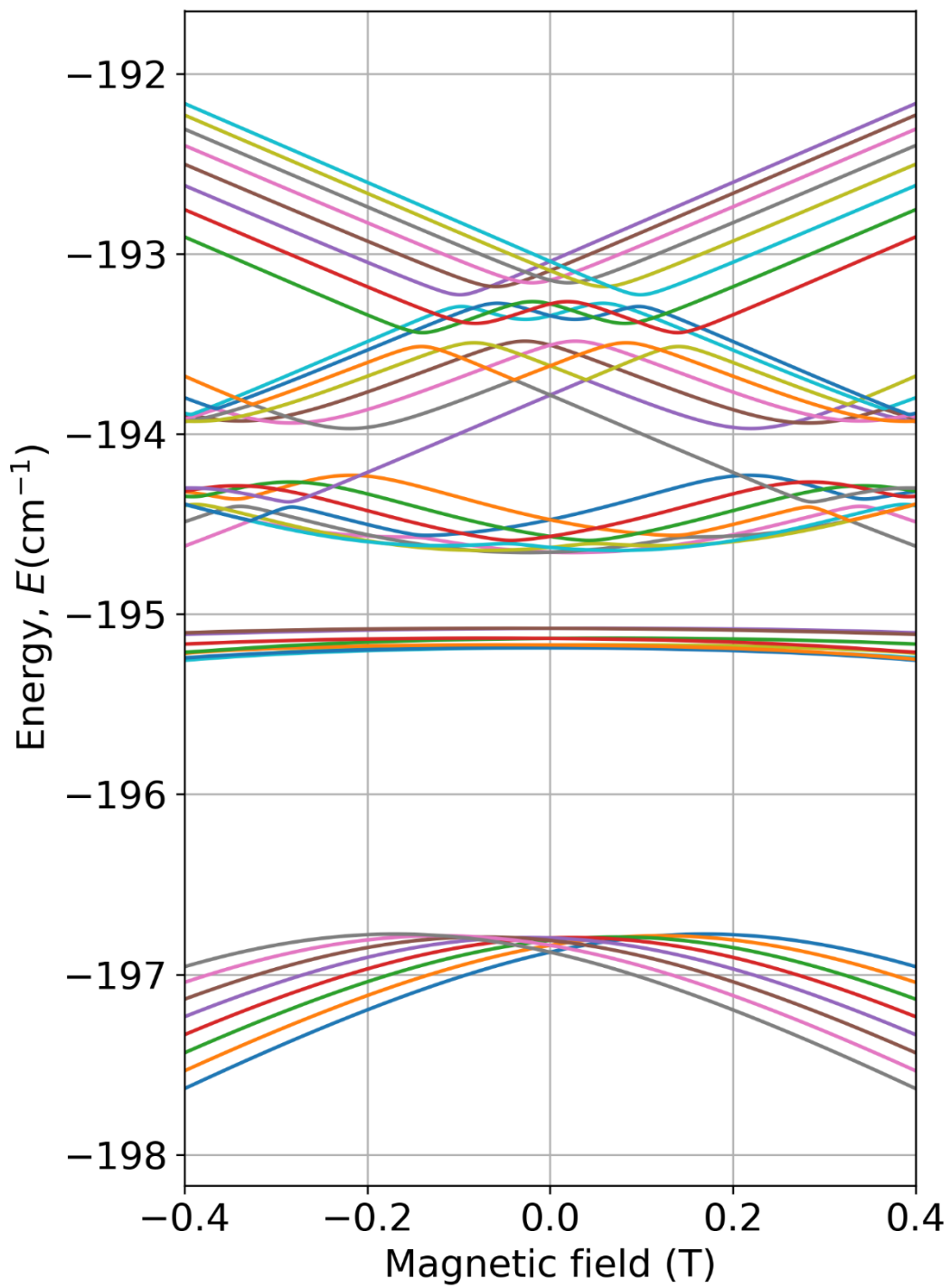


Figure S36: Energy levels splitting for a vertical compression of 0.603%

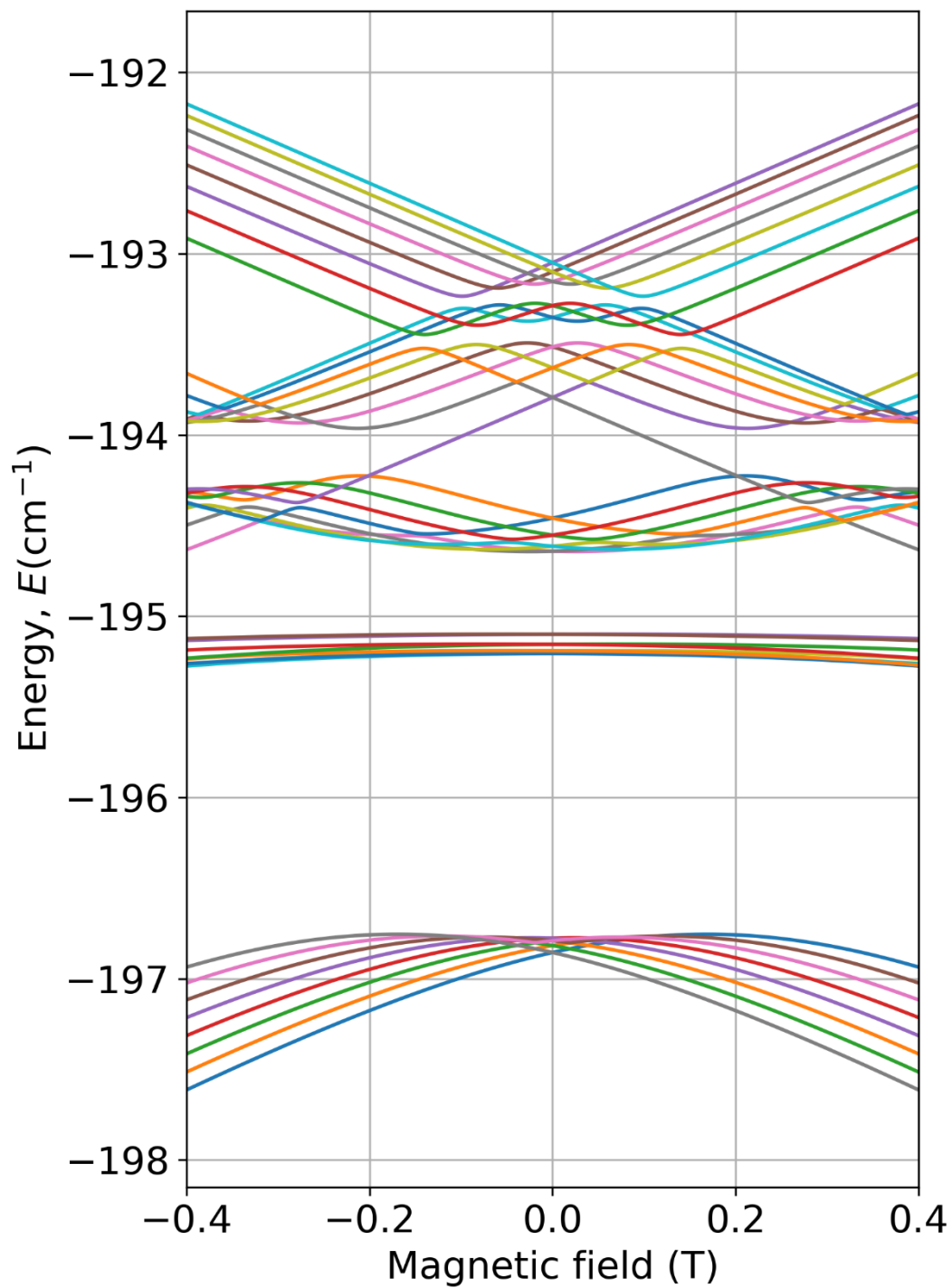


Figure S37: Energy levels splitting for a vertical compression of 0.588%

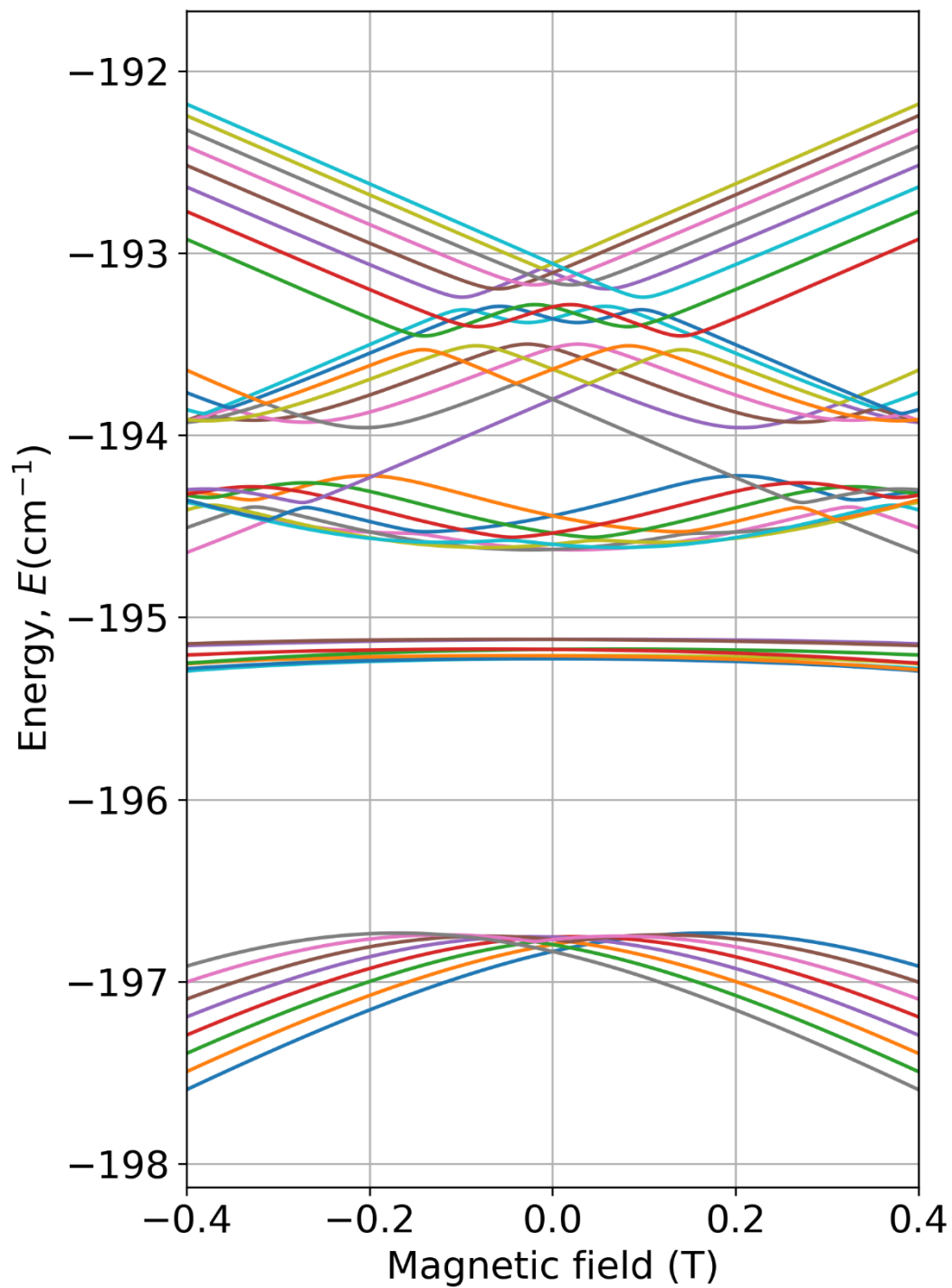


Figure S38: Energy levels splitting for a vertical compression of 0.573%

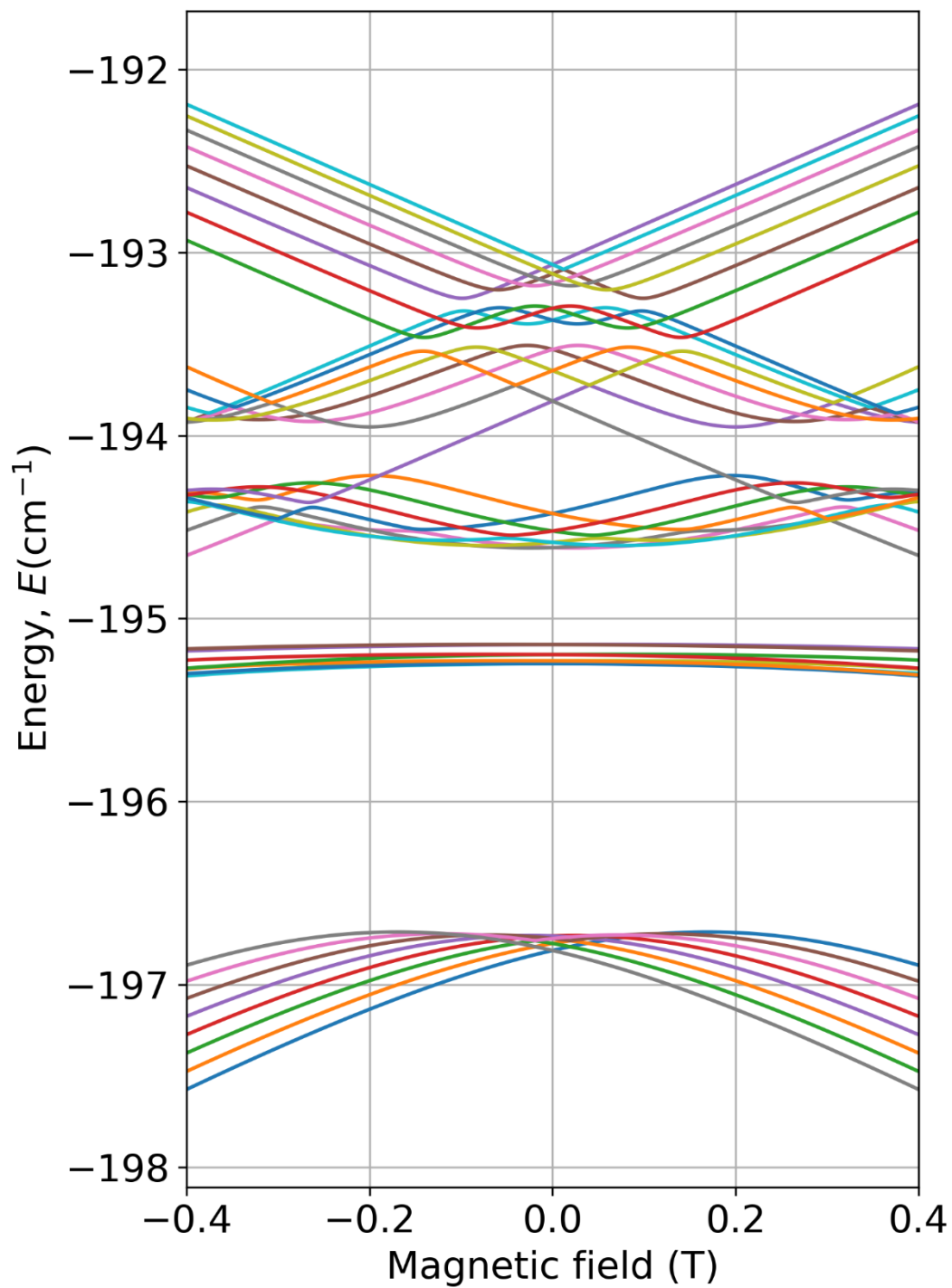


Figure S39: Energy levels splitting for a vertical compression of 0.559%

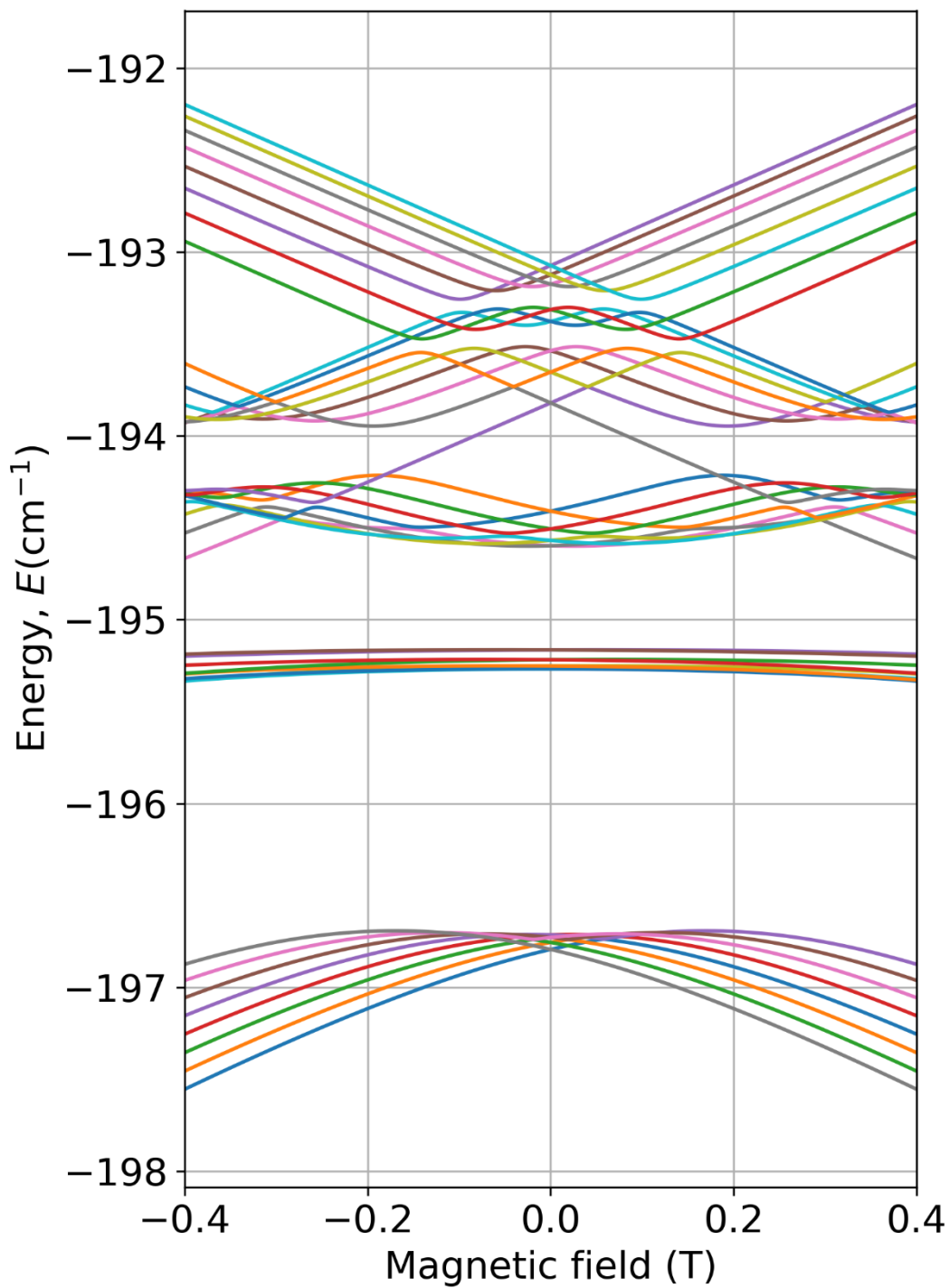


Figure S40: Energy levels splitting for a vertical compression of 0.544%

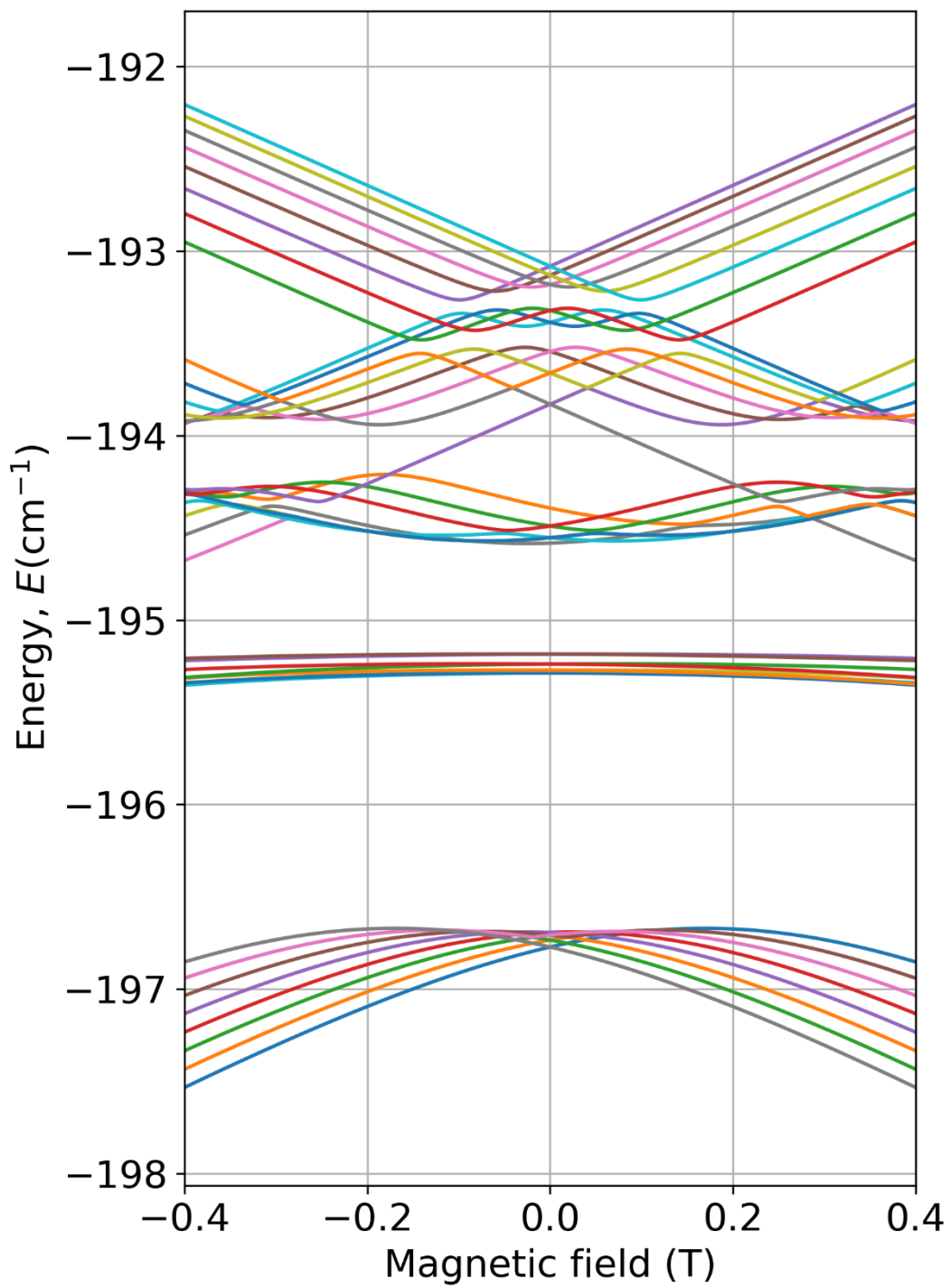


Figure S41: Energy levels splitting for a vertical compression of 0.529%

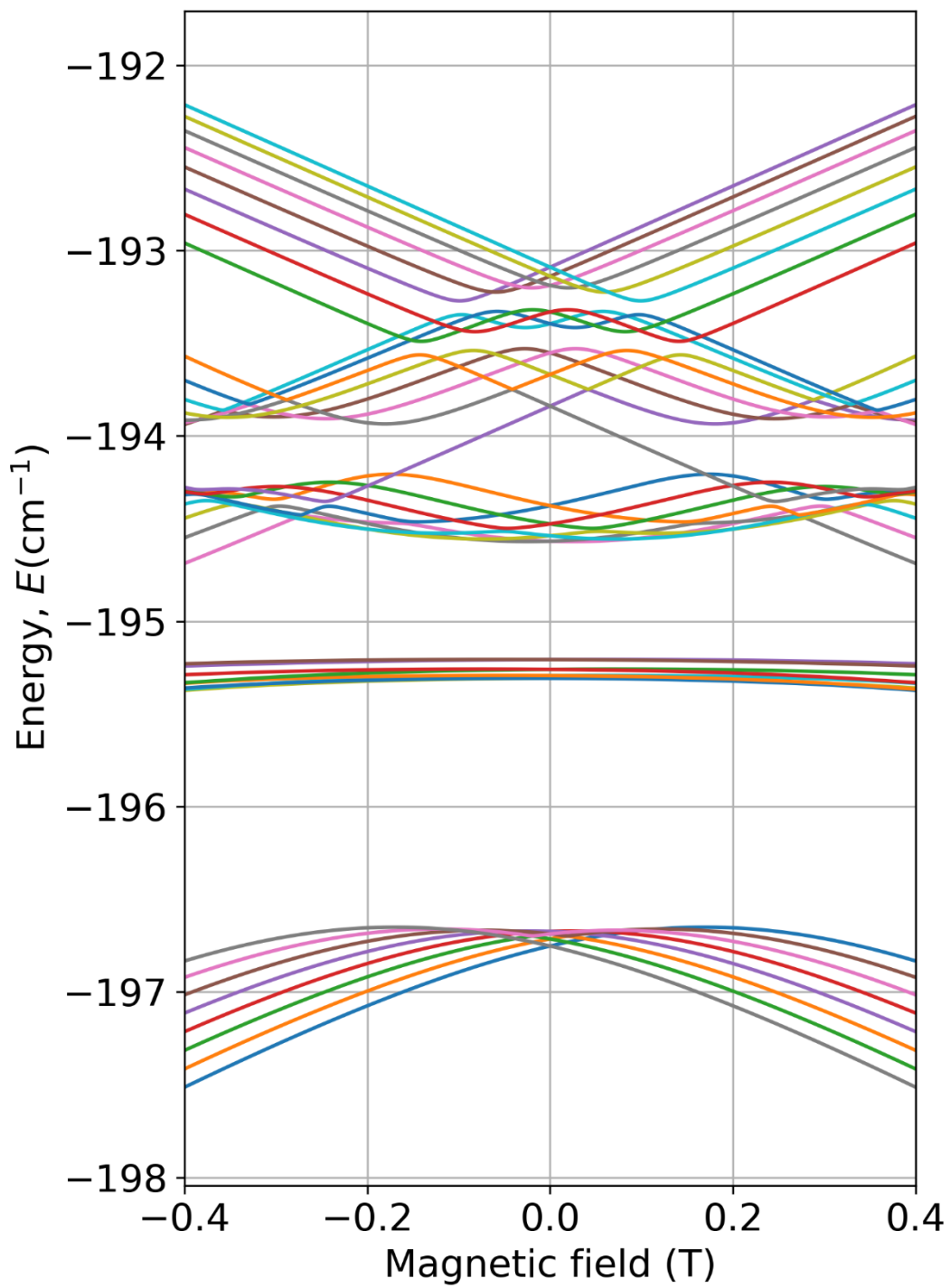


Figure S42: Energy levels splitting for a vertical compression of 0.514%

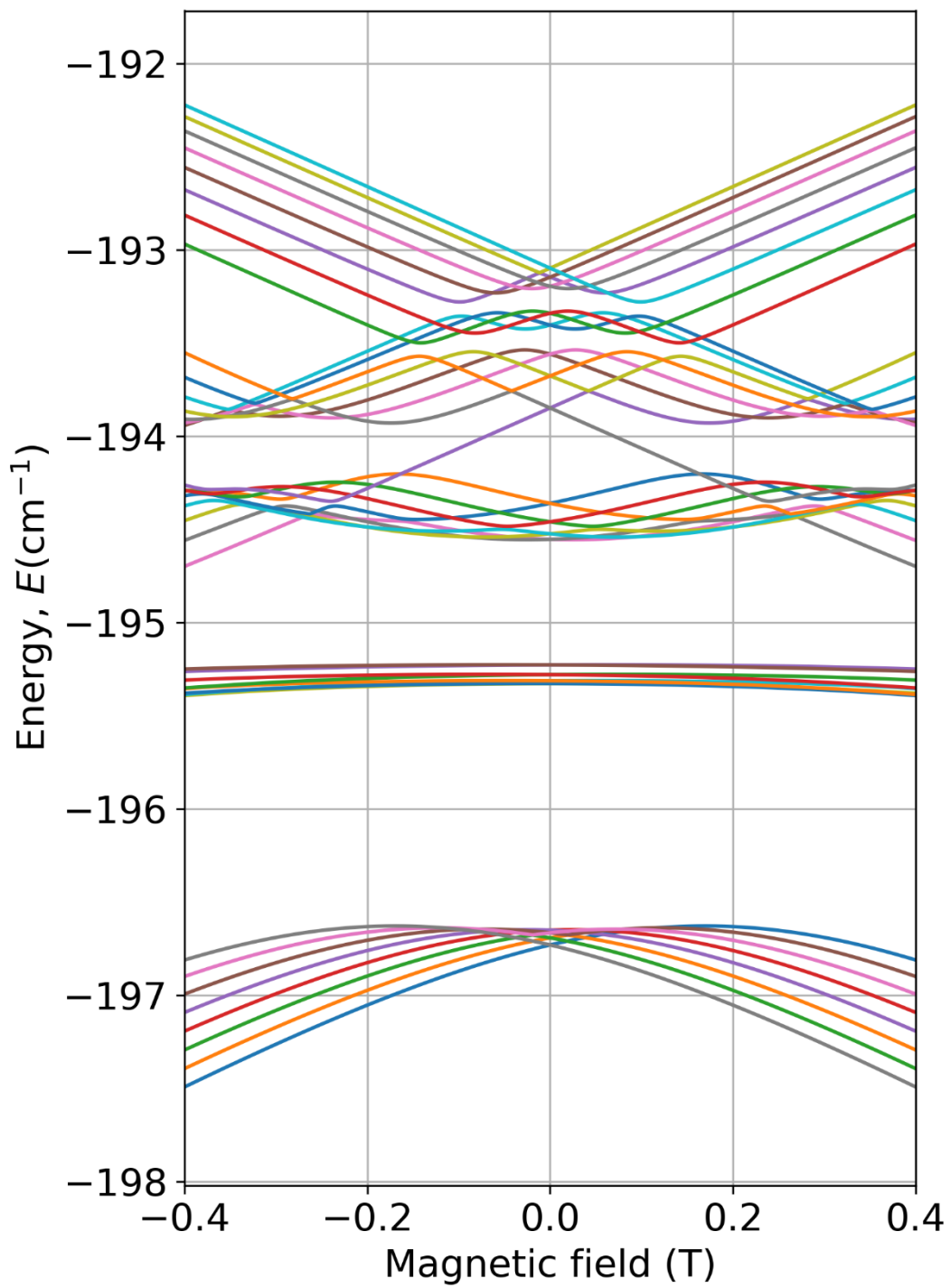


Figure S43: Energy levels splitting for a vertical compression of 0.500%

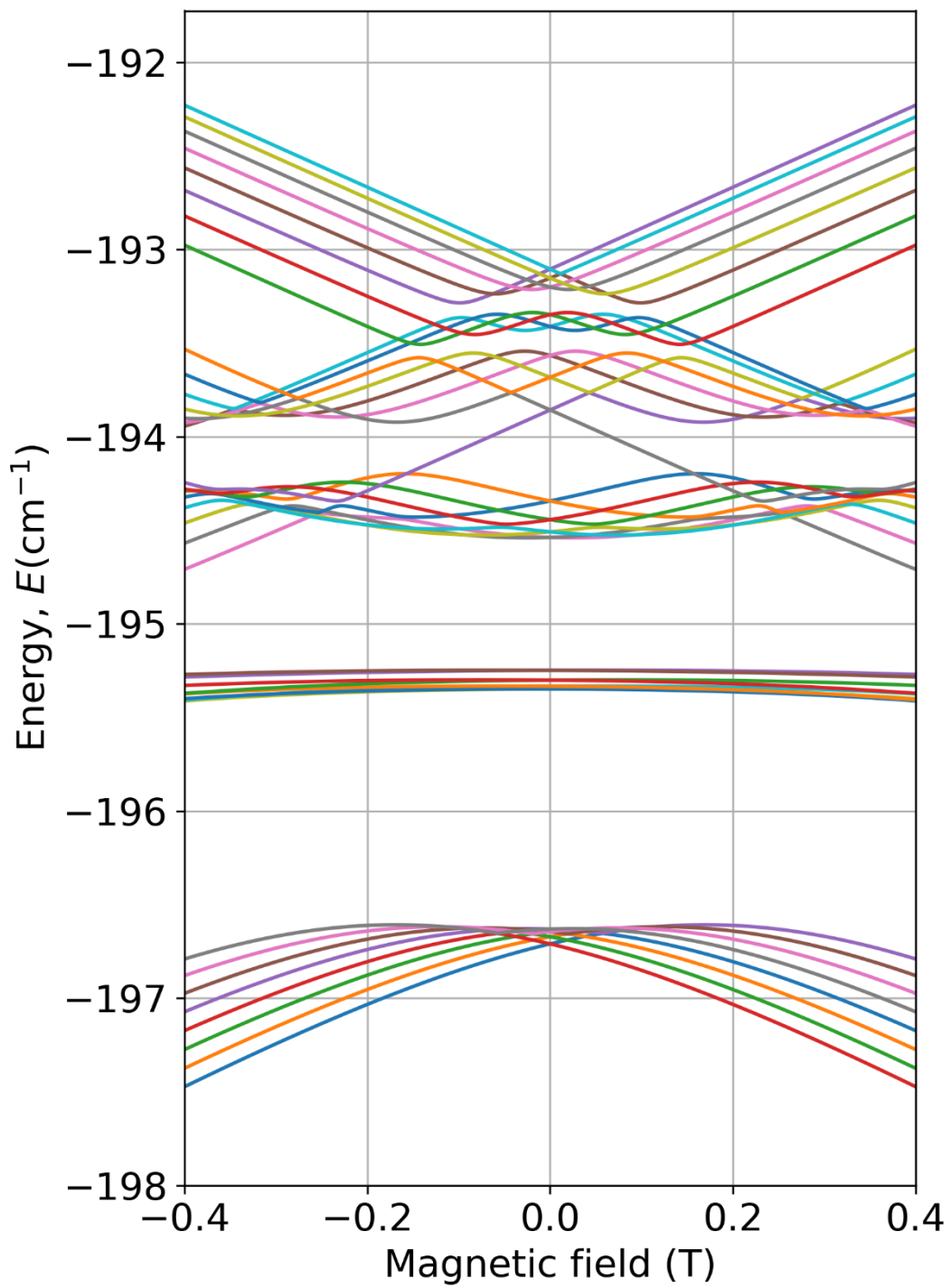


Figure S44: Energy levels splitting for a vertical compression of 0.485%

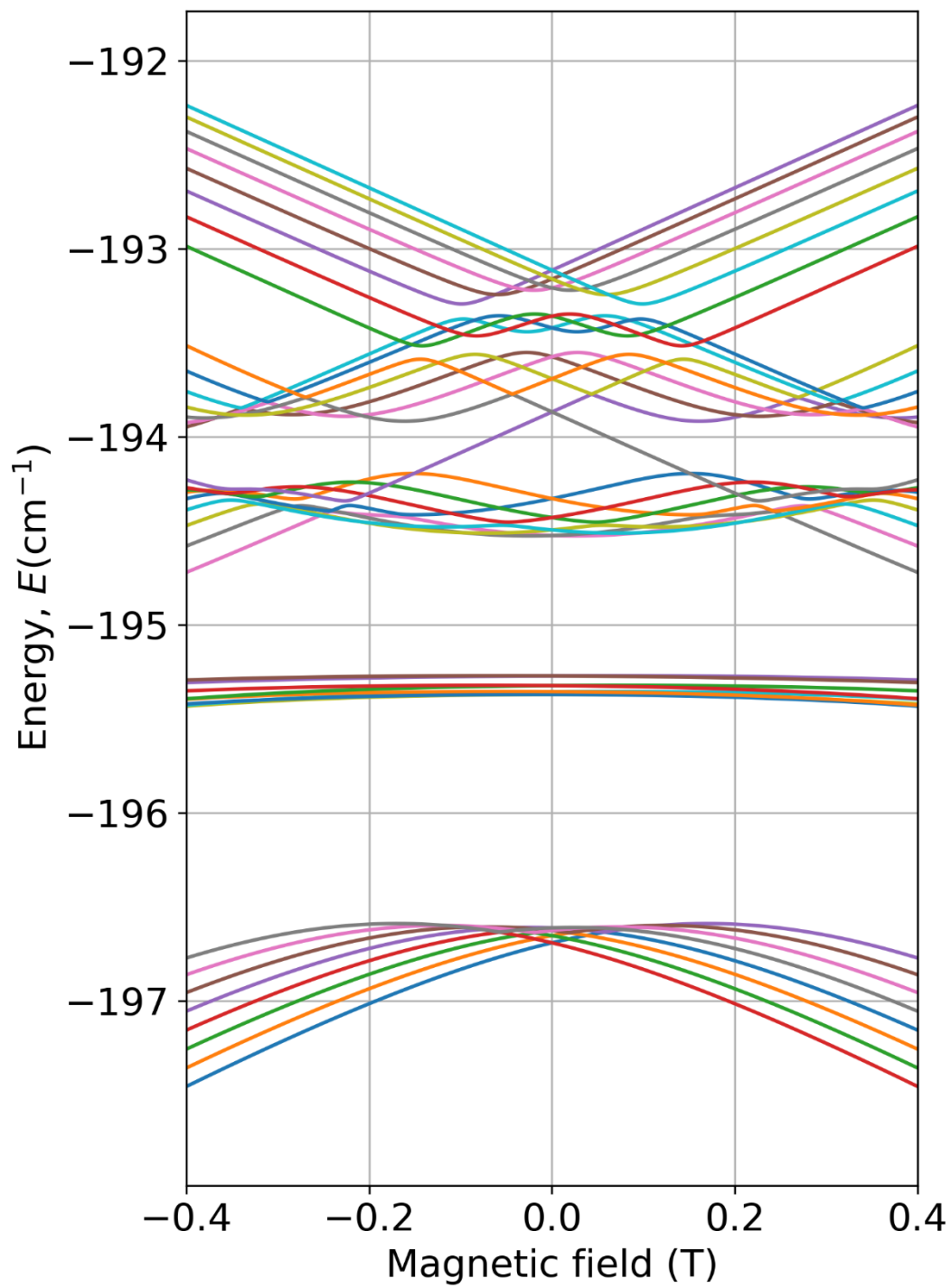


Figure S45: Energy levels splitting for a vertical compression of 0.470%

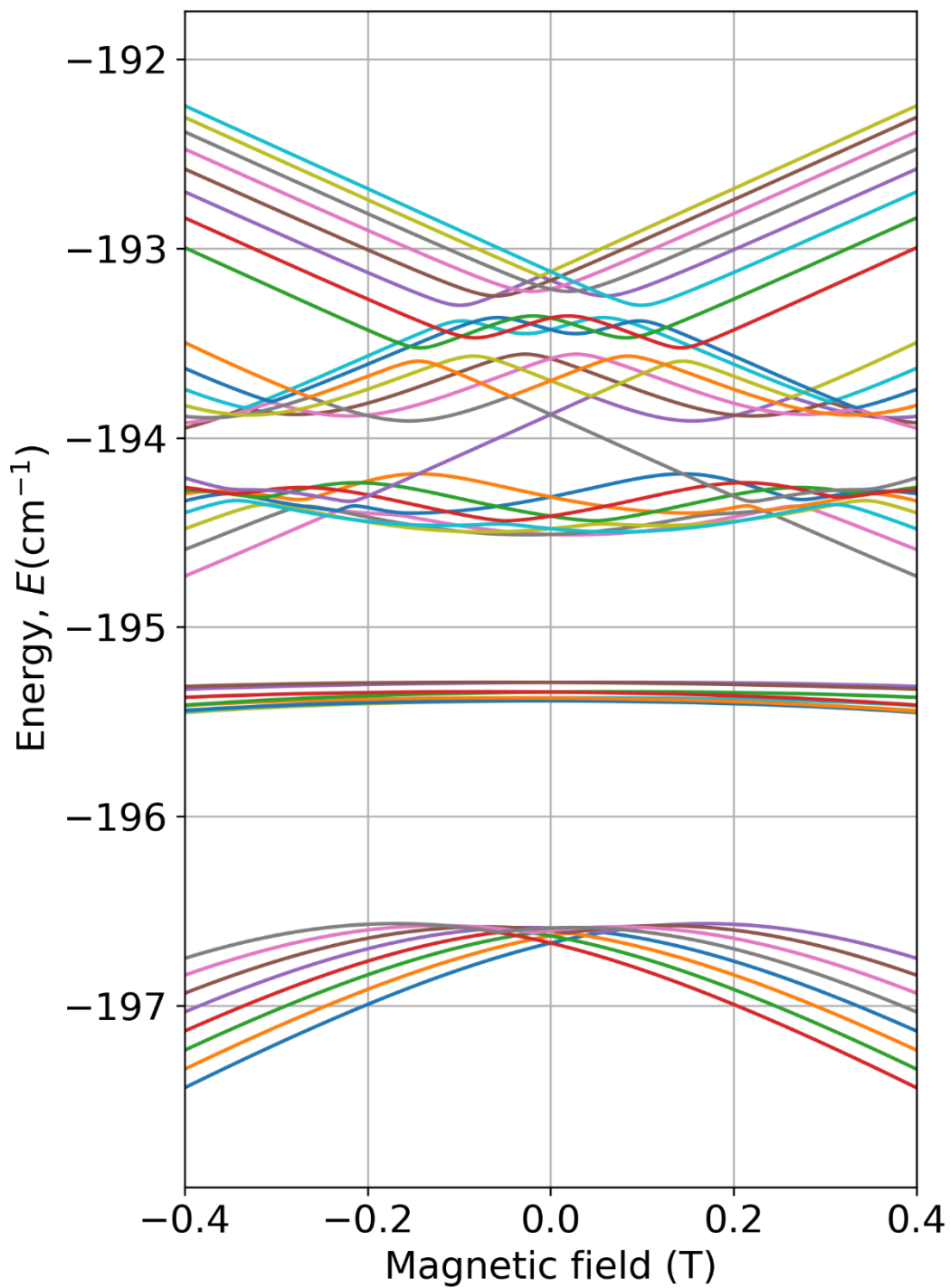


Figure S46: Energy levels splitting for a vertical compression of 0.455%

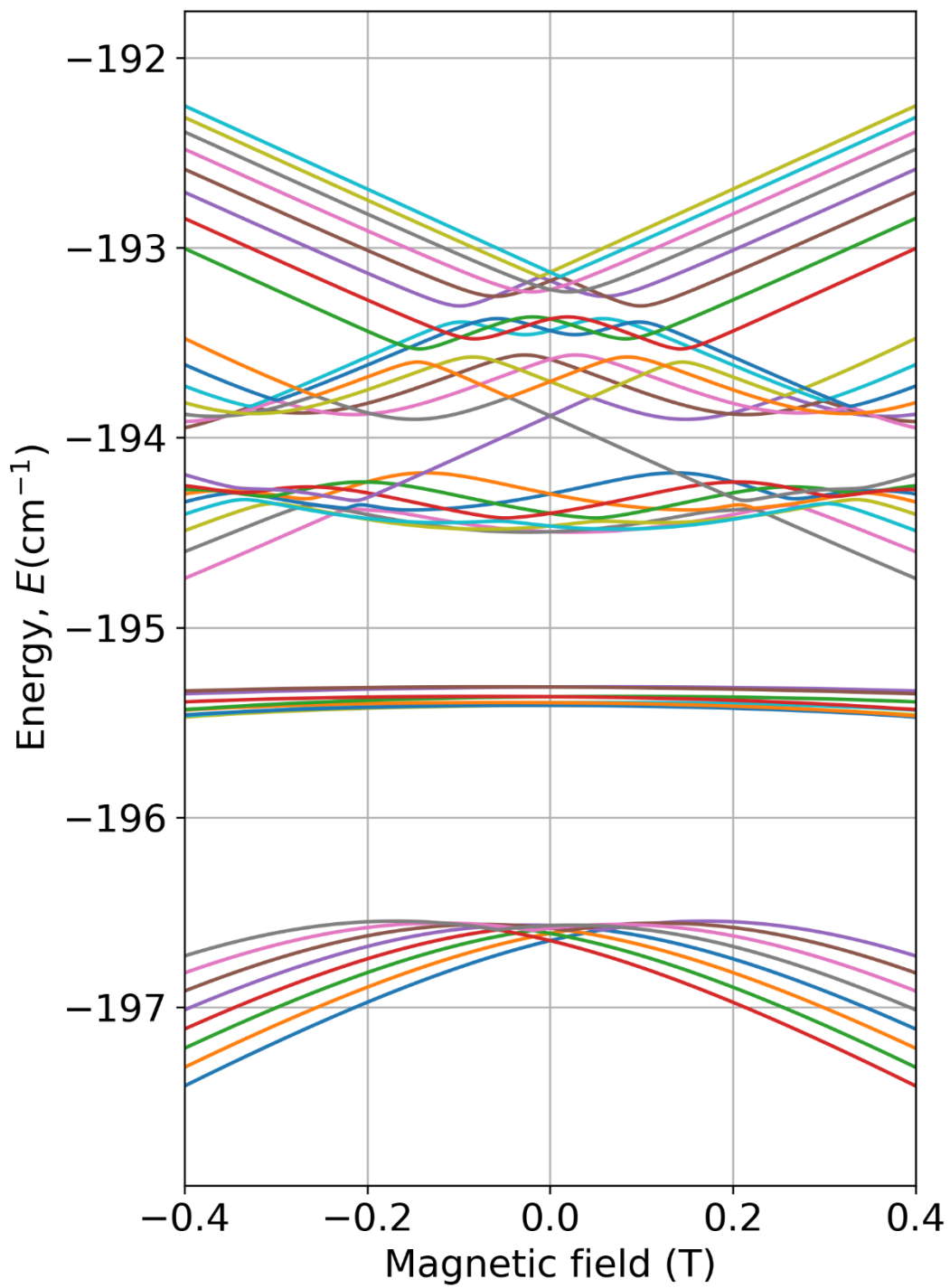


Figure S47: Energy levels splitting for a vertical compression of 0.441%

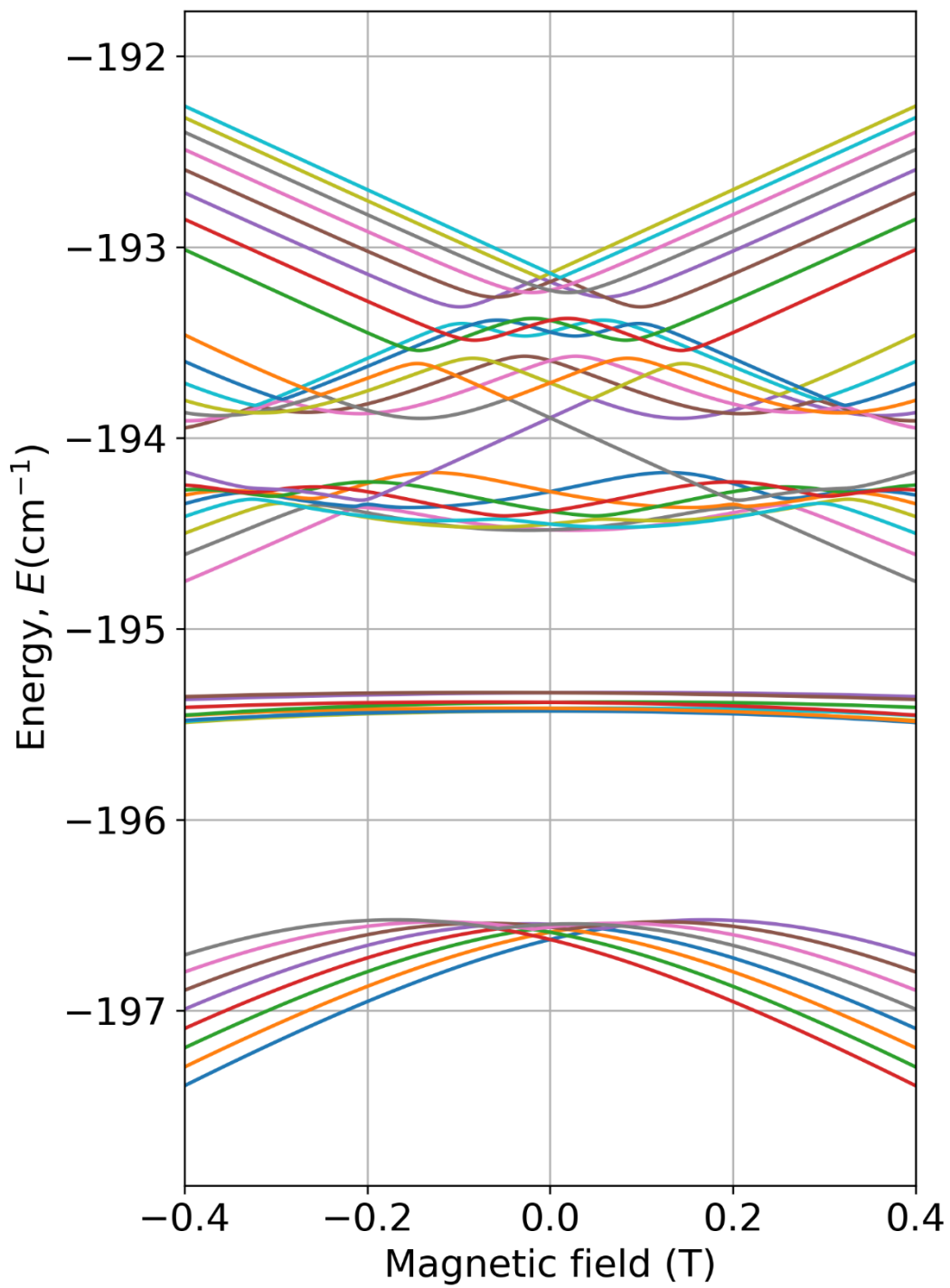


Figure S48: Energy levels splitting for a vertical compression of 0.426%

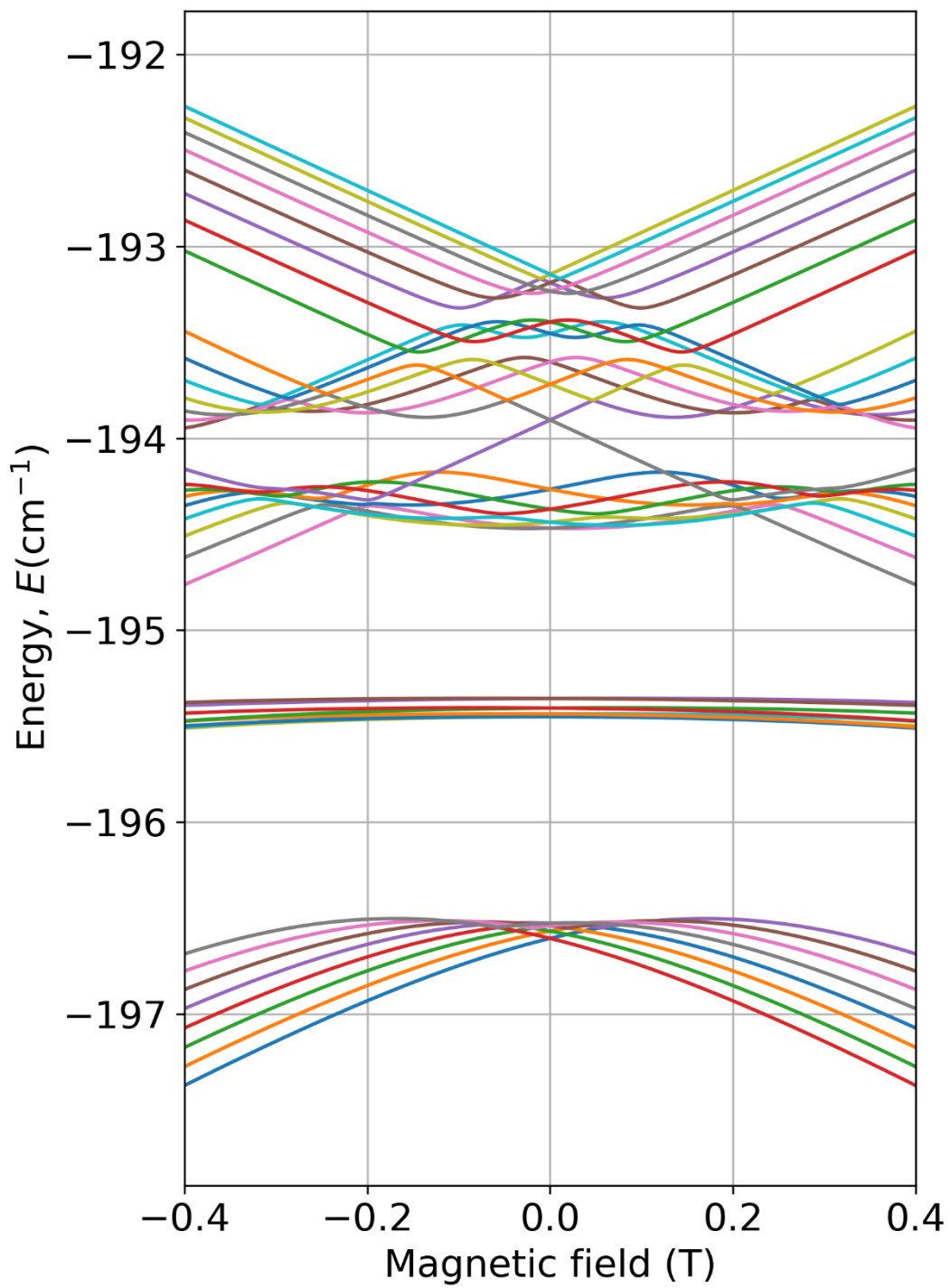


Figure S49: Energy levels splitting for a vertical compression of 0.411%

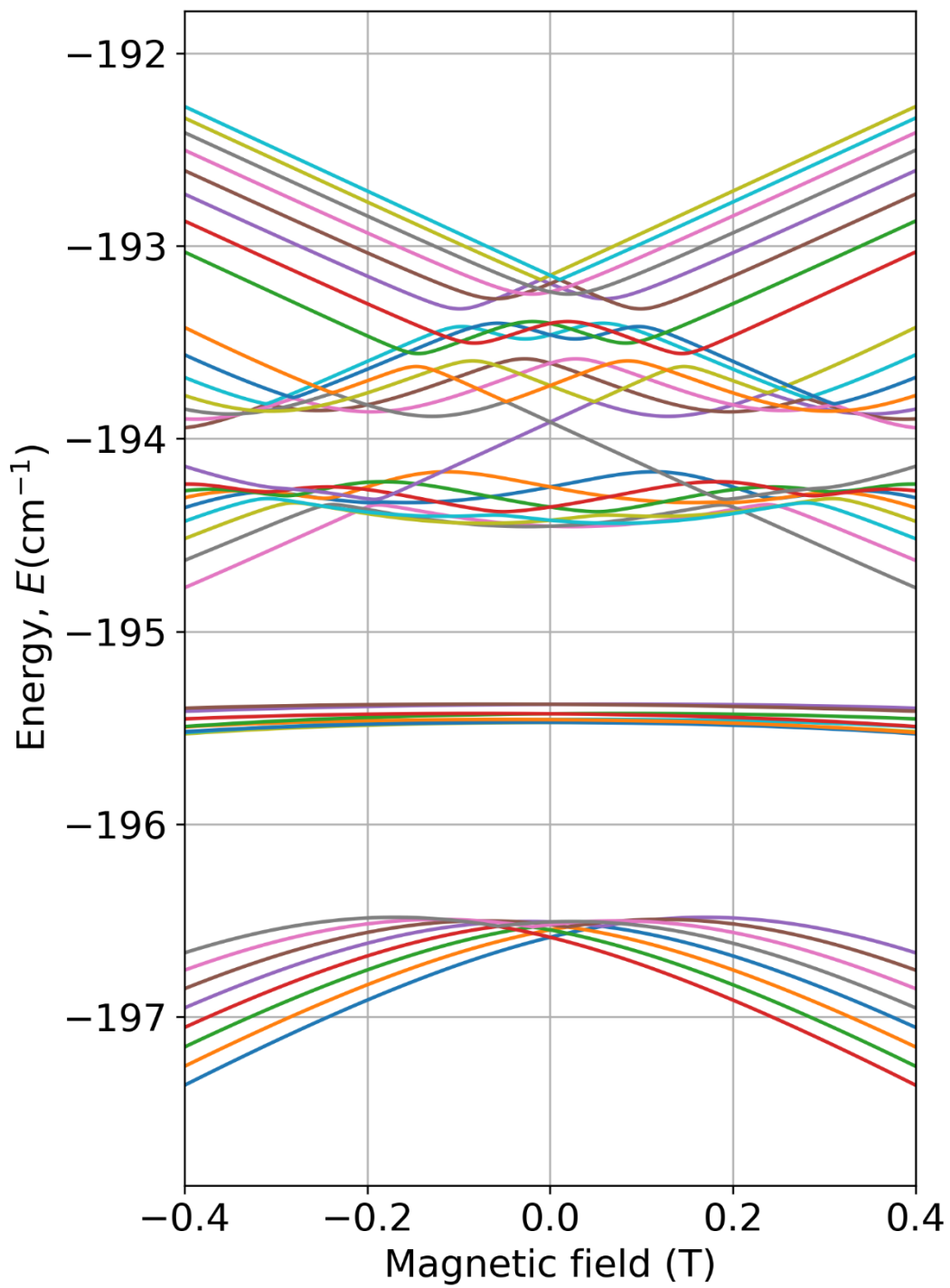


Figure S50: Energy levels splitting for a vertical compression of 0.397%

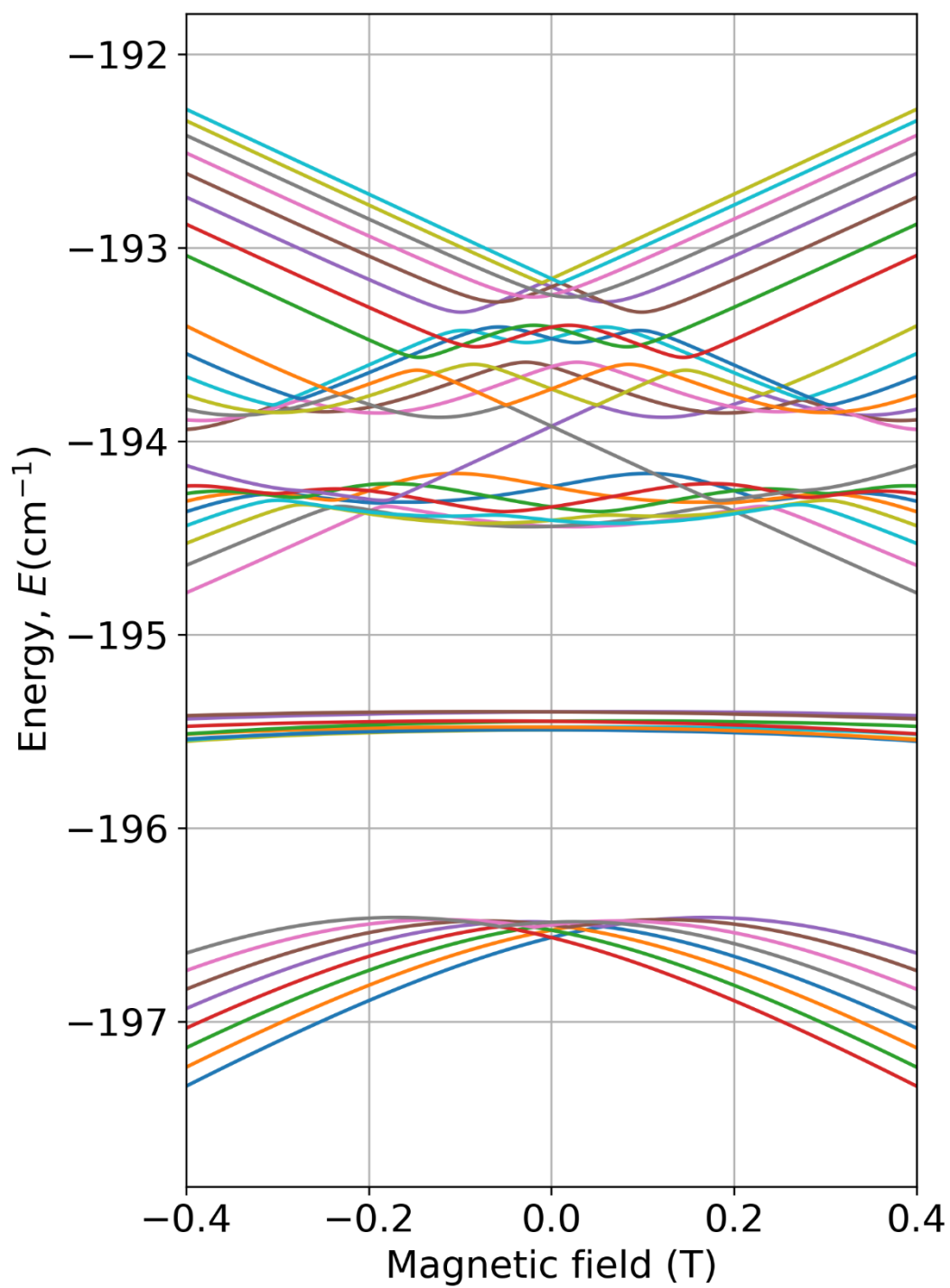


Figure S51: Energy levels splitting for a vertical compression of 0.382%

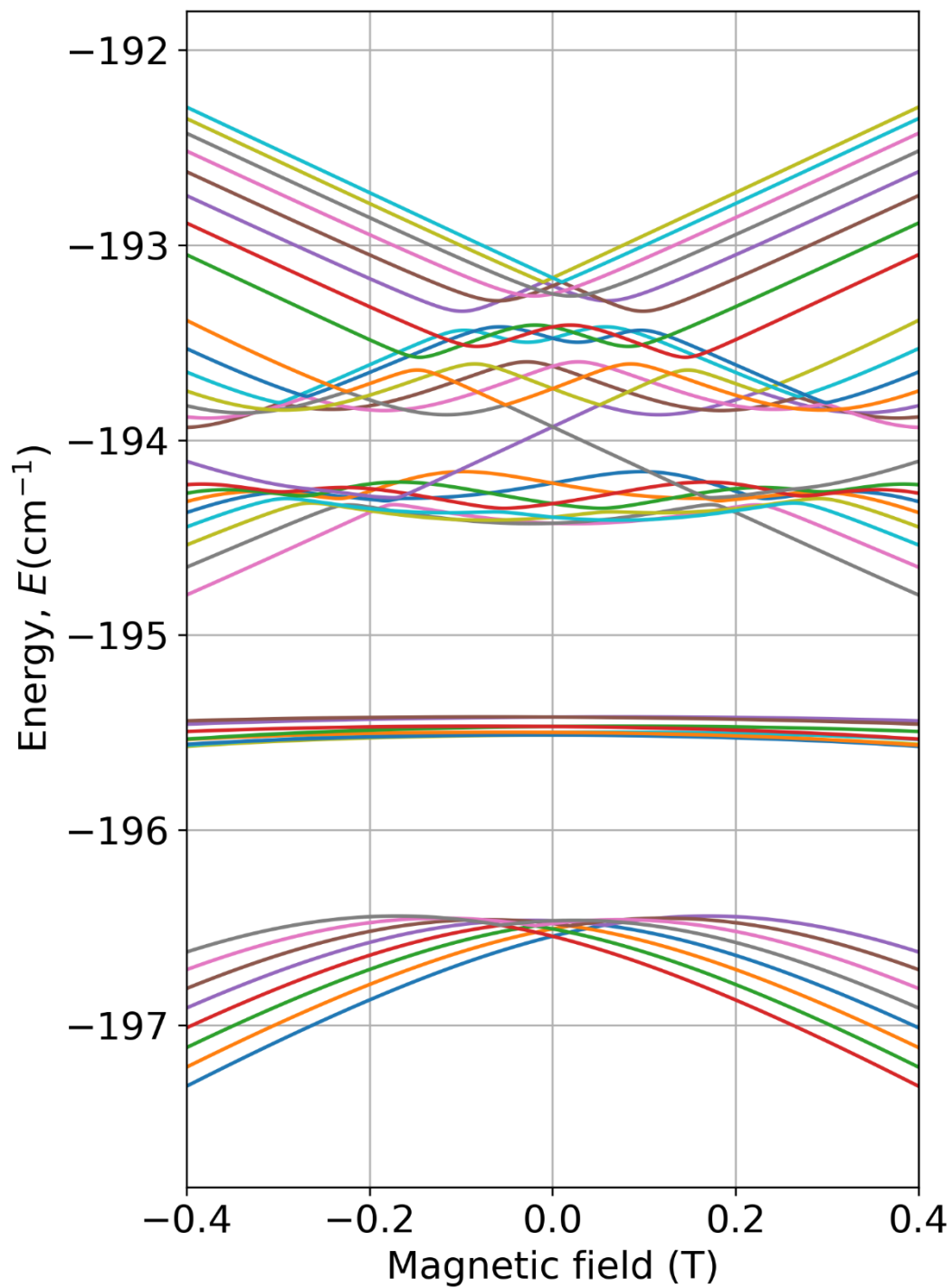


Figure S52: Energy levels splitting for a vertical compression of 0.367%

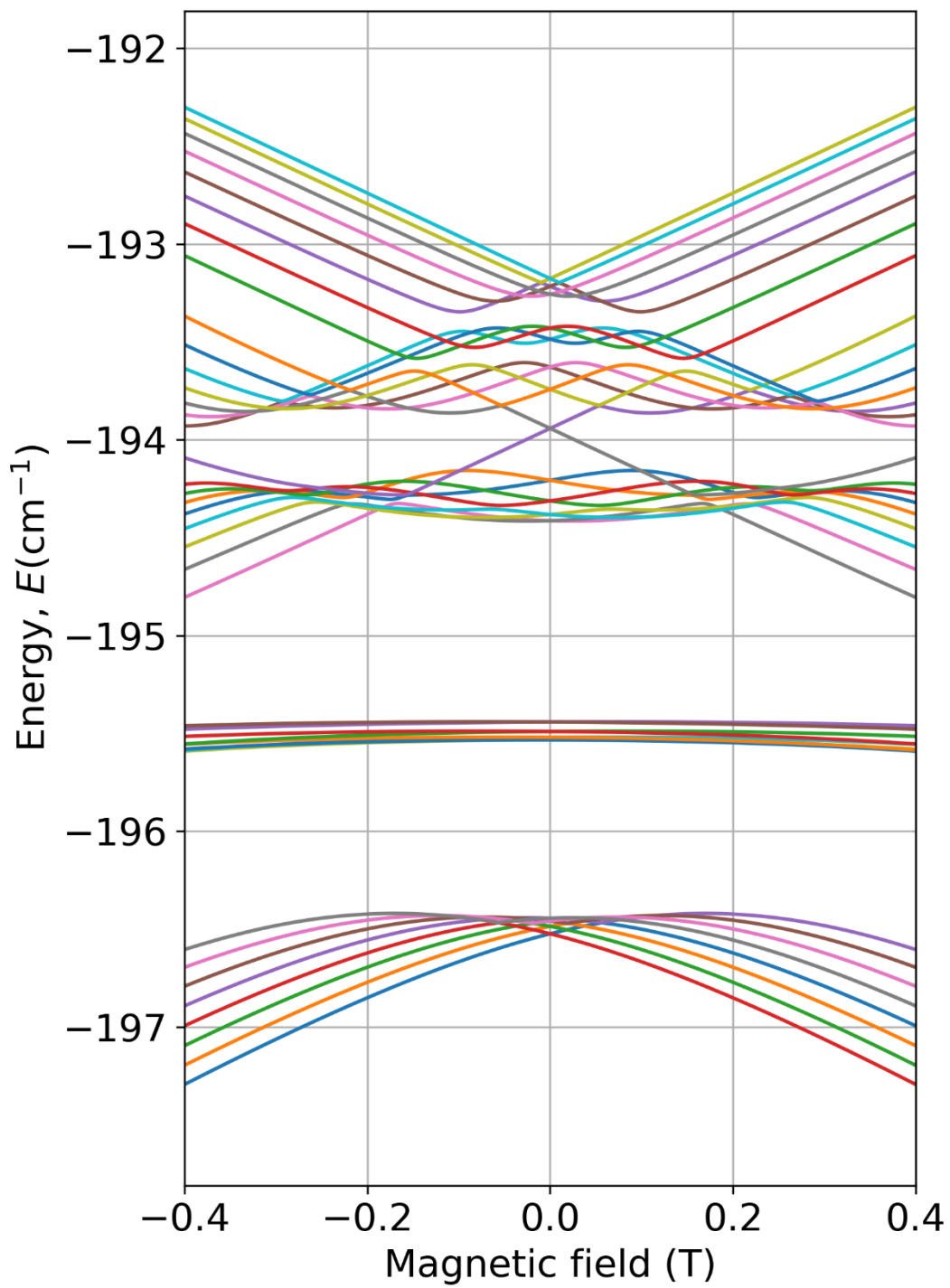


Figure S53: Energy levels splitting for a vertical compression of 0.352%

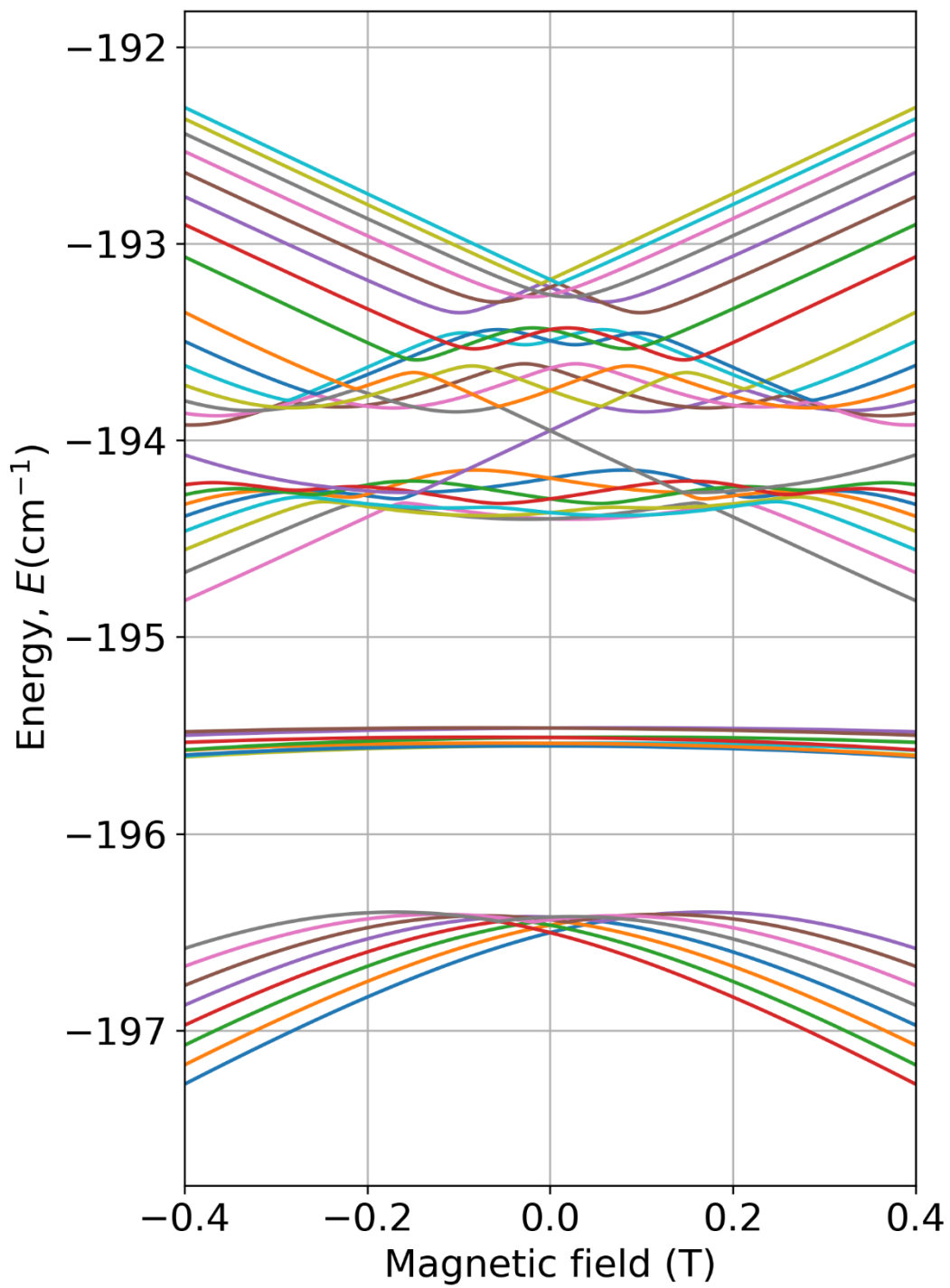


Figure S54: Energy levels splitting for a vertical compression of 0.338%

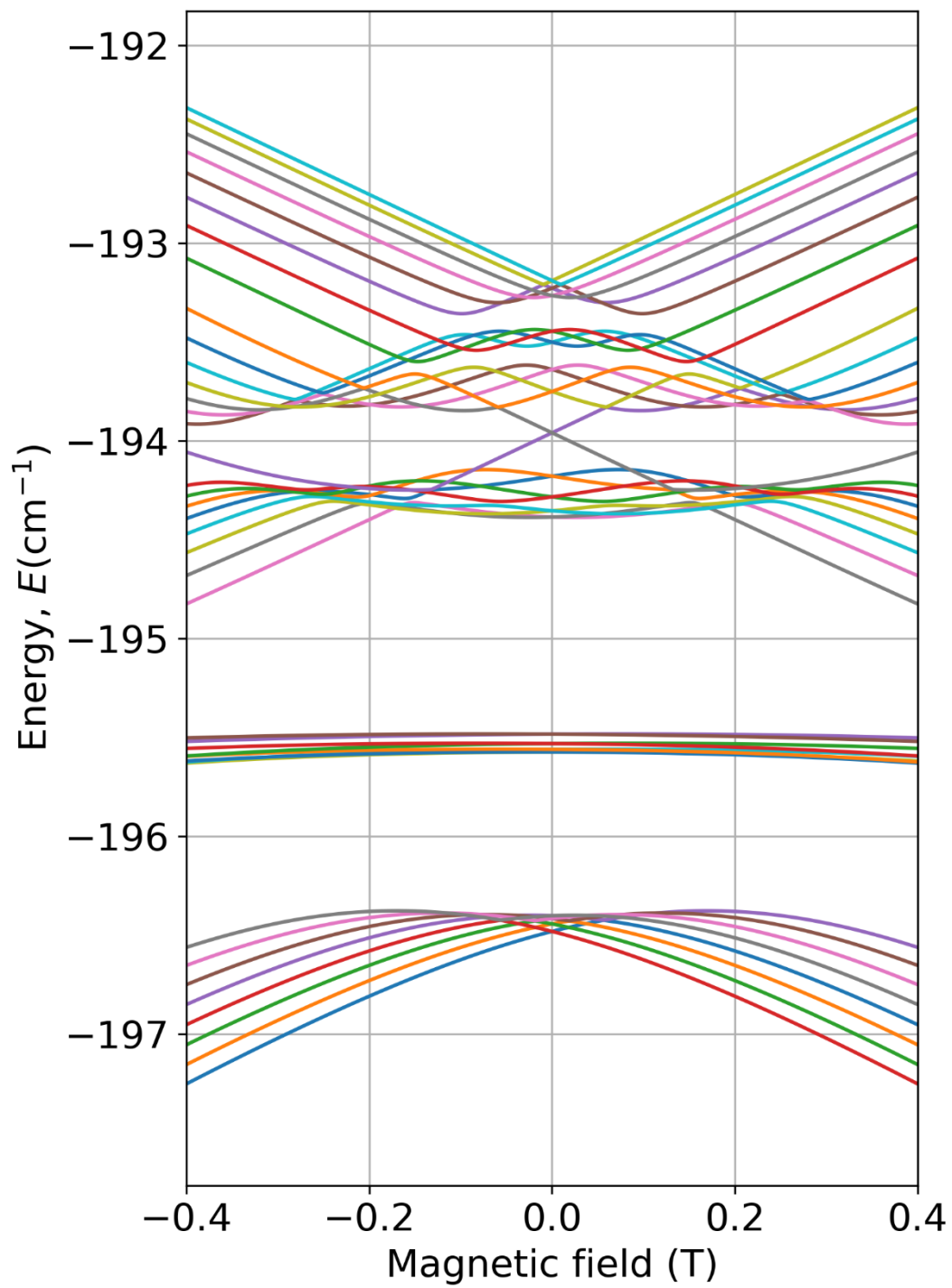


Figure S55: Energy levels splitting for a vertical compression of 0.323%

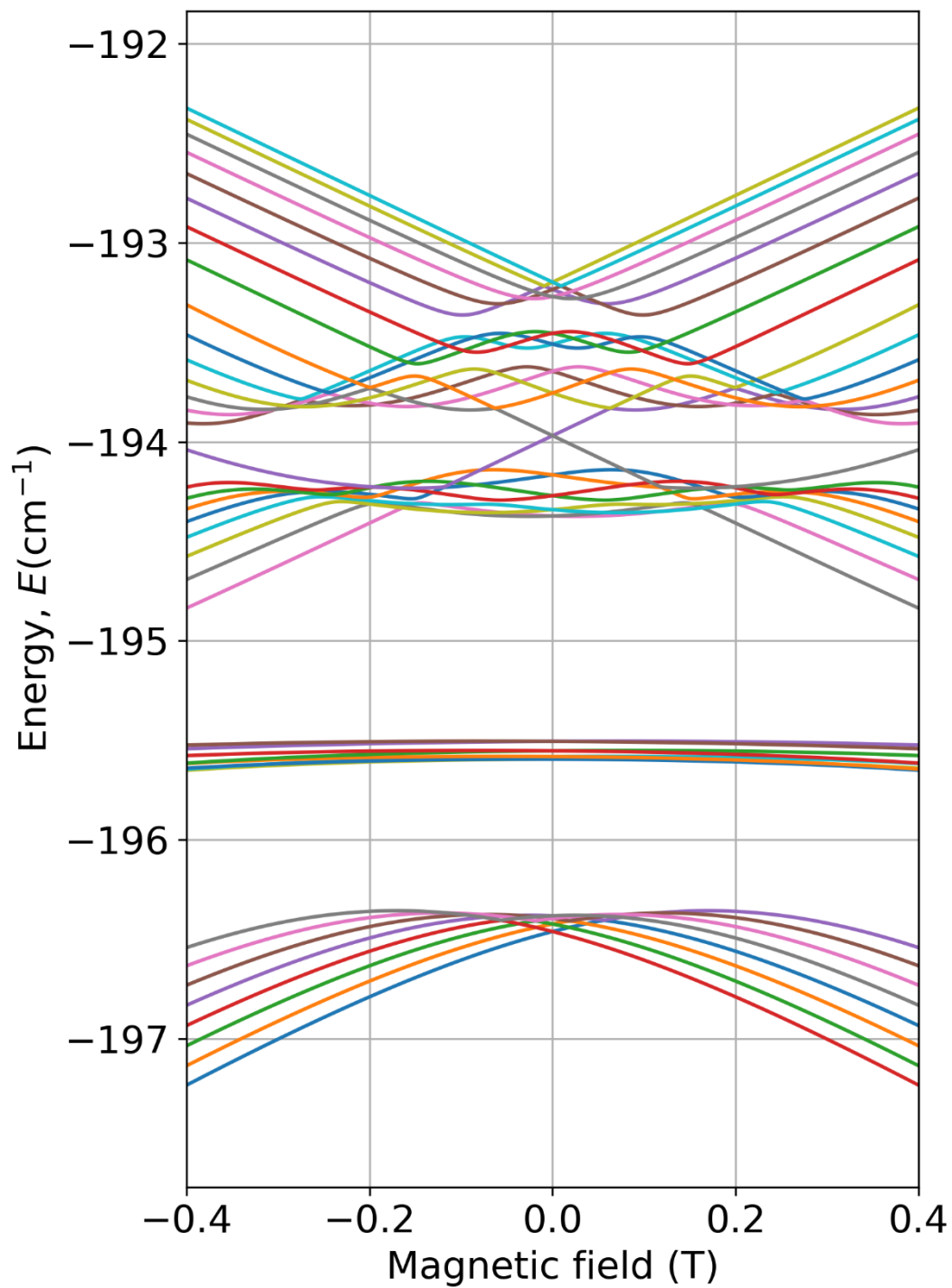


Figure S56: Energy levels splitting for a vertical compression of 0.308%

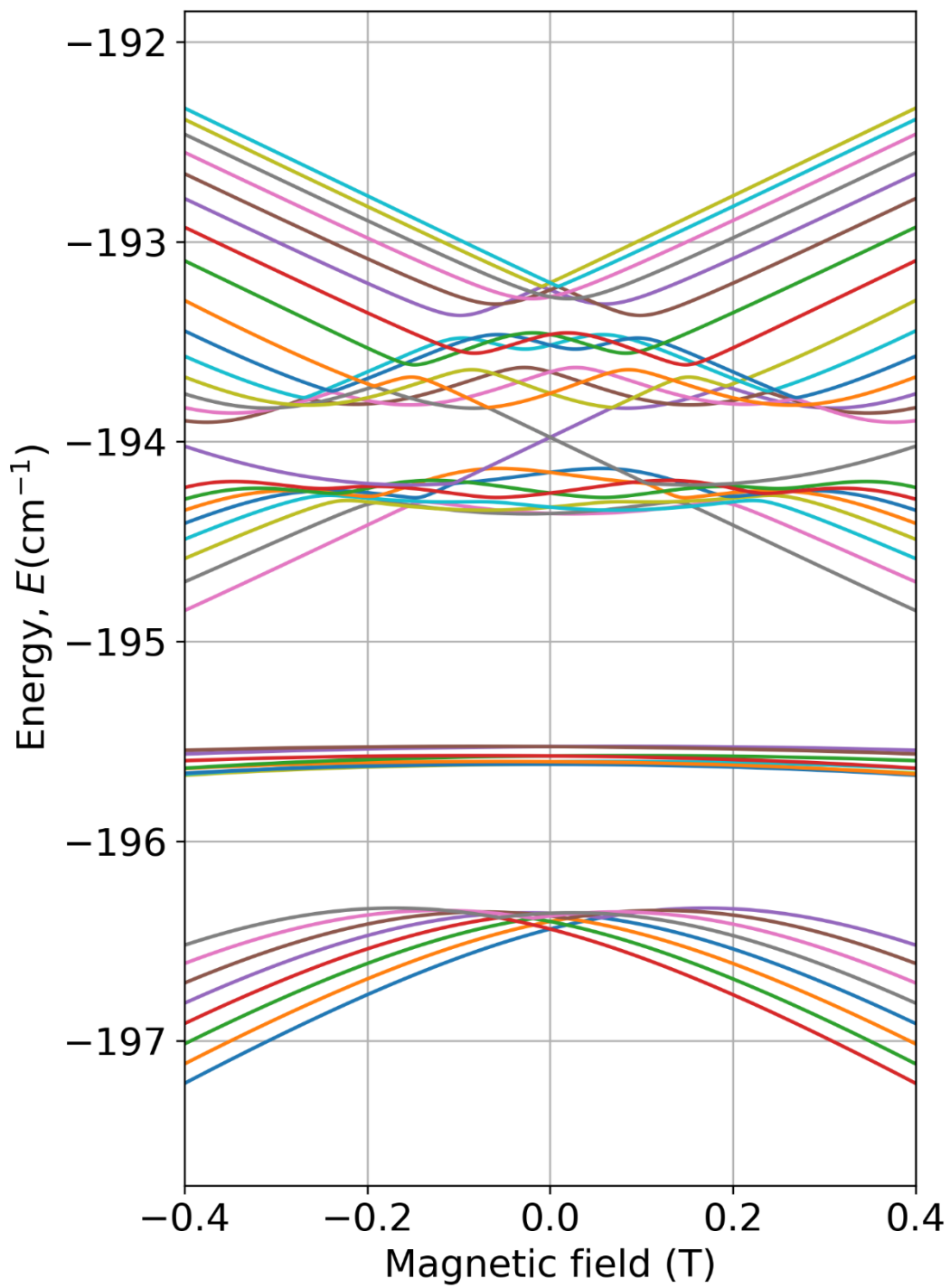


Figure S57: Energy levels splitting for a vertical compression of 0.294%

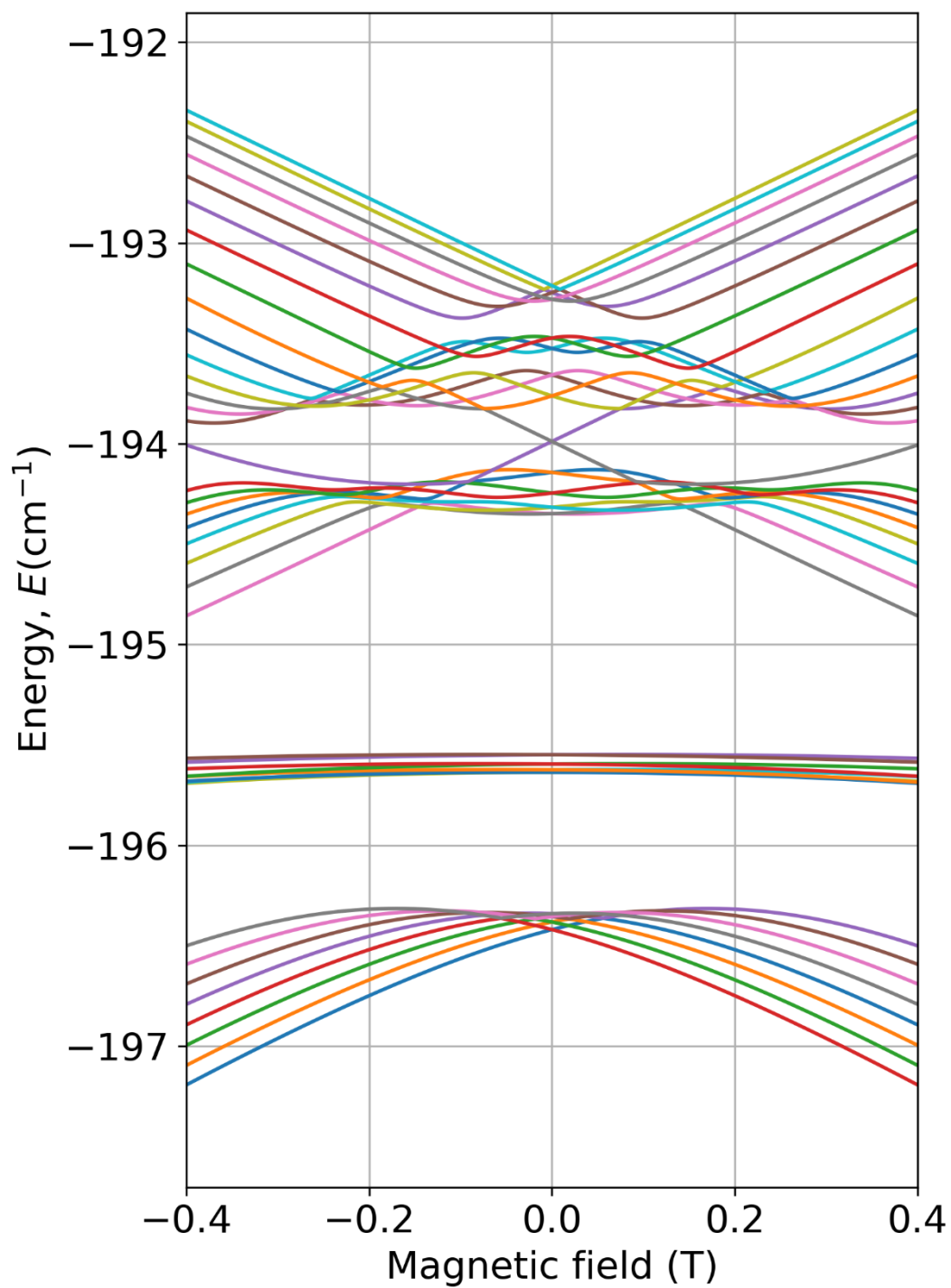


Figure S58: Energy levels splitting for a vertical compression of 0.279%

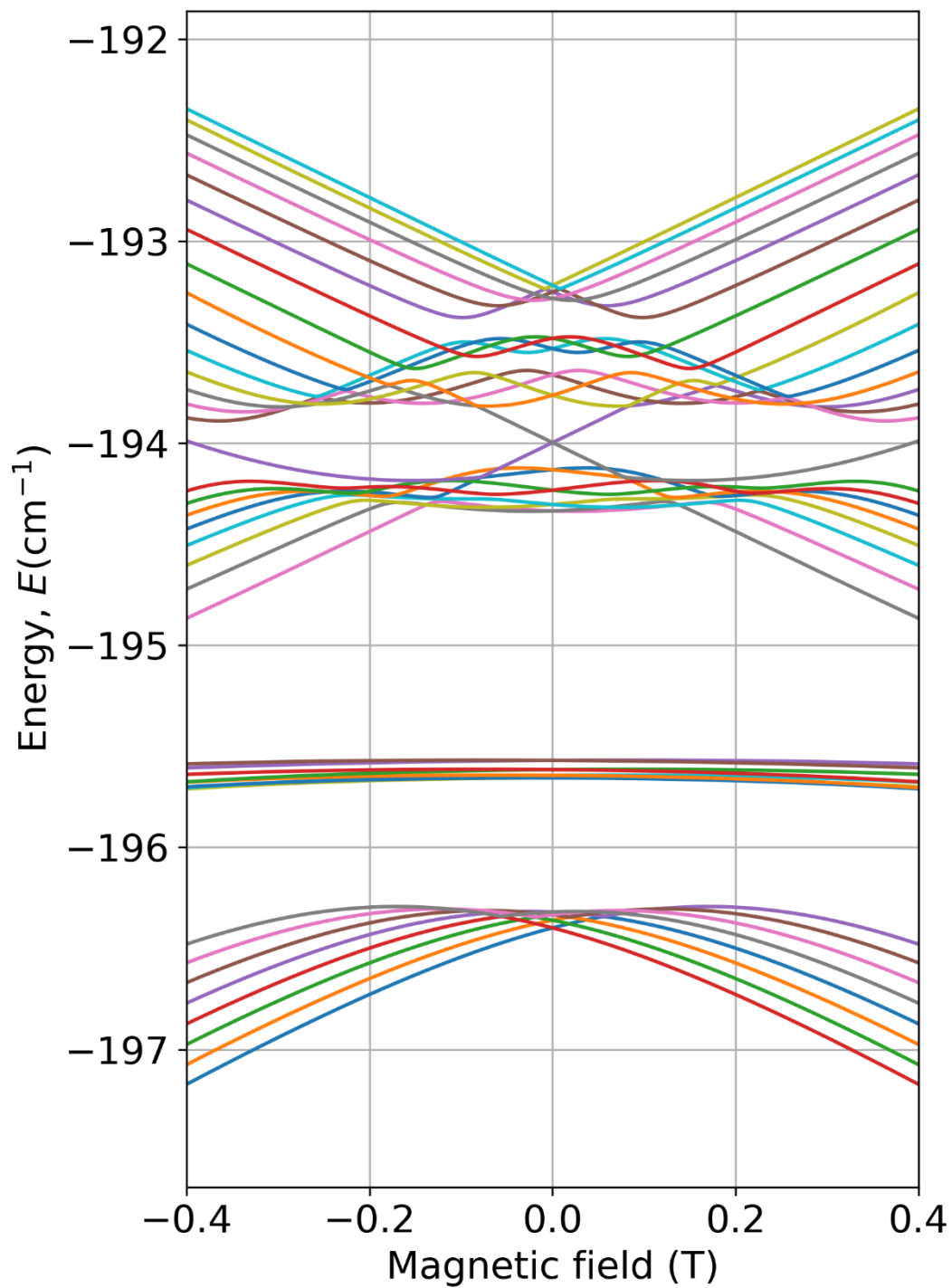


Figure S59: Energy levels splitting for a vertical compression of 0.264%

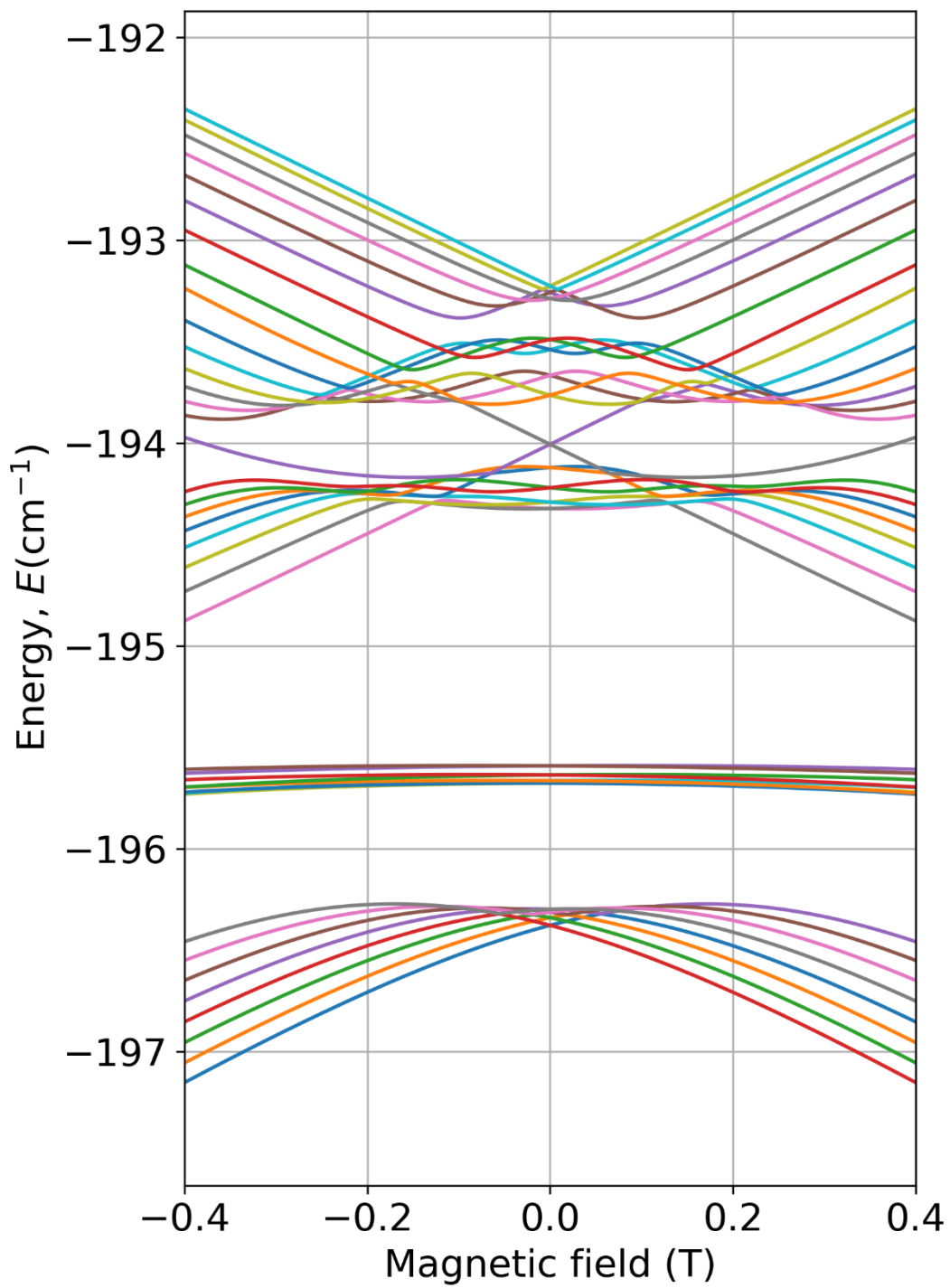


Figure S60: Energy levels splitting for a vertical compression of 0.250%

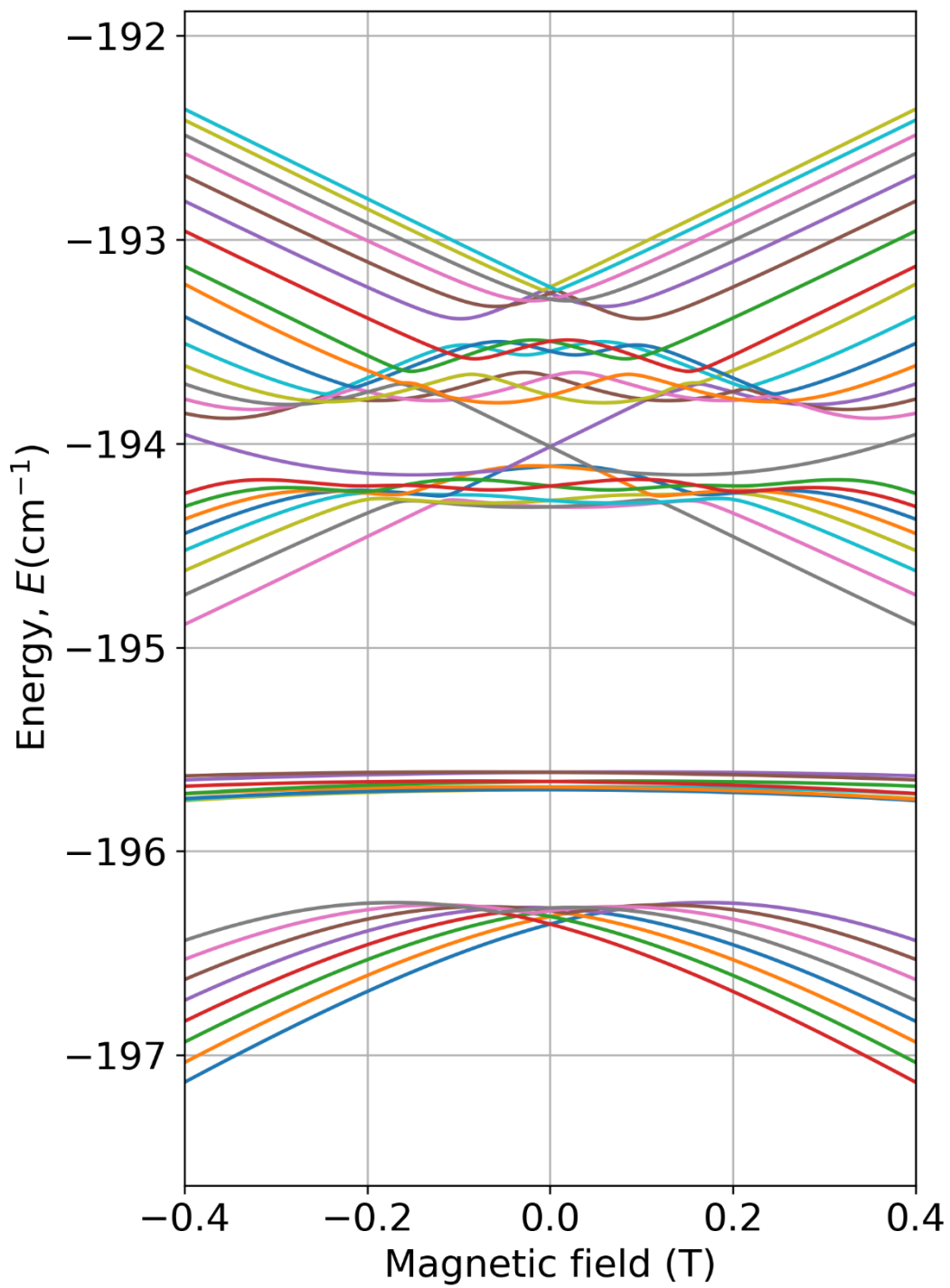


Figure S61: Energy levels splitting for a vertical compression of 0.235%

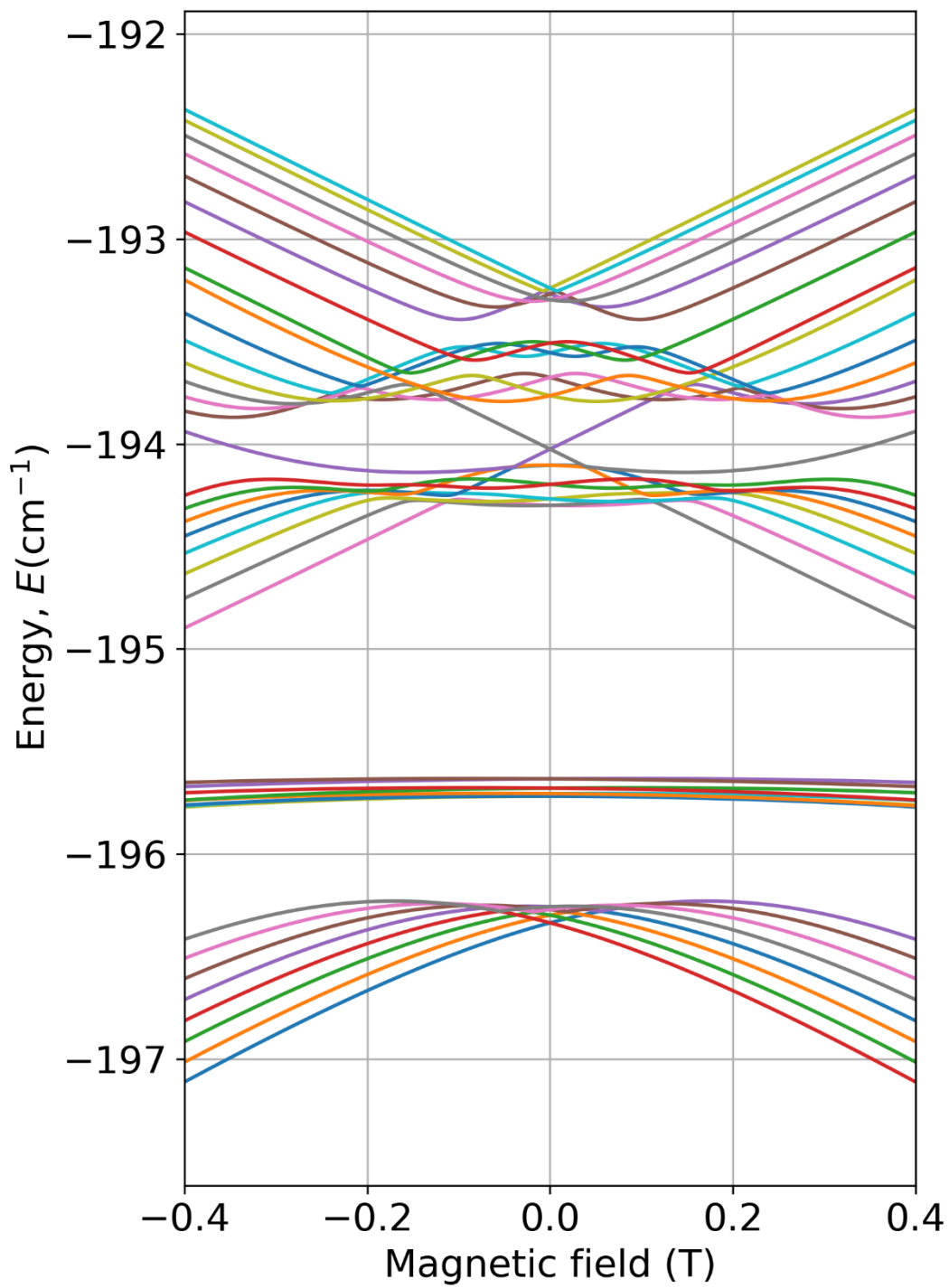


Figure S62: Energy levels splitting for a vertical compression of 0.220%

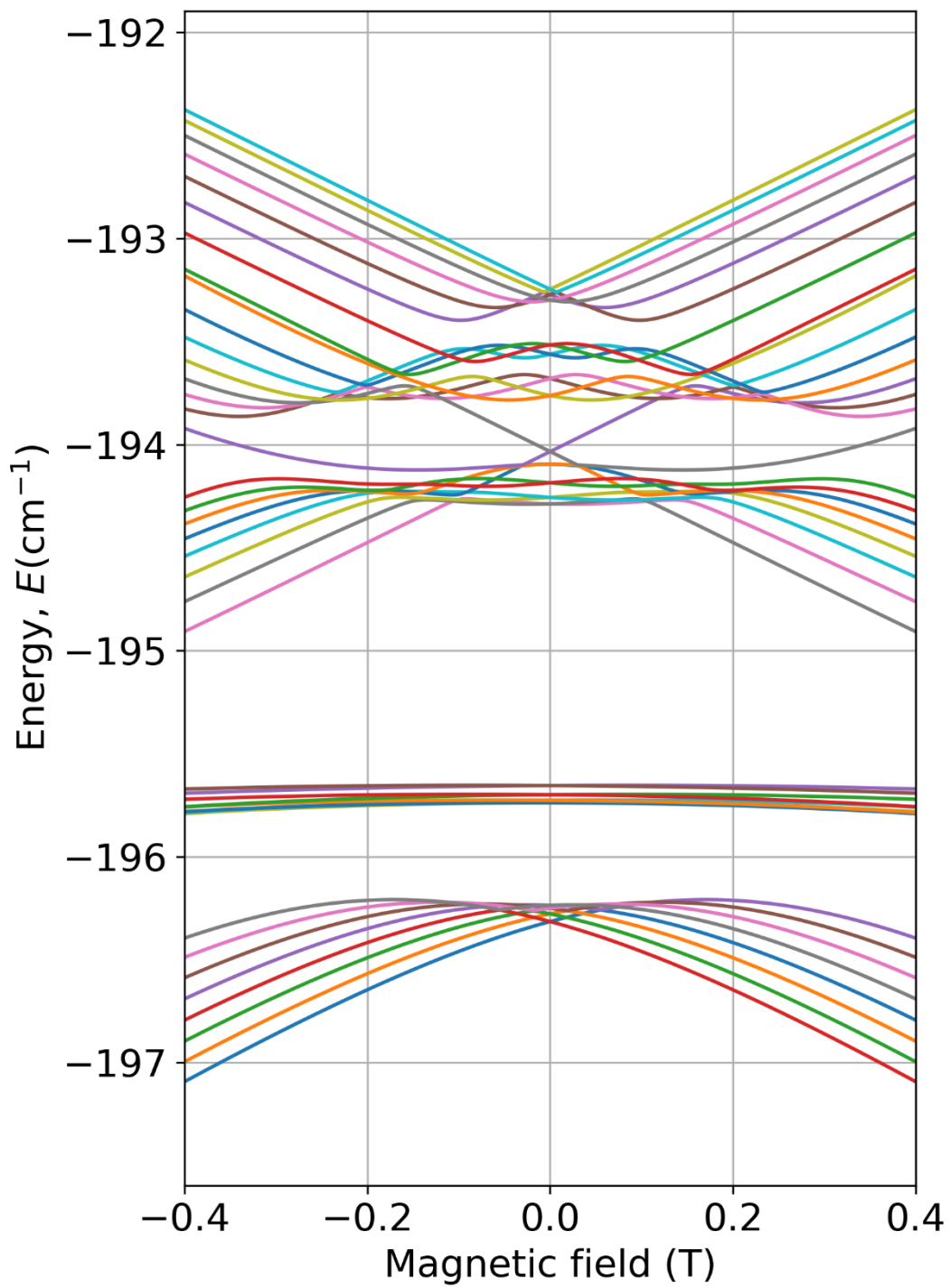


Figure S63: Energy levels splitting for a vertical compression of 0.205%

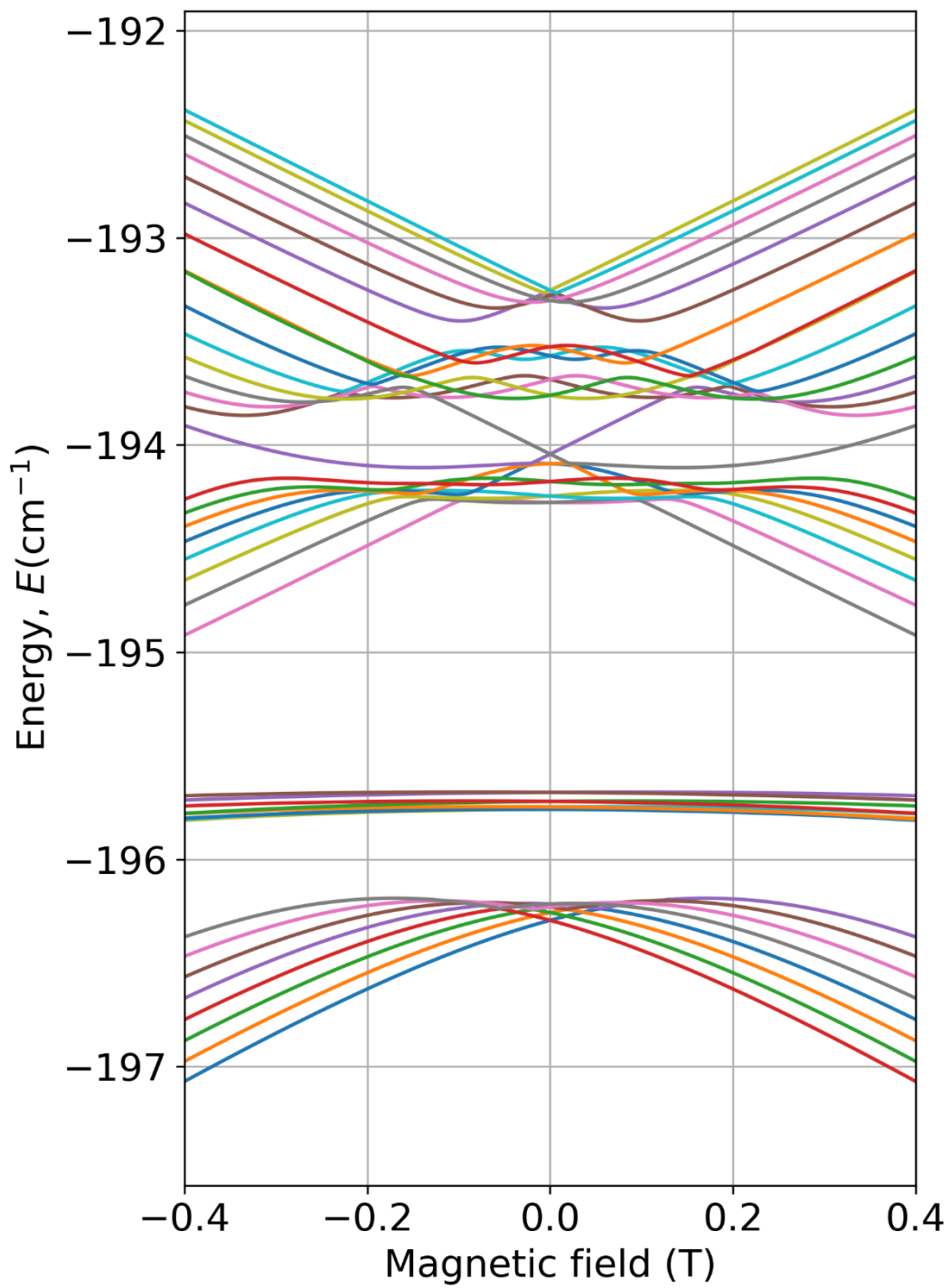


Figure S64: Energy levels splitting for a vertical compression of 0.191%

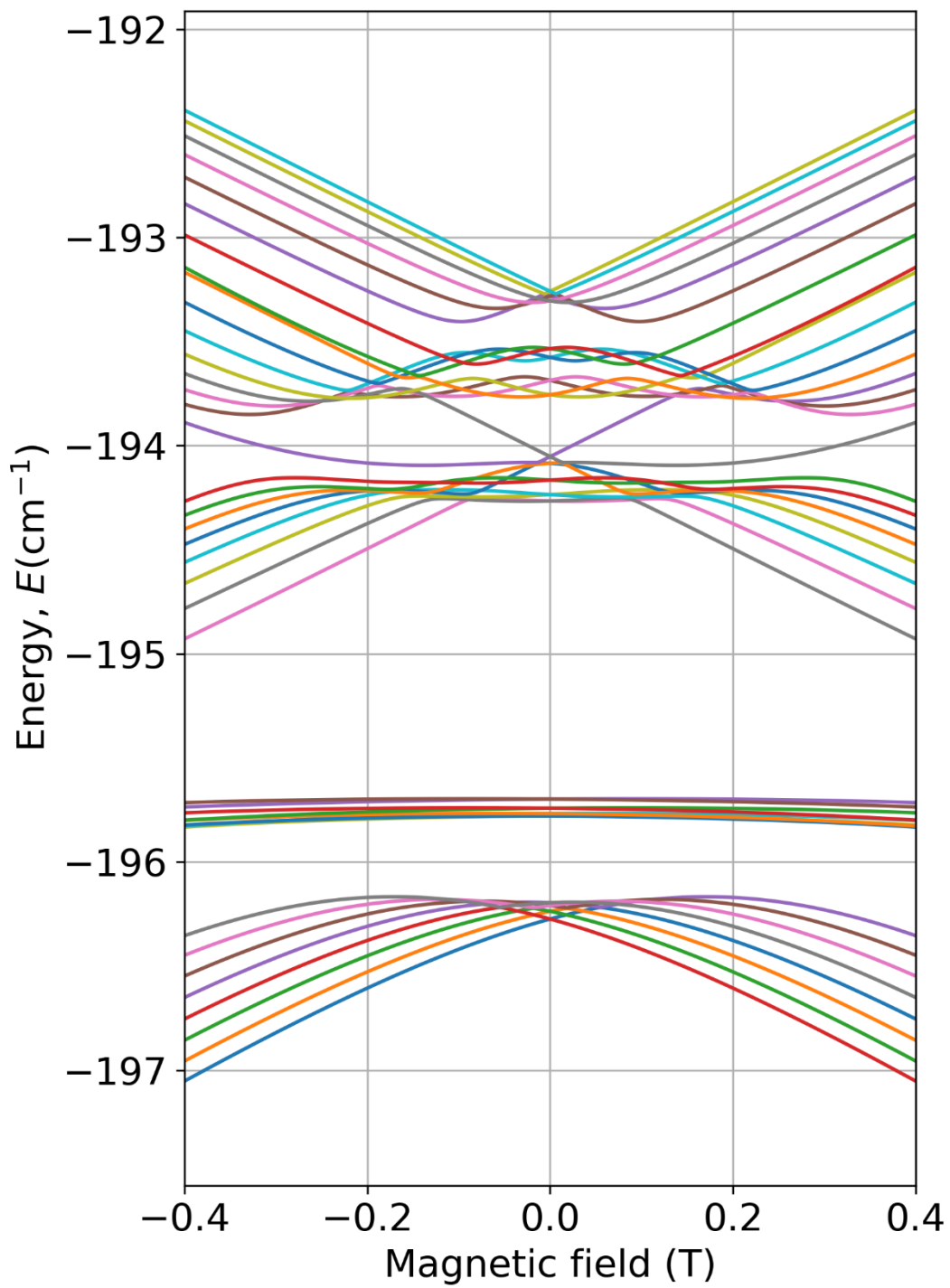


Figure S65: Energy levels splitting for a vertical compression of 0.176%

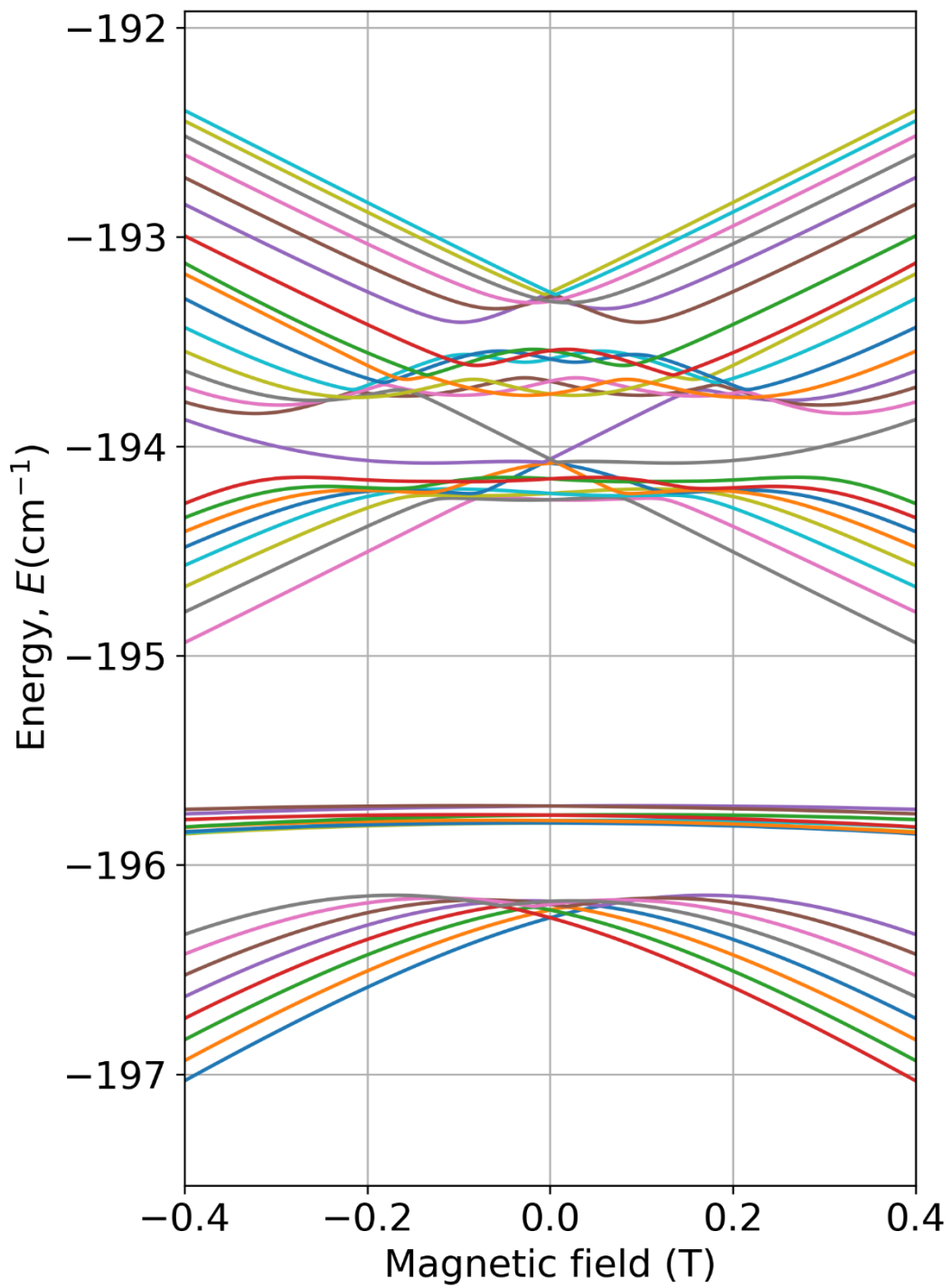


Figure S66: Energy levels splitting for a vertical compression of 0.161%

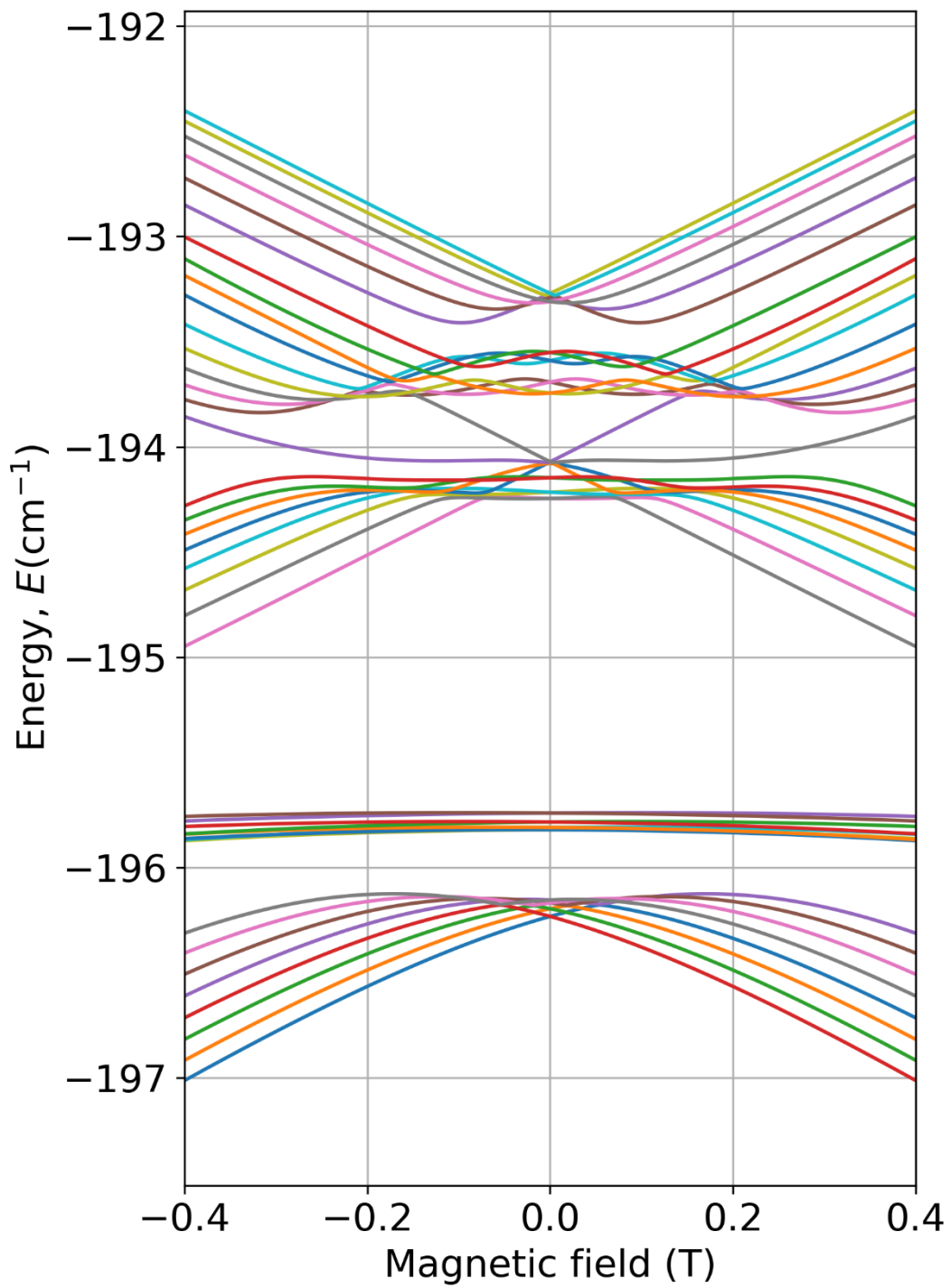


Figure S67: Energy levels splitting for a vertical compression of 0.147%

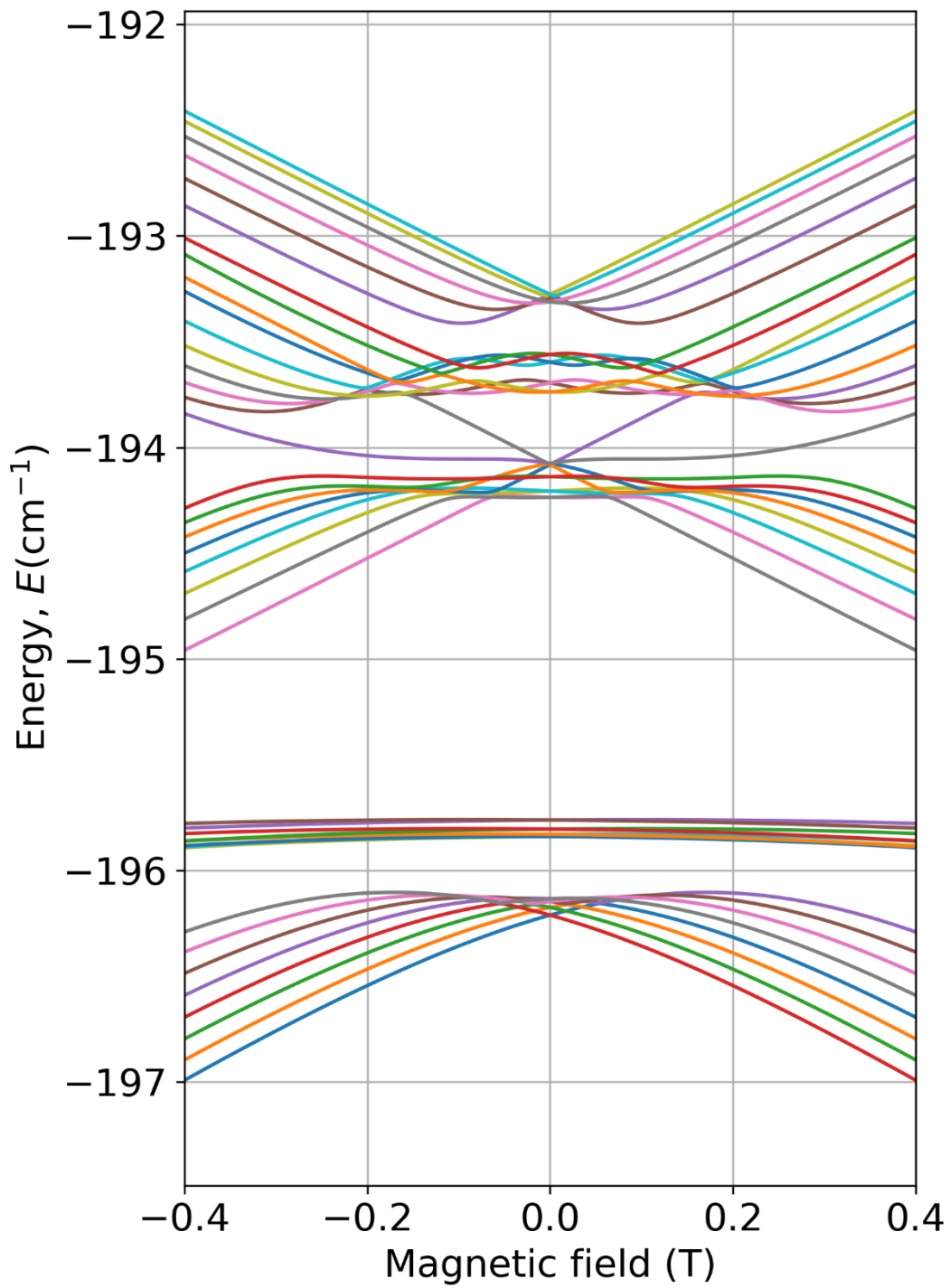


Figure S68: Energy levels splitting for a vertical compression of 0.132%

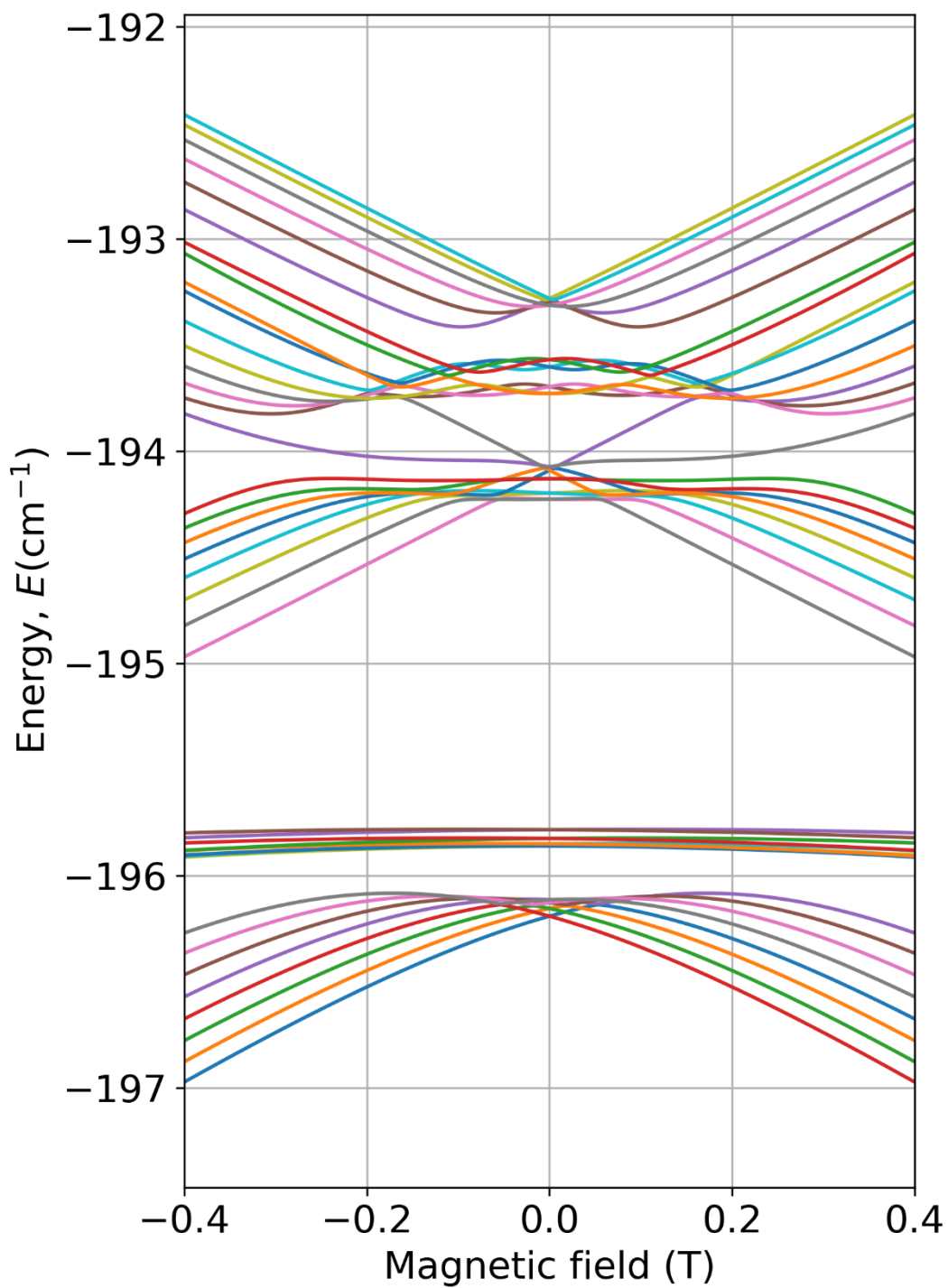


Figure S69: Energy levels splitting for a vertical compression of 0.117%

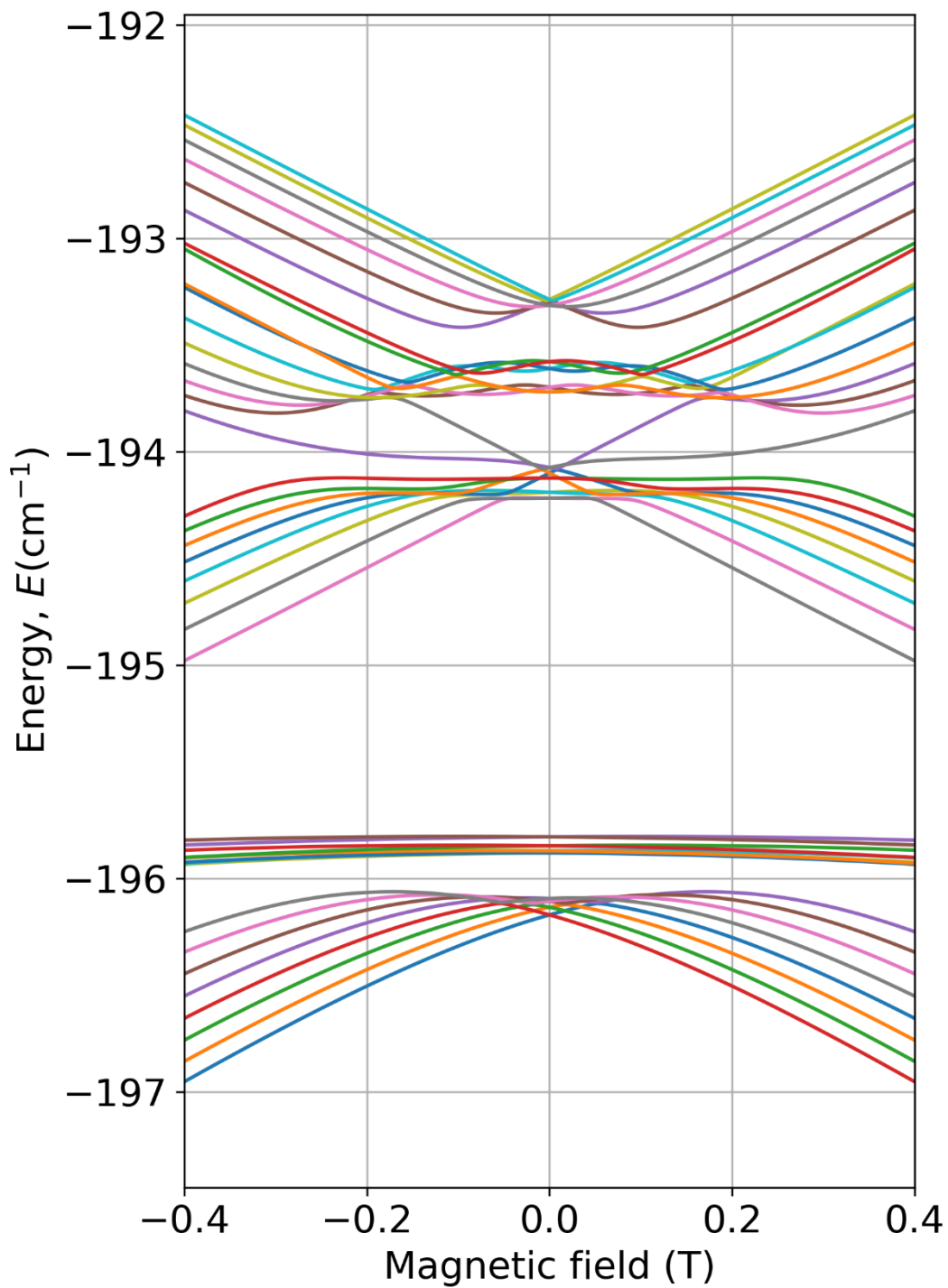


Figure S70: Energy levels splitting for a vertical compression of 0.102%

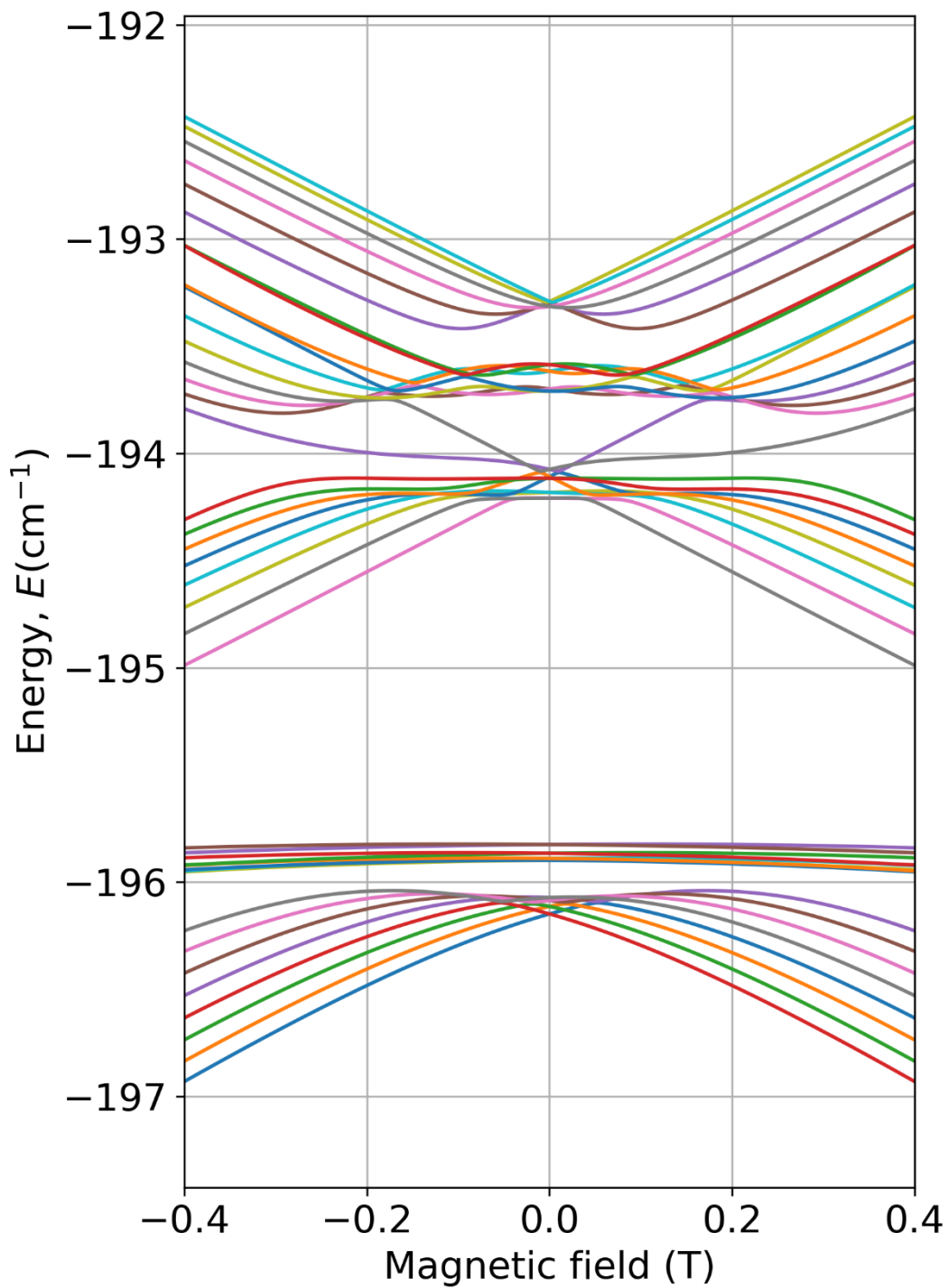


Figure S71: Energy levels splitting for a vertical compression of 0.088%

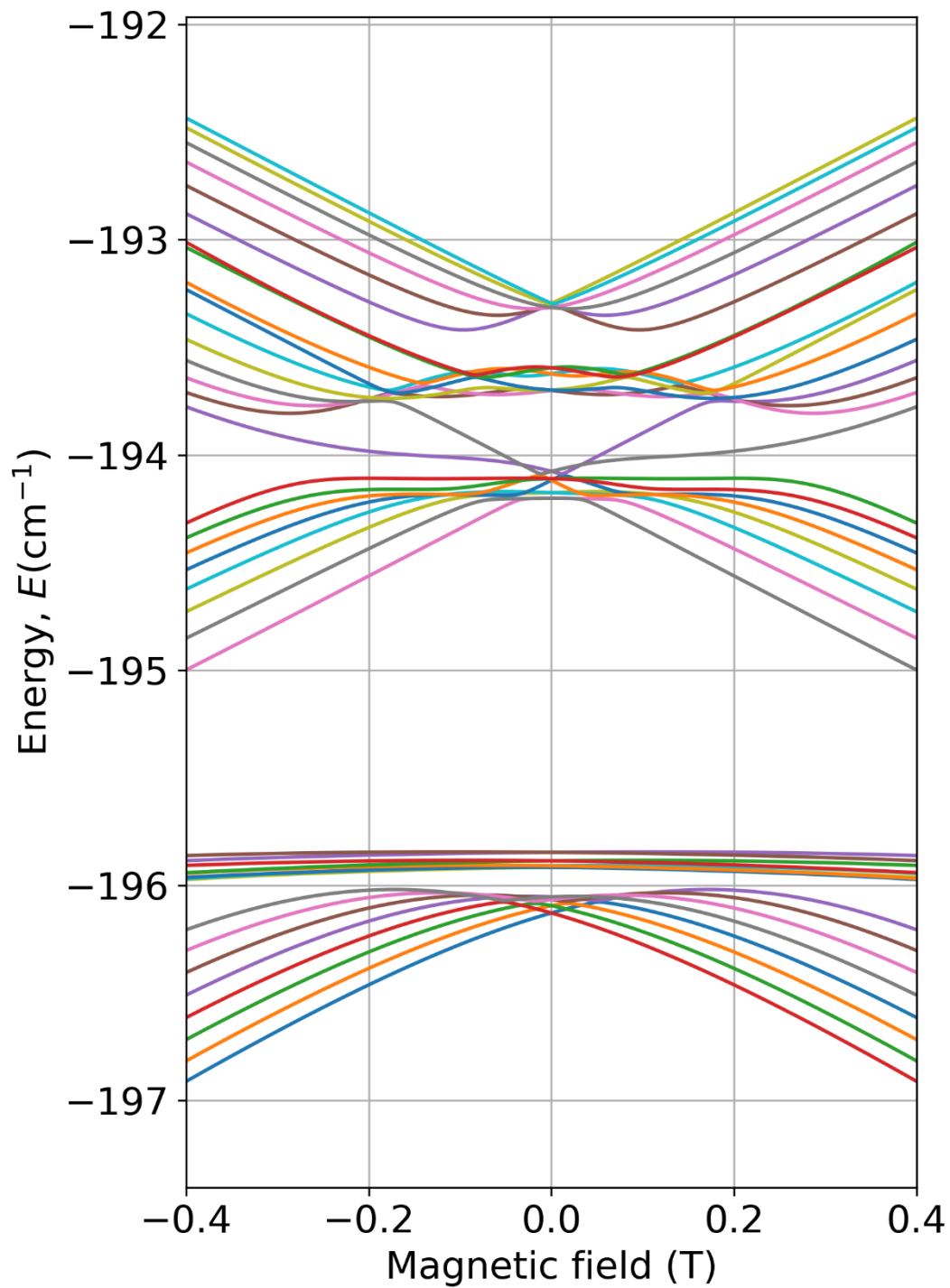


Figure S72: Energy levels splitting for a vertical compression of 0.074%

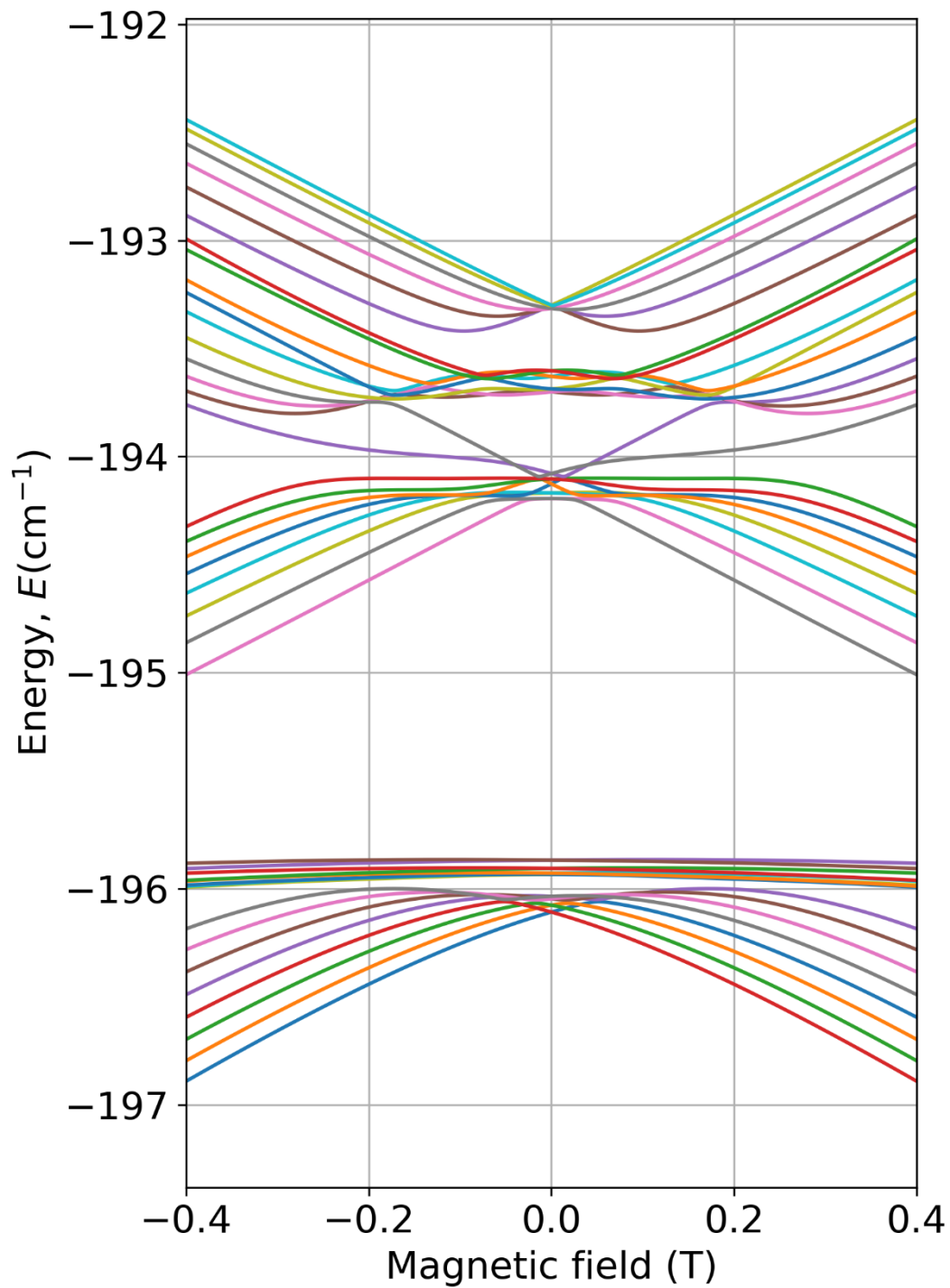


Figure S73: Energy levels splitting for a vertical compression of 0.059%

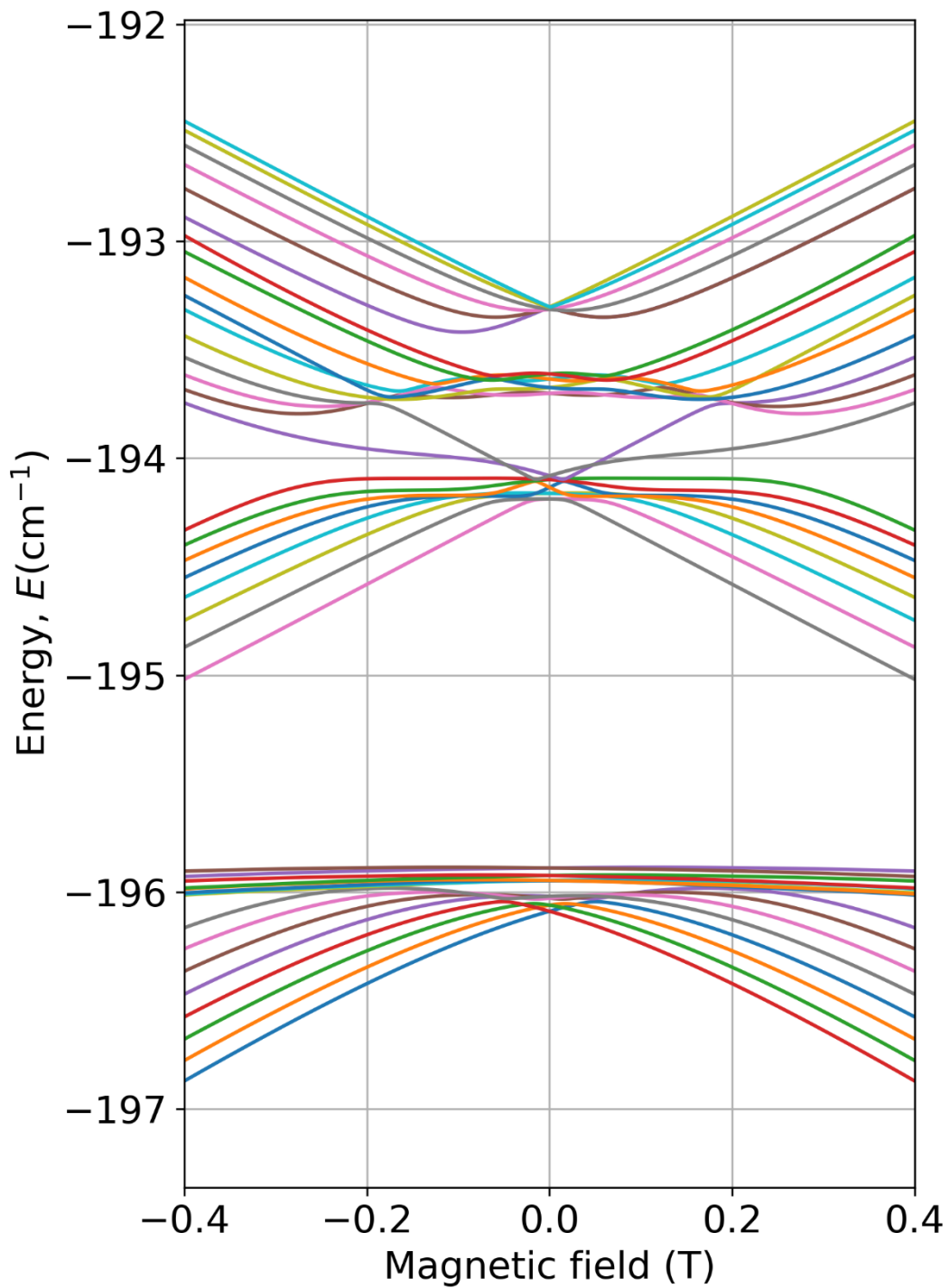


Figure S74: Energy levels splitting for a vertical compression of 0.044%

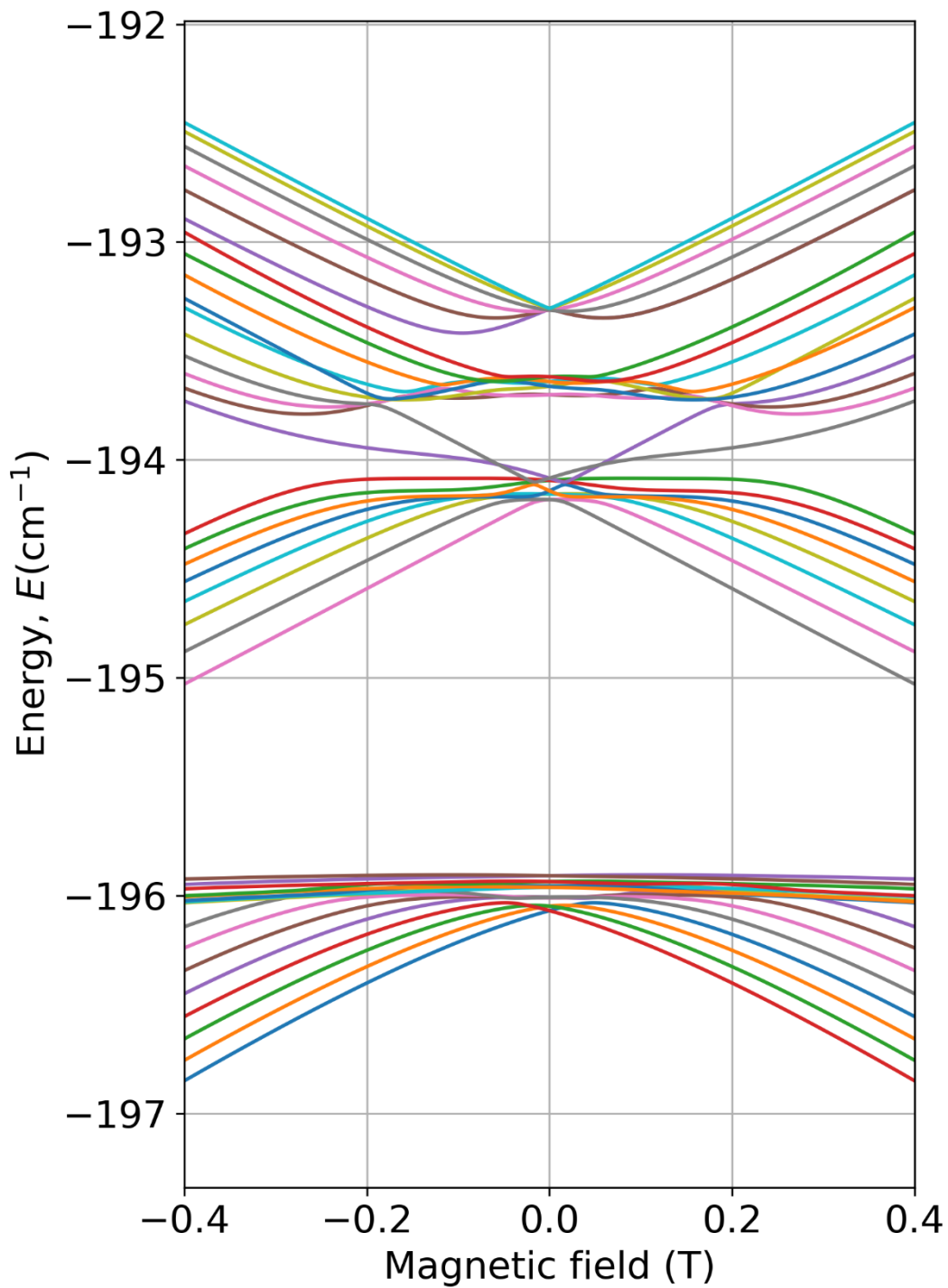


Figure S75: Energy levels splitting for a vertical compression of 0.029%

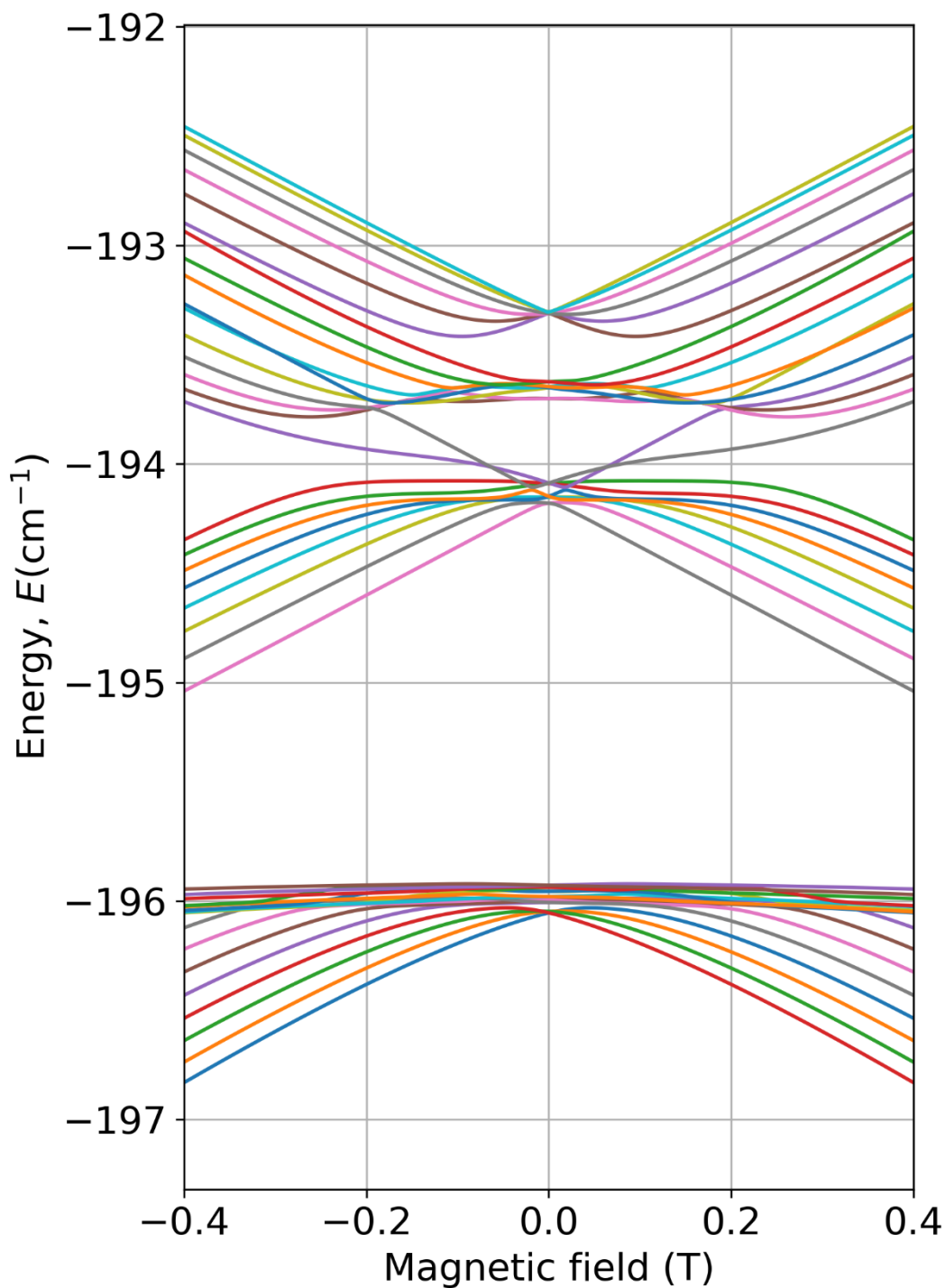


Figure S76: Energy levels splitting for a vertical compression of 0.015%

a. Potential CTs in a perfect cubic HoPd12

Here we report the identified CTs in HoPd12 system, for a given range of frequencies. We focused the search of CTs for the most common EPR-bands: L-band [0.8-1.4 GHz (0.03-0.04 cm^{-1})], X-band [9 GHz (0.33 cm^{-1})], Q-band [35 GHz (1.167 cm^{-1})], W-band [95 GHz (3.1688 cm^{-1})]. This search is traduced on the objective of finding spin levels that accomplish a energy splitting between them equal or in the range of the energy of a EPR-band.

Starting from the perfect cubic geometry for which spin levels scheme is depicted in Fig. 6b, we give detailed information for the identified CTs at different energy ranges:

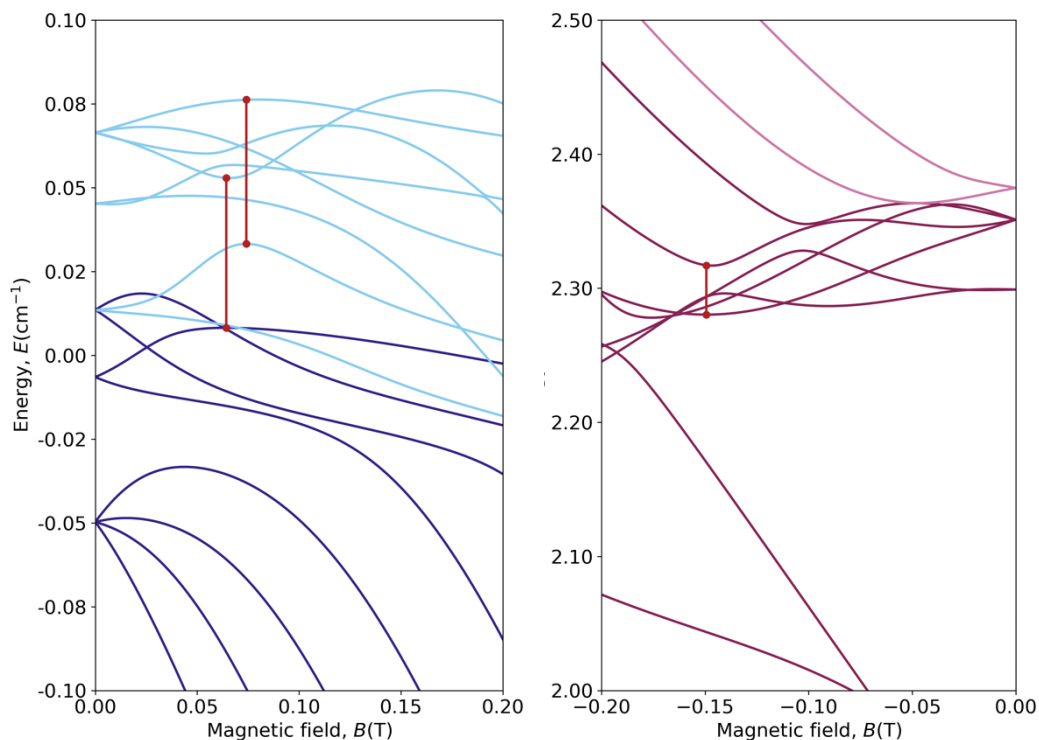


Figure S77: Identified transitions with tunneling splitting energies in the range ~ 0.8 - 1.4 GHz (0.03 - 0.05 cm^{-1}). Left: Zoom in of transitions appearing at the 16th fundamental levels, for simplicity only positive values of magnetic field are shown; right: Zoom in of the transition appearing at the next 24th fundamental levels, for simplicity only negative values of magnetic field are shown. See table S4.

Table S4: Detailed information about the transitions depicted in Fig. S77.

i	j	Type	H_{CT}	E_i	E_j	ΔE_{ij}	k_i	k_j
10	15	Avoided	0.0741	-195.9667	-195.9237	0.043	26.70	3.78
5	14	Avoided	0.0642	-195.9918	-195.9471	0.044	2.96	24.61
29	30	Avoided	-0.149	-193.7196	-193.6831	0.036	13.13	70.90

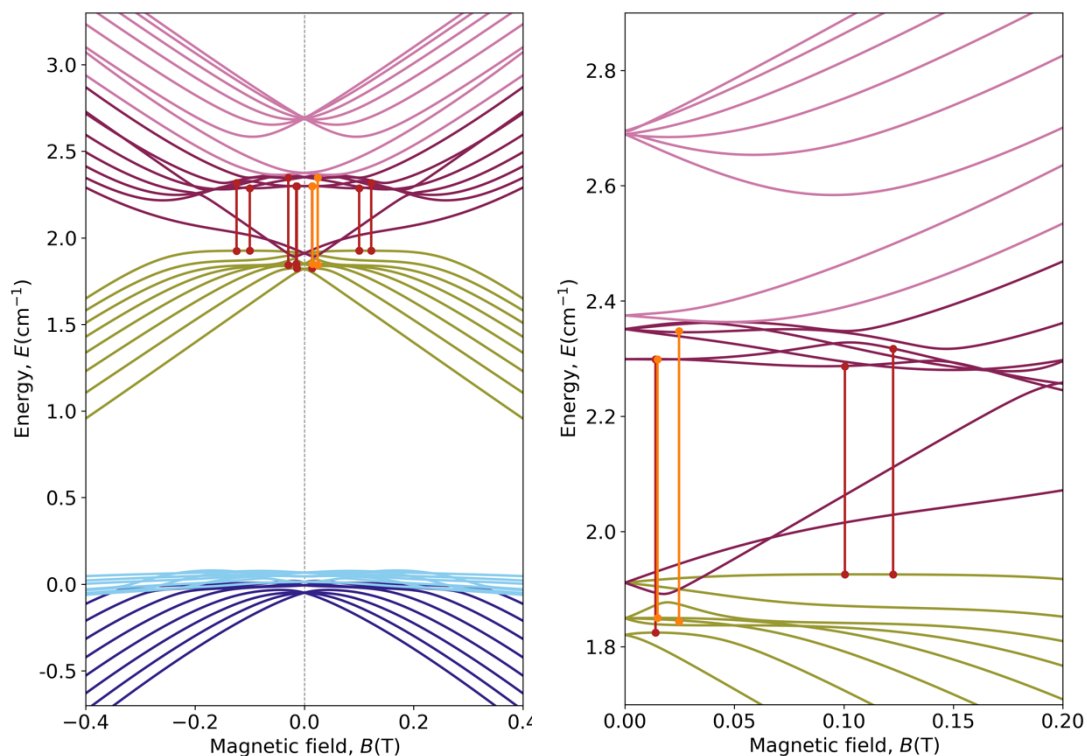


Figure S78: Identified transitions with tunneling splitting energies in the range ~ 9 -15 GHz (0.3 - 0.51 cm^{-1}). Right: complete Zeeman diagram for the fundament 40 spin levels. Left: Zoom in of the CTs, for simplicity and because of symmetry only positive values of magnetic field are shown. See table S5.

Table S5: Detailed information about the transitions depicted in Fig. S78.

i	j	Type	H_cross	E_{maxi}	E_{maxj}	ΔE_{ij}	k_i	k_j
17	26	Avoided	0.0140	-194.175	-193.701	0.473	27.57	4.94
18	27	Avoided	-0.0140	-194.175	-193.701	0.47	27.0	4.94
19	26	Avoided (*)	0.0149	-194.150	-193.701	0.450	5.21	5.27
20	27	Avoided	-0.0149	-194.150	-193.701	0.448	5.27	5.49
21	30	Avoided (*)	0.0247	-194.156	-193.652	0.504	0.82	0.40
22	32	Avoided	-0.0295	-194.156	-193.652	0.504	0.88	0.47
23	27	Avoided	0.100	-194.074	-193.713	0.360	1.32	10.07
23	32	Avoided	0.1224	-194.0746	-193.683	0.391	1.76	8.46

The composition of both level 21 and level 30 are a mixture with contributions of all M_I from -8 to $+8$, but for each M_I only a few M_I values contribute, giving a very clear structure of non-zero components that are slightly displaced with respect to each other (see table S5). Examining the compositions of wavefunctions of levels 21, 30, one can easily verify that, for every non-zero component of level 21 in terms of $|M_J, M_I\rangle$, one finds a non-zero component of level 30 after applying either the ladder operator J_- or, equivalently, the ladder operator L_- . The EPR transition between these levels is therefore expected to be allowed. For example, in level 21 the wave function coefficient for $M_J-4, M_I-1/2$ is -0.48 , which transits to level 30 with $M_J-4, M_I-3/2$ with coefficient $0.08+0.127i$. However, no transitions were found in ranges from 30 - 45 GHz (1.0 - 1.5 cm^{-1}) neither from 90 - 105 GHz (3 - 3.5 cm^{-1}).

b. Potential CTs for X-band EPR along 1% compression of HoPd12

Here we provide detailed information about interesting transitions with a range of Δ suitable for X-band EPR, found in different steps along the compression procedure.

Table S6: Detailed information about transitions for $c = 0.06$ (Fig. 6d).

i	j	Type	H_cross	E_{max_i}	E_{max_j}	ΔE_{ij}	k_i	k_j
23	26	Avoided	0.051	-194.100	-193.714	0.385	1.87	13.56
23	27	Avoided	0.134	-194.101	-193.724	0.376	0.93	12.39
23	29	Avoided	0.204	-194.100	-193.715	0.385	0.66	3.82
23	31	Avoided	0.194	-194.100	-193.732	0.368	0.93	12.37
24	26	Avoided	-0.132	-194.101	-193.724	0.377	1.10	12.57
24	27	Avoided	-0.051	-194.100	-193.714	0.385	1.88	13.51
24	29	Avoided	-0.197	-194.100	-193.732	0.368	0.82	11.91
24	31	Avoided	-0.204	-194.100	-193.715	0.385	0.66	3.85

Table S7: Detailed information about transitions for $c = 0.65$ (Fig. 6e).

i	j	Type	H_cross	E_{max_i}	E_{max_j}	ΔE_{ij}	k_i	k_j
13	1826	Avoided	0.057	-195.051	-194.716	0.335	0.60	4.54
13	19	Avoided	0.049	-195.051	-194.706	0.345	0.66	3.14
13	20	Avoided	0.068	-195.051	-194.706	0.345	0.55	6.69
14	17	Avoided	-0.050	-195.051	-194.716	0.335	0.66	4.78
14	19	Avoided	-0.068	-195.051	-194.706	0.345	0.60	6.64
14	20	Avoided	-0.049	-195.051	-194.706	0.345	0.66	3.14

Table S8: Detailed information about transitions for $c = 0.95$ (Fig. 6f).

i	j	Type	H_cross	E_{max_i}	E_{max_j}	ΔE_{ij}	k_i	k_j
10	21	Avoided	0.024	-195.063	-194.652	0.412	6.70	0.55
10	25	Avoided	-0.164	-194.985	-194.556	0.429	5.99	0.38
11	16	Avoided	0.048	-195.012	-194.653	0.359	46.19	0.60
11	20	Avoided	0.048	-195.012	-194.617	0.395	44.65	0.66
12	21	Avoided	-0.048	-195.012	-194.653	0.359	46.58	0.60
12	23	Avoided	-0.048	-195.012	-194.617	0.395	44.93	0.49
9	16	Avoided	-0.024	-195.063	-194.652	0.412	6.65	0.55
9	24	Avoided	0.164	-194.985	-194.554	0.431	5.88	0.27

S5. Estimate of instantaneous vibrational distortions

We employ here the output files of a previous work by some of us. [6] In said work, we estimated the time-dependent evolution of spin energy levels in a lanthanide metalloprotein by combining molecular dynamics (AMBER force field) with crystal field analysis (the REC model, like in the present work). Fluctuations of tens of cm^{-1} for spin energy levels at fs times were found. We represent here the time-dependent metal-oxygen distance for a sample 1000 fs trajectory at 3 K (see Fig. S79). The amplitude of the instantaneous vibrational distortions at this timescale is of the order of $0.01 - 0.02 \text{ \AA}$. Following the results of the cited work, we can assume that, as happened in the energies, one will find a reduction in the distance fluctuations following a square root law, meaning that averaging over a period of time that is a hundred times longer translates into one tenth of the noise amplitude.

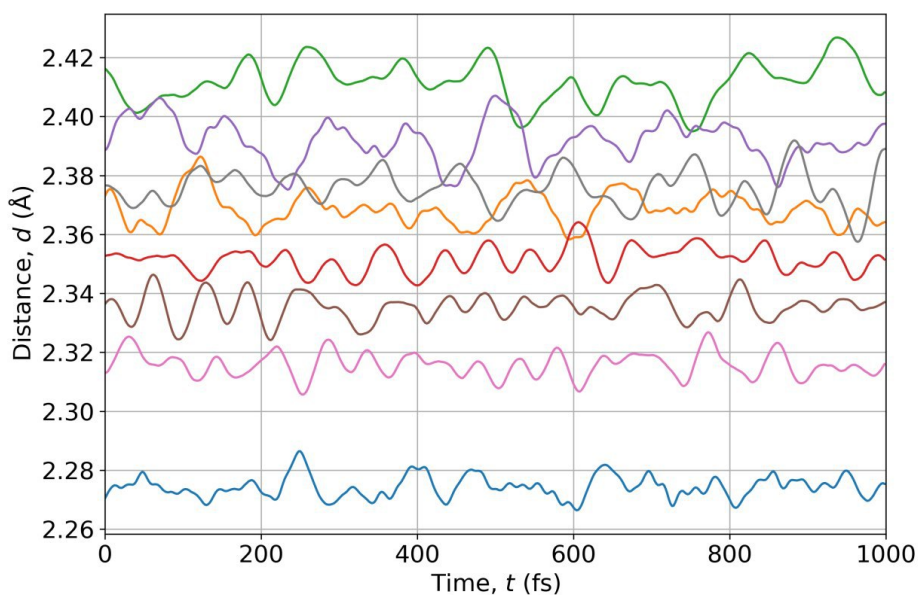


Figure S79: Time evolution of the metal-oxygen distances for each of the 8 atoms in the coordination sphere of the case study, the metalloprotein TbLBT.

S6. Probability of CTs for VO derivative

Here we deepen in the study of wavefunctions for the CTs found in VO derivative complex.

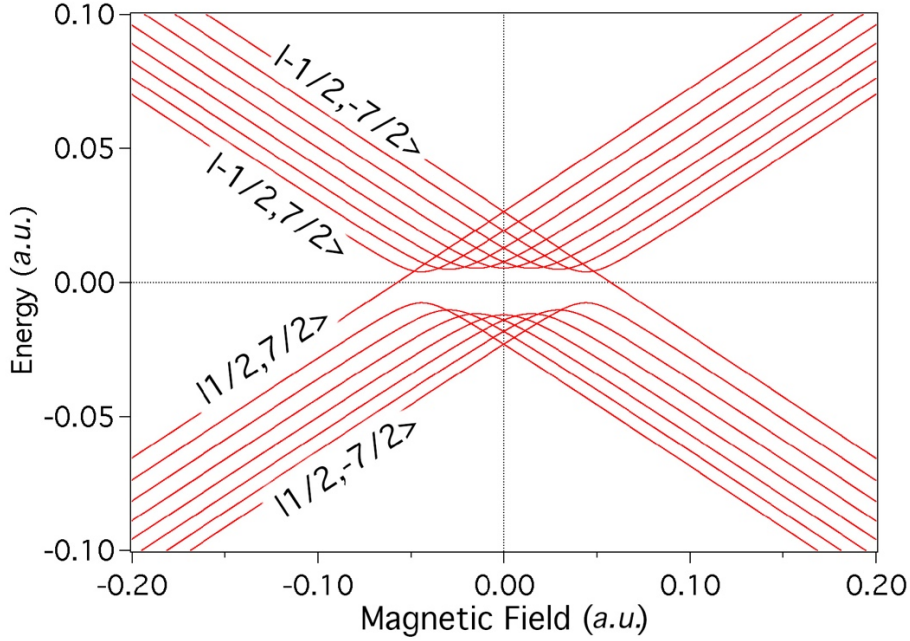


Figure S80: General structure of the anticrossings in terms of the electron spin states and nuclear spin states involved. Since the anticrossings result from the $(S+I_- + S-I_+)$ perpendicular hyperfine term, each anticrossing involves a change in a single unit of the electron spin quantum number together with a change in a single unit but with opposite sign in the nuclear spin quantum number.

Let us begin by constructing the Hamiltonian when a magnetic field in z direction is applied, (B_z) :

$$\hat{H} = g\beta B_{0z} S_z + A_{\parallel} S_z I_z + \frac{1}{2} A_{\perp} (S_+ I_- + S_- I_+)$$

If we suppose a microwave radiation incident perpendicular to the sample, B_I :

$$\hat{H}_{perturb} = g_{xx} \beta B_I S_x \quad \langle \phi_1 | \hat{S}_{\pm} | \phi_2 \rangle \langle \phi_1 | \phi_2 \rangle \neq 0 \quad P_{12} = \left| \langle \phi_1 | \hat{S}_{\pm} | \phi_2 \rangle \langle \phi_1 | \phi_2 \rangle \right|^2$$

In contrast if we suppose a radiation incident parallel to the sample, B_I :

$$\hat{H}_{perturb} = g_{zz} \beta B_I S_z \quad \langle \phi_1 | \hat{S}_z | \phi_2 \rangle \langle \phi_1 | \phi_2 \rangle \neq 0 \quad P_{12} = \left| \langle \phi_1 | \hat{S}_z | \phi_2 \rangle \langle \phi_1 | \phi_2 \rangle \right|^2$$

Where P_{12} is the transition probability.

In the case study of the vanadium complex, CTs appearing at, $B_I = 0$ occurs between two functions with vectors:

$$-\frac{-\beta gH + \sqrt{C}}{4A_x \sqrt{1 + \left| \frac{-\beta gH + \sqrt{C}}{4A_x} \right|^2}} \varphi\left(m_s = \frac{1}{2}, m_j = -\frac{1}{2}\right) + \frac{1}{\sqrt{1 + \left| \frac{-\beta gH + \sqrt{C}}{4A_x} \right|^2}} \varphi\left(m_s = -\frac{1}{2}, m_j = \frac{1}{2}\right)$$

$$\frac{\beta gH + \sqrt{C}}{4A_x \sqrt{1 + \left| \frac{-\beta gH - \sqrt{C}}{4A_x} \right|^2}} \varphi\left(m_s = \frac{1}{2}, m_j = -\frac{1}{2}\right) + \frac{1}{\sqrt{1 + \left| \frac{-\beta gH - \sqrt{C}}{4A_x} \right|^2}} \varphi\left(m_s = -\frac{1}{2}, m_j = \frac{1}{2}\right)$$

Where,

$$C = (4A_x)^2 + (\beta gH)^2$$

Then, probabilities for microwave radiation perpendicular to the sample would be:

$$\begin{aligned} \sqrt{P_{12}} &= \langle \phi_1 | \hat{S}_+ + \hat{S}_- | \phi_2 \rangle \langle \phi_1 | \phi_2 \rangle = \\ &= -\frac{(-\beta gH + \sqrt{C}) \left\langle \frac{1}{2} | S_+ | -\frac{1}{2} \right\rangle \left\langle -\frac{1}{2} | \frac{1}{2} \right\rangle}{4A_x \sqrt{1 + \left| \frac{-\beta gH + \sqrt{C}}{4A_x} \right|^2} \sqrt{1 + \left| \frac{-\beta gH - \sqrt{C}}{4A_x} \right|^2}} - \frac{(-\beta gH - \sqrt{C}) \left\langle -\frac{1}{2} | S_- | \frac{1}{2} \right\rangle \left\langle \frac{1}{2} | -\frac{1}{2} \right\rangle}{4A_x \sqrt{1 + \left| \frac{-\beta gH + \sqrt{C}}{4A_x} \right|^2} \sqrt{1 + \left| \frac{-\beta gH - \sqrt{C}}{4A_x} \right|^2}} \\ &= -\frac{(-\beta gH + \sqrt{C}) \cdot 1 \cdot 0}{4A_x \sqrt{1 + \left| \frac{-\beta gH + \sqrt{C}}{4A_x} \right|^2} \sqrt{1 + \left| \frac{-\beta gH - \sqrt{C}}{4A_x} \right|^2}} - \frac{(-\beta gH - \sqrt{C}) \cdot 1 \cdot 0}{4A_x \sqrt{1 + \left| \frac{-\beta gH + \sqrt{C}}{4A_x} \right|^2} \sqrt{1 + \left| \frac{-\beta gH - \sqrt{C}}{4A_x} \right|^2}} \\ &= 0 \end{aligned}$$

$$P_{12} = 0$$

$$P_{12}(H \rightarrow 0) = 0$$

And CTs probability for microwave radiation parallel to the sample would be:

$$\begin{aligned}
 \sqrt{P_{12}} &= \langle \phi_1 | \hat{S}_z | \phi_2 \rangle \langle \phi_1 | \phi_2 \rangle = \\
 &= -\frac{(-\beta g H + \sqrt{C})(\beta g H + \sqrt{C}) \left\langle \frac{1}{2} | S_z | \frac{1}{2} \right\rangle \left\langle -\frac{1}{2} | -\frac{1}{2} \right\rangle}{(4A_x)^2 \sqrt{1 + \left| \frac{-\beta g H + \sqrt{C}}{4A_x} \right|^2} \sqrt{1 + \left| \frac{-\beta g H - \sqrt{C}}{4A_x} \right|^2}} + \frac{\left\langle -\frac{1}{2} | S_z | -\frac{1}{2} \right\rangle \left\langle \frac{1}{2} | \frac{1}{2} \right\rangle}{\sqrt{1 + \left| \frac{-\beta g H + \sqrt{C}}{4A_x} \right|^2} \sqrt{1 + \left| \frac{-\beta g H - \sqrt{C}}{4A_x} \right|^2}} \\
 &= -\frac{(-\beta g H + \sqrt{C})(\beta g H + \sqrt{C})}{2(4A_x)^2 \sqrt{1 + \left| \frac{-\beta g H + \sqrt{C}}{4A_x} \right|^2} \sqrt{1 + \left| \frac{-\beta g H - \sqrt{C}}{4A_x} \right|^2}} - \frac{1}{2 \sqrt{1 + \left| \frac{-\beta g H + \sqrt{C}}{4A_x} \right|^2} \sqrt{1 + \left| \frac{-\beta g H - \sqrt{C}}{4A_x} \right|^2}} \\
 &= \frac{-C + (\beta g H)^2 - (4A_x)^2}{2(4A_x)^2 \sqrt{1 + \left| \frac{-\beta g H + \sqrt{C}}{4A_x} \right|^2} \sqrt{1 + \left| \frac{-\beta g H - \sqrt{C}}{4A_x} \right|^2}} = \frac{-1}{\sqrt{1 + \left| \frac{-\beta g H + \sqrt{C}}{4A_x} \right|^2} \sqrt{1 + \left| \frac{-\beta g H - \sqrt{C}}{4A_x} \right|^2}} \\
 P_{12} &= \frac{256}{\left(16 + \left| \frac{-\beta g H + \sqrt{C}}{A_x} \right|^2\right) \left(16 + \left| \frac{-\beta g H - \sqrt{C}}{A_x} \right|^2\right)} \quad P_{12}(H \rightarrow 0) = \frac{1}{4}
 \end{aligned}$$

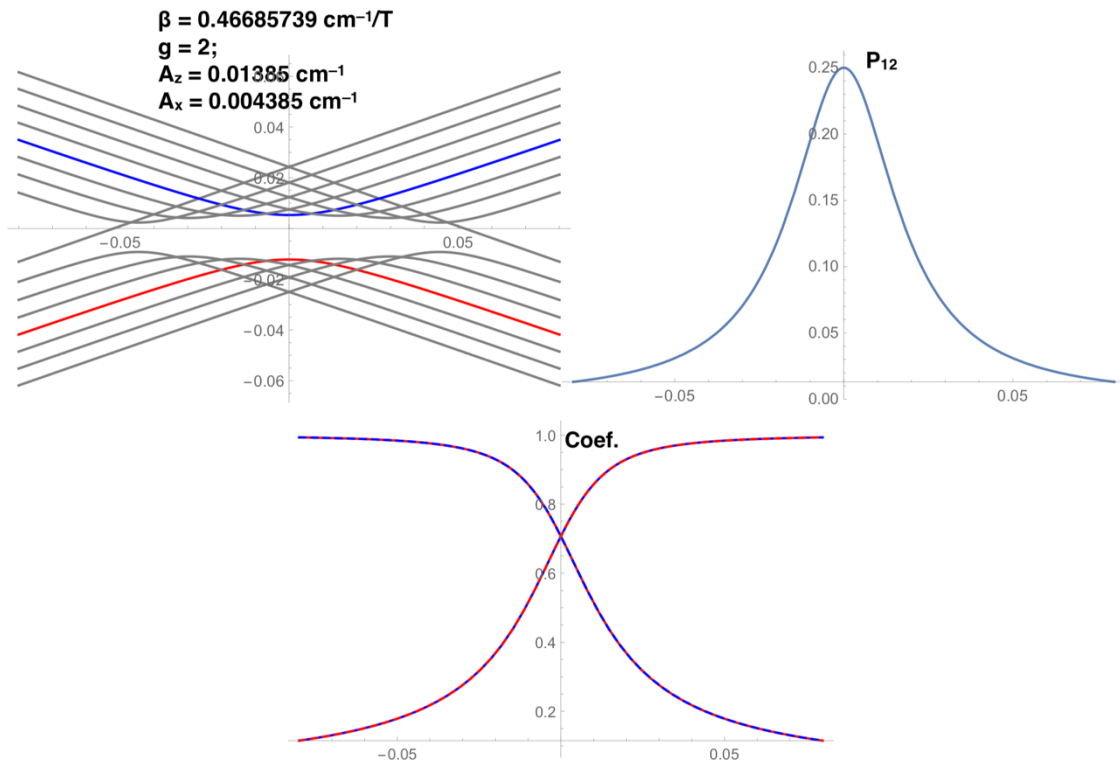


Figure S81: (Up) Energies and probability for CT at $B=0$. (Down) Coefficients involved in the transition.

This probability is not assuming any particular frequency but an upper limit assuming the resonance condition is met. So, it means that, for a given frequency, it has to be multiplied by another Gaussian or Lorentzian function that takes into account the width of the incident microwave, vibrations or any other relaxation in the ΔE .

-
- ¹ C. J. Yu, M. J. Graham, J. M. Zadrozny, J. Niklas, M. D. Krzyaniak, M. R. Wasielewski and D. E. Freedman, *J. Am. Chem. Soc.*, 2016, **138**, 14678.
- ² J. M. Zadrozny, J. Niklas, O. G. Poluektov and D. E. Freedman, *ACS Cent. Sci.* 2015, **1**, 488.
- ³ M. Shiddiq, D. Komijani, Y. Duan, A. Gaita-Ariño, E. Coronado and S. Hill, *Nature*. 2016, **531**, 348.
- ⁴ J. Liu, J. Mrozek, Y. Duan, A. Ullah, J. J. Baldoví, E. Coronado, A. Gaita-Ariño, A. Ardavan, arXiv:2005.01029 [cond-mat.mes-hall].
- ⁵ J. J. Baldoví, L. E. Rosaleny, V. Ramachandran, J. Christian, N. S. Dalal, J. M. Clemente-Juan, P. Yang, U. Kortz, A. Gaita-Ariño and E. Coronado, *Inorg. Chem. Front.* 2015, **2**, 893.
- ⁶ L. E. Rosaleny, K. Zinovjev, I. Tuñón and A. Gaita-Ariño, *Phys. Chem. Chem. Phys.*, 2019, **21**, 10908.